K2K Near Detector Laserball Calibration:

Manipulator Motivation, Design and Results

by

Frank Olaf Berghaus

B.Sc., Saint Mary's University, 2003

A THESIS SUBMITTED IN PARTIAL FULFILMENT OF
THE REQUIREMENTS FOR THE DEGREE OF

Master of Science

in

The Faculty of Graduate Studies

(Physics)

The University Of British Columbia

April 18, 2006

Abstract

The K2K experiment uses a muon neutrino (ν_μ) beam generated at the KEK accelerator facility, aimed at Super-Kamiokande (Super-K) detector 250 km away, to measure ν_μ oscillations first seen from atmospheric ν's at Super-K. The measurement is done using two detectors. The near detector measures the ν_μ flux 300 m from the origin of the neutrino beam. The far detector (Super-K) measures the neutrino flux 250 km downstream. One main source of error in the oscillation measurement is the understanding of the near detector. After some optical calibrations along the vertical axis of the One Kilo Ton (1KT) detector found problems with the position reconstruction a manipulation system was built. The goal of this manipulation system was to allow exploration of the entire 1KT volume with a calibration source. The design required the manipulation system to place the calibration source to ~ 1 cm accuracy in the 1KT, and to avoid all contact with the photomultiplier tubes monitoring the tank volume. This manipulation system was built and tested at TRIUMF (Tri-University Meson Facility) and deployed in the 1KT detector at KEK. The results of the optical position reconstruction indicate a reconstruction bias of unknown origin at high occupancy.

Contents

List of Tables

List of Figures

Acknowledgements

Part I

Thesis

Chapter 1

Introduction

First I will talk about the history of neutrinos from the first predictions to their current place in the Standard Model of particle physics. I will also give a short introduction to the experiments that uncovered the rich field that neutrino physics is today. Next I will discuss the K2K (KEK to Kamioka) experiment and the results of its data run. Finally the near detector system, which the rest of this work will be on, is discussed.

1.1   Neutrinos

In 1931 German physicist Wolfgang Pauli postulated a uncharged particle to save conservation of energy in nuclear beta decay [7]. Enrico Fermi took Pauli's idea and used it in his theory of nuclear decays and dubbed the particle "neutrino" (Italian for "little neutral one"). Until 1953 neutrinos were only needed as a tool to explain missing energy and momentum in beta decays ($\pi^{\pm}$ decays for example). Clyde L. Cowan, Jr and Frederick Reines first observed neutrinos by this reaction [8]:

$$\bar{\nu} + p^+ \rightarrow \beta^+ + n^0 \qquad (1.1)$$

Figure 1.1 shows where neutrinos fit into the current picture of the constituents of matter. The first piece of information to take from Figure 1.1 is that we have two different types of matter, quarks, which make up hadrons, and leptons. The quarks and leptons are further separated in two rows: quarks with charge $q = +\frac{2}{3}$ are in the top row, those with $q = -\frac{1}{3}$ are placed in the second row. The chargeless leptons (neutrinos) are in the third row, and charged leptons in the last row. Furthermore the particles are organized in three columns by their "flavor". For example the first pair of leptons, the e and ν_e, are of electron flavor. Interactions of leptons conserve the total number of leptons as well as lepton flavor. Thus the two quarks (or leptons) of each flavor are associated, meaning that if you see one in a reaction, you

Figure 1.1: Matter consists of either hadrons (quarks) or leptons. Each comes in three flavor generations. The first generation holds the lightest and thus stable fundamental particles while the second and third generations hold the heavier counterparts which decay.

will likely see the other. Quarks do not conserve flavor, as described by the CKM matrix described in the next section. Antimatter is organized in the same way, just that the internal quantum numbers (like charge, or lepton number) are reversed. For example in beta decay an electron is produced and to balance the total number of leptons and the total number of electron-like particles an electron anti-neutrino is produced as an up quark changes into a down quark (eg. Equation 1.2).

$$d \rightarrow u e \bar{\nu}_e \tag{1.2}$$

Cowan and Reines observed the anti-neutrino associated with the electron. In 1962 the Brookhaven National Laboratory (BNL) and CERN reported that neutrinos created in muon decays behave differently from neutrinos produced in beta decays [9] establishing the existence of a second kind of neutrino, called ν_μ. To finish off our current picture the DONUT experiment found the τ neutrino [10], thus giving an uncharged partner to every charged lepton.

1.1.1 Problems

Solar Neutrinos

The Sun is a natural source of neutrinos, which are produced in the fusion reactions fueling the Sun. Figure 1.2 shows the energy spectra of neutrinos emitted by the Sun. These spectra are calculated using measurements from
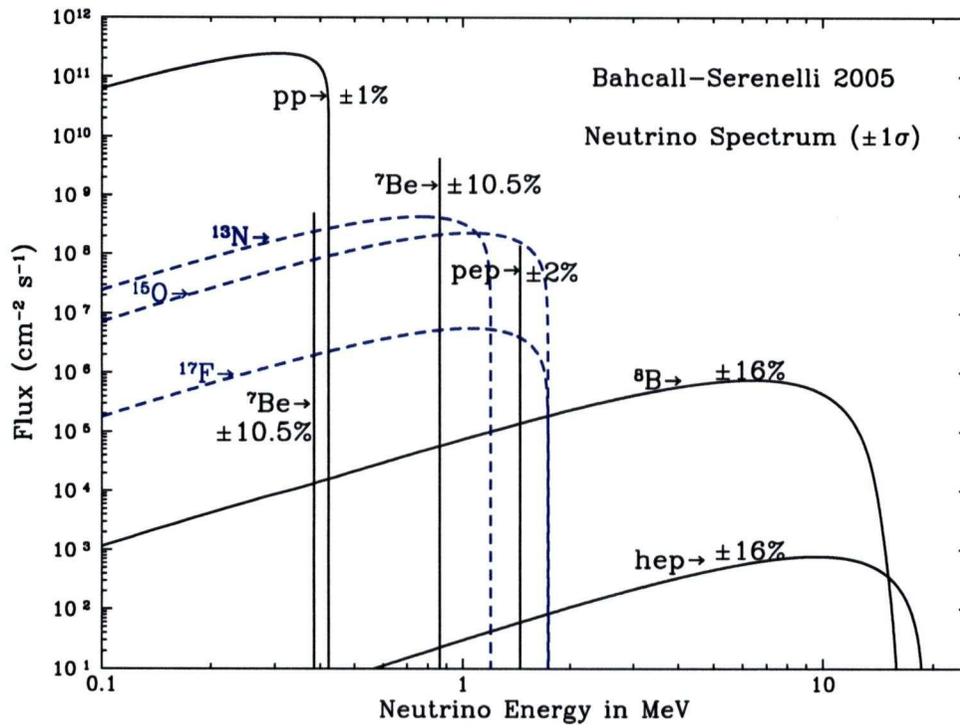
Figure 1.2: Energy spectra of neutrinos emitted by the sun and labeled by the reactions that produce those neutrinos [5].

helio-seismology as constraints on the standard solar model. This allows the calculation of the rates for the reactions producing neutrinos in the Sun.

Ray Davis did the first experiment looking at solar neutrinos at Homestake in 1964 [11]. The number of neutrinos observed by Davis did not agree with the flux predicted using helio-seismology and the standard solar model [12]. In fact Davis observed about a third of the neutrinos that were expected using the solar model. Later the Kamiokande, Sage and GALLEX experiments also saw fewer solar neutrinos than predicted.

The inspiration to explain this problem came from quark flavor mixing. In the decay shown in Equation 1.3 a strange quark turns into a down quark:

$$\Lambda^\circ \rightarrow p\pi^- \tag{1.3}$$

This means that the flavor in quarks is not conserved as it is in leptons. The Cabibbo-Kobayashi-Maskawa (CKM) matrix describes this "mixing" of quark flavors:

$$\begin{pmatrix} d' \\ s' \\ b' \end{pmatrix} = \begin{bmatrix} V_{ud} & V_{us} & V_{ub} \\ V_{cd} & V_{cs} & V_{cb} \\ V_{td} & V_{ts} & V_{tb} \end{bmatrix} \begin{pmatrix} d \\ s \\ b \end{pmatrix} \tag{1.4}$$

where the V-matrix is the CKM matrix. The u, c and t are coupled in CC interactions to d', s' and b' respectively, rather than the original d, s and b quarks. This allows reactions in which quark flavor changes.

The inconsistency between neutrino observations and the solar model prediction can be explained by neutrino oscillations which follow from a similar mixing to the quark mixing described in Equation 1.4 [13]. Neutrino oscillation will be discussed in Section 1.1.2.

Atmospheric Neutrinos

Neutrino oscillations were first observed with the Super-Kamiokande experiment. The Super-Kamiokande experiment now is the far detector for the K2K experiment. Atmospheric neutrinos are produced in hadronic showers caused by cosmic rays entering the atmosphere. Most cosmic rays are protons or light nuclei. When these hit the upper atmosphere a hadronic shower composed of pions and a few other light hadrons is caused. Since over 95% of all neutrinos below 100GeV come from the (charged) pion decay chain and Kamiokande and Super-Kamiokande are sensitive to neutrinos with less

energy than 8 GeV, we can ignore the other hadron decay chains [14]. Equation1.5 shows the relevant decays:

$$\begin{aligned} \pi^{\pm} &\rightarrow \mu^{\pm} + \nu_{\mu}(\bar{\nu}_{\mu}) \\ \mu^{\pm} &\rightarrow e^{\pm} + \nu_e(\bar{\nu}_e) + \bar{\nu}_{\mu}(\nu_{\mu}) \end{aligned} \tag{1.5}$$

The final state electron quickly dissipates in the atmosphere only leaving some photons. So we expect to see two muon-(anti)neutrinos for every electron (anti)neutrino. The Kamiokande and SK detector cannot tell the matter and antimatter states apart, thus we sum over the two. This ratio holds even when considering a large range of other particles in the hadronic showers and a larger window of neutrino energies [14, 15].

Furthermore the cosmic radiation incident upon the atmosphere is isotropic, and neutrino interactions with matter are negligible. Thus we expect to see an isotropic distribution of neutrinos from the Super-Kamiokande experiment. Super-K found that neutrinos oscillate by observing an anisotropic muon neutrino flux and by comparing theoretical and experimental ratios of muon to electron neutrinos. Figure 1.3 shows the results of the Super-K experiment.

1.1.2 Theory

Since neutrinos are chargeless leptons they only feel the weak force (neglecting gravity). As such neutrino interactions are lumped into two categories: Charged Current (CC) when the weak force mediator is a $W^{\pm}$ and Neutral Current (NC) when the weak force is mediated by the Z^0. To observe the neutrino oscillations I talked about in the last section we have to assume that the flavor (interaction) and mass (propagation) eigenstates of neutrinos are not the same.

Two Neutrino Oscillation

To simplify this explanation let us consider a model where only two ν exist and oscillate. Equation 1.6 shows a ν_{μ} just after it is created. Here ν_{μ} is the interaction eigenstate that couples to the muon and ν_2 and ν_3 are the two mass eigenstates. Since both interaction and mass eigenstates form a complete basis for all neutrinos we can write one as a linear combination of the other.

$$\begin{aligned} |\nu_{\mu}\rangle &= \cos\theta_{12}|\nu_1\rangle + \sin\theta_{12}|\nu_2\rangle \\ |\nu_{\tau}\rangle &= -\sin\theta_{12}|\nu_1\rangle + \cos\theta_{12}|\nu_2\rangle \end{aligned} \tag{1.6}$$
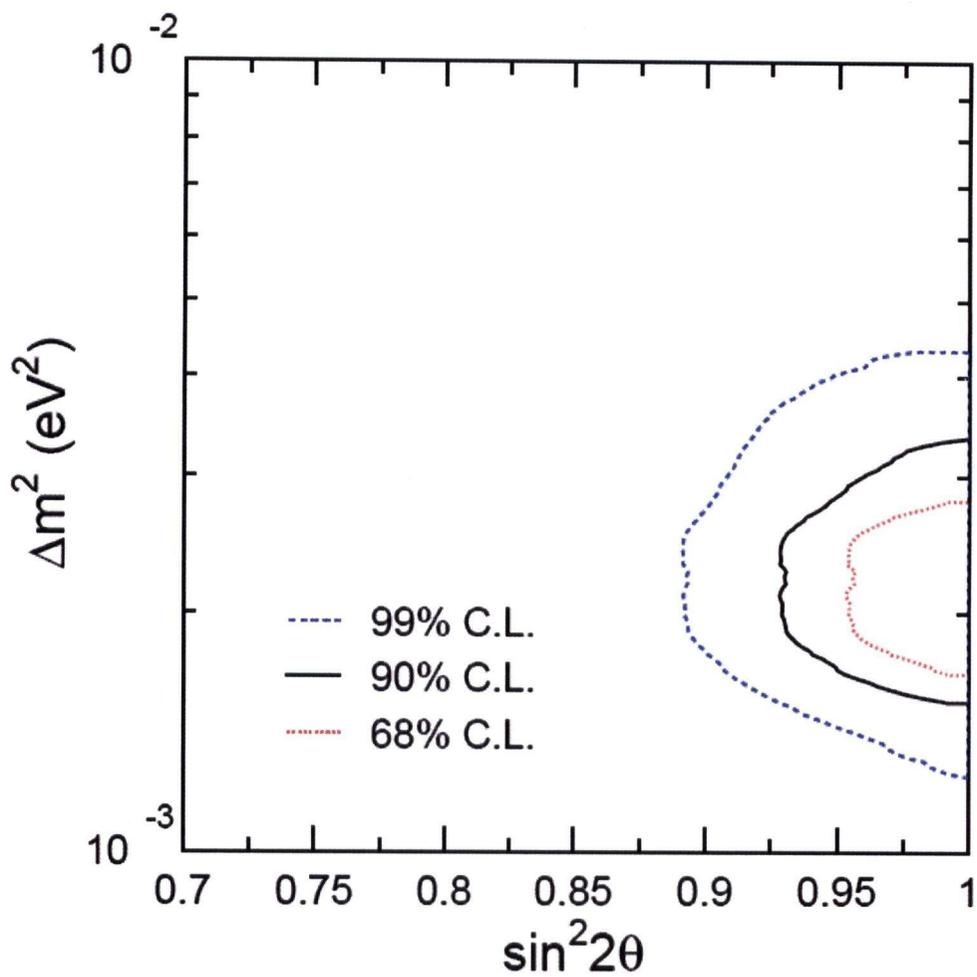
Figure 1.3: Results of the Super-K neutrino oscillation measurement. This zenith result comes from investigating the muon neutrino anisotropy [6]

Equation 1.7 adds time dependence to the ν_μ as predicted by quantum mechanics:

$$|\nu_\mu(\vec{x}, t)\rangle = e^{-\imath(E_1 t - \vec{p_1}\cdot\vec{x})}\cos\theta_{12}|\nu_1\rangle + e^{-\imath(E_2 t - \vec{p_2}\cdot\vec{x})}\sin\theta_{12}|\nu_2\rangle$$
$$|\nu_\tau(\vec{x}, t)\rangle = -e^{-\imath(E_1 t - \vec{p_1}\cdot\vec{x})}\sin\theta_{12}|\nu_1\rangle + e^{-\imath(E_2 t - \vec{p_2}\cdot\vec{x})}\cos\theta_{12}|\nu_2\rangle \quad (1.7)$$

Note from Equation 1.7 that neutrino oscillation only occur if the propagation eigenstates of the neutrinos have different masses. If we express the mass eigenstates in terms of flavor states by solving Equation 1.6 for the mass states we have:

$$\begin{pmatrix} |\nu_\mu(\vec{x},t)\rangle \\ |\nu_\tau(\vec{x},t)\rangle \end{pmatrix} = \lambda(\theta_{12}) \begin{bmatrix} e^{-\imath(E_1 t - \vec{p_1}\cdot\vec{x})} & 0 \\ 0 & e^{-\imath(E_2 t - \vec{p_2}\cdot\vec{x})} \end{bmatrix} \lambda^{-1}(\theta_{12}) \begin{pmatrix} |\nu_\mu\rangle \\ |\nu_\tau\rangle \end{pmatrix}$$
$$(1.8)$$

Where $\lambda(\theta)$ is the rotation matrix:

$$\lambda(\theta) = \begin{bmatrix} \cos\theta & \sin\theta \\ -\sin\theta & \cos\theta \end{bmatrix}$$

Now assuming we start of with a muon neutrino, as we do at K2K we obtain the probability of observing a tauon neutrino by Equation 1.9:

$$\langle\nu_\mu|\nu_\tau(\vec{x},t)\rangle = P_{\nu_\mu \to \nu_\tau} = \sin^2(2\theta_{12})\sin^2(\frac{1.27\Delta m_{12}^2 L}{E}) \quad (1.9)$$

Here $\Delta m_{12}^2 = m_1^2 - m_2^2$ is the mass squared difference in eV, L is the distance traveled (in km), and E is the total energy of the neutrino (in GeV). Now you can see that we should only observe neutrino oscillations if neutrinos have mass and those masses differ between the different neutrino mass eigenstates. From the results of the Super-K experiment [6] we take an estimate of Δm_{12}^2 and tune E such that knowing L we measure Δm_{12}^2 precisely. Note that if:

$$\frac{1.27\Delta m^2 L}{2\pi E} \gg 1 \quad (1.10)$$

the probability of finding either flavor averages to $\frac{1}{2}$, if $\sin^2 2\theta_{12} = 1$.

Figure 1.4 shows the probability to observe the neutrino of the original flavor ($P_{\nu_\mu \to \nu_\tau} = 0$) or the neutrino of the oscillated flavor ($P_{\nu_\mu \to \nu_\tau} = 1$) depending on when you observe the neutrino.
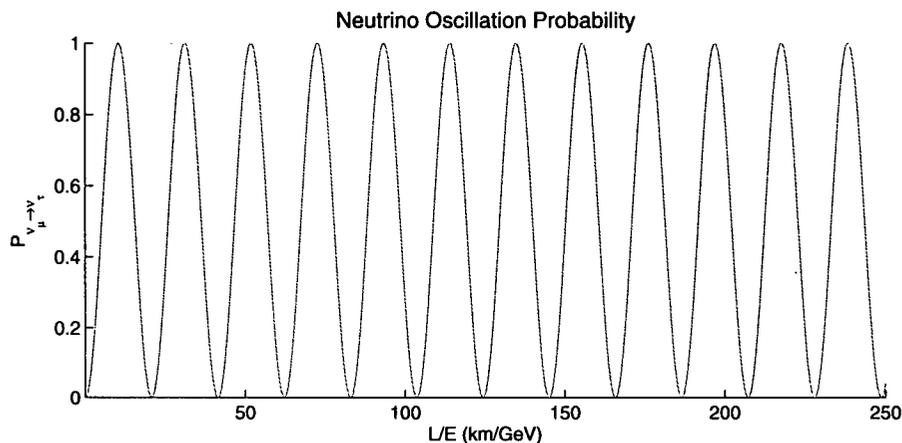
Figure 1.4: The probability for a neutrino of flavor μ to oscillate into neutrino of flavor τ after traveling a distance L (km) at energy E (GeV). The mass squared difference was taken to be $\Delta m^2 = 3 \cdot 10^{-3}\ eV^2$ for $\sin^2 2\theta = 1$ as taken from the latest K2K results [16].

1.1.3 Extension to Three Neutrinos

Since we have three generations of neutrinos we must do this for each of the three possible combinations. Doing this we obtain Equation 1.11.

$$|\nu_l\rangle = \sum_i^3 U_{li}|\nu_i\rangle \tag{1.11}$$

Here l is the lepton (e, μ, τ) associated with ν_l and the ν_i are the neutrino mass eigenstates. U is the Maki-Nakagawa-Sakata (MNS) matrix [17] describing neutrino mixing and is analogous to the CKM matrix describing quark mixing.

It is more convenient to look at the MNS matrix broken into three matrices each describing oscillations involving two of the three neutrino mass eigenstates.

$$U = \begin{bmatrix} 1 & 0 & 0 \\ 0 & c_{23} & s_{23} \\ 0 & -s_{23} & c_{23} \end{bmatrix} \begin{bmatrix} c_{13} & 0 & e^{-i\delta}s_{13} \\ 0 & 1 & 0 \\ -e^{i\delta}s_{13} & 0 & c_{13} \end{bmatrix} \begin{bmatrix} c_{12} & s_{12} & 0 \\ -s_{12} & c_{12} & 0 \\ 0 & 0 & 1 \end{bmatrix}$$

Here $s_{ij} = \sin\theta_{ij}$ and $c_{ij} = \cos\theta_{ij}$ and δ is a phase factor that introduces CP violation for the neutrino sector. The first matrix (23-mixing) is maximal (ie $\theta_{23} \approx \frac{\pi}{4}$) and can be investigated by atmospheric and long baseline

neutrino experiments. In the second matrix (13-mixing) the mixing angle is small (similar to quark mixing) with $\theta_{13} < \frac{\pi}{20}$. Solar neutrino experiments found the last matrix (12-mixing) to show large but non-maximal mixing with $\theta_{12} \approx \frac{\pi}{6}$ [18].

1.1.4 Previous Experiments

Since the discovery of neutrino oscillation in 1998 the mixing angles of the MNS matrix have been investigated thoroughly. The Super-K group measured the ν_μ disappearance interpreted as $\nu_\mu \leftrightarrow \nu_\tau$ oscillation by observing atmospheric neutrinos. This observation gives the mixing angle θ_{23} as $\sin^2 2\theta > 0.92$ and $1.5 \cdot 10^{-3} < \Delta m_{23}^2 < 3.4 \cdot 10^{-3}\ eV^2$ (at 90% confidence) for the associated mass eigenstates [6]. Together the SNO and KamLAND experiment have measured $\nu_e \leftrightarrow \nu_{\mu/\tau}$ mixing, which allows the measurement of $\theta_{12} = 33.9^{+2.4}_{-2.2}$ and $\Delta m_{12}^2 = \left(8.0^{0.6}_{-0.4}\right) \cdot 10^{-5}\ eV^2$ using neutrinos produced in the Sun [19] or in reactors. The allowed mass squared differences and mixing angles for the neutrino mass eigenstates are summarized in Figure 1.5 for the results from solar neutrinos and Figure 1.6 for long baseline neutrino experiments.

1.2 The K2K Experiment

The KEK to Kamioka (K2K) is the first accelerator-based long-baseline neutrino oscillation experiment, and measures the same oscillation as atmospheric neutrino experiments such as Super-K. The K2K experiment confirmed $\nu_\mu \leftrightarrow \nu_\tau$ oscillation seen by experiments like Super-K [6] at greater than 4σ significance [16].

The K2K measurement uses an accelerator-made neutrino beam and measures the energy-dependent difference between the ν_μ flux measured at near (300 m from the beam origin) and far (250 km) detectors. The neutrino oscillation parameters are fitted by predicting the neutrino flux and spectrum for the far detector based upon the measurement from the near detector.

To measure $\nu_\mu \leftrightarrow \nu_\tau$ oscillation K2K uses a muon neutrino (ν_μ) beam made at the KEK accelerator site that is aimed at the Super-K detector in Kamioka. The neutrino beam is made by scattering 12 GeV protons off an aluminum target and focusing the produced π^+ into a decay pipe using two horn magnets. The pions decay to give a 98% pure muon neutrino
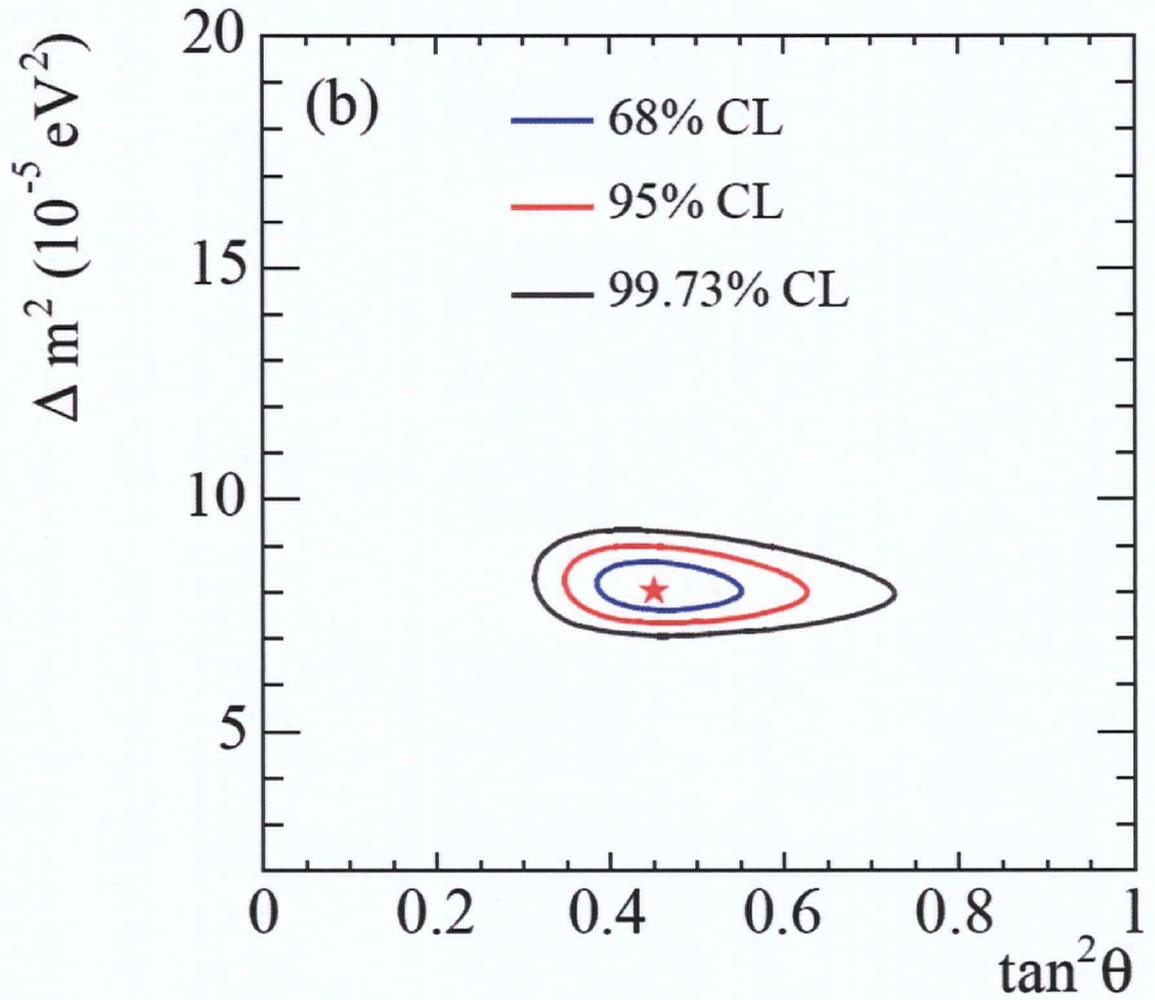
Figure 1.5: The allowed region for mass squared difference and mixing angle for the solar neutrino sector. Data from SNO, KamLAND, Gallex, and SAGE [19].
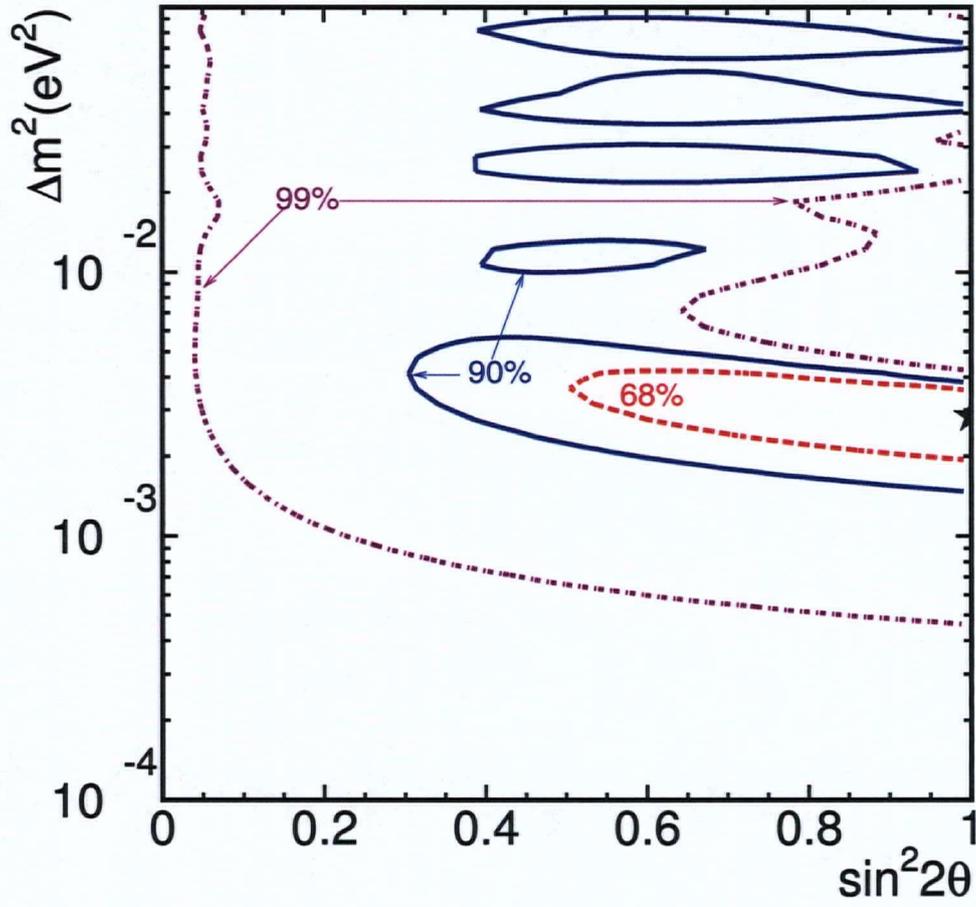
Figure 1.6: The allowed region in mass squared difference and mixing angle for the atmospheric neutrino sector according to the K2K long baseline experiment.
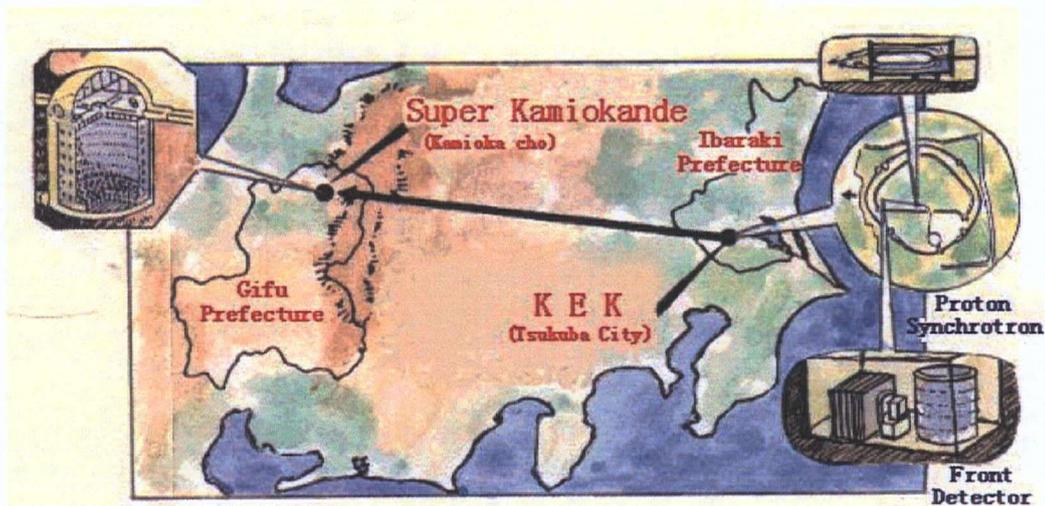
Figure 1.7: The K2K experiment fires a ν_μ beam made at the KEK accelerator at the Super-Kamiokande detector through 250 km of earth. The near (or front) and Super-Kamiokande (or far) detector measure the muon neutrino flux. Neutrino oscillation is measured through ν_μ disappearance [20].

beam. The neutrinos travel a distance of L = 250 km with mean beam energy E = 1.3 GeV through the island of Honshu in Japan as displayed in Figure 1.7.

1.3 The KEK Proton Synchrotron And Beam Line

The ν beam is produced at KEK by a synchrotron that accelerates protons to 12 GeV (KEK-PS). The protons are accelerated step by step as summarized in Table 1.1. Protons are inserted into the accelerator in spills which occur every 2.2 s. Each spill carries $7 \cdot 10^{12}$ protons in nine "bunches" separated by 120 ns. In total then a spill of protons (from first to ninth bunch) lasts 1.1 μs.

To accelerate the protons in a spill to 12GeV they must go through the Main Ring. After one cycle in the main ring the protons are extracted though a beam pipe leading to the target. On the way to the target the beam profile

Table 1.1: KEK Beam Accelerator Components [1]

Accelerator Component	Final Proton Energy
Pre-injector	750 keV
LINAC	40 MeV
BOOSTER	500 MeV
Main Ring	12 GeV
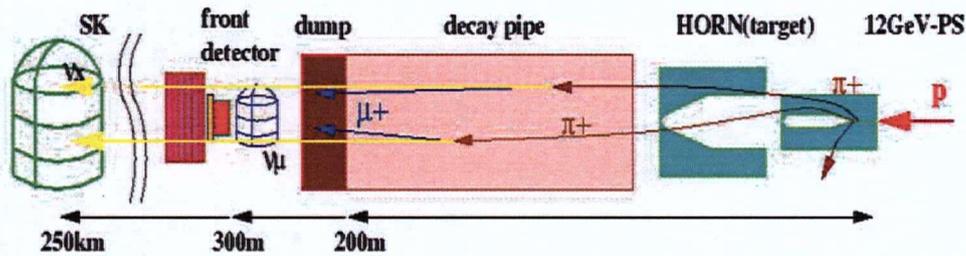
Figure 1.8: Schematic of the K2K neutrino beam generation and travel.

and intensity are carefully monitored. The position of the proton beam needs to be known accurately such that the final neutrino beam is properly directed at the far detector. Finally the spill of protons hits the target. At this point about $(5-6) \cdot 10^{12}$ protons are left in the nine bunches.

1.3.1 The Neutrino Beam

Figure 1.8 shows a schematic of the K2K experiment. The proton beam hits the aluminum target creating a pion beam. The target is a 66cm long cylinder with a 3cm diameter. It is made of 6061-t aluminum alloy [1].

The Horn Magnets

Two so-called "horn magnets" are cylindrically symmetric magnets that create a toroidal magnetic field. They function on a 250 kA current pulse lasting for 2 msec on a 2.2 s cycle. This pulse current is synchronized with the beam spills. The horn magnets operate on this pulsed current to prevent overheating.

The target is inside the first horn magnet forming the conductor core for the magnet. The second magnet is placed 10.5 meters downstream. The

Table 1.2: ν Beam Composition At Origin [2]

Particle	Source	Fraction of Beam
ν_μ	Low Energy: $\pi^+ \to \mu^+ \nu_\mu$, High Energy: $K^+ \to \mu^+ \nu_\mu$	97.3%
ν_e	$\mu^+ \to e^+ \bar{\nu}_\mu \nu_e$	1.3%
$\bar{\nu}_\mu$	$\pi^- \to \mu^- \bar{\nu}_\mu$ or μ^+ decay	1.5%
$\bar{\nu}_e$	$K_L^0 \to \pi^\pm e^\pm \nu_e$	0.018%

toroidal magnetic field created by the horn magnets focuses positive particles (mostly π^+) created at the target down the decay pipe. The horn magnets effectively reduce the transverse momentum of positive particles by 100 MeV per meter of longitudinal travel though the magnet [2]. Negative particles produced at the target are dispersed by the magnetic field.

Decay Volume

The decay volume starts 19 m downstream of the target. The decay volume is a 200 m long cylindrical tunnel. The diameter of the tunnel is 1.5 m, 2 m and 3 m for the following 10 m, 90 m and 100 m sections respectively. π^+ entering the tunnel have a momentum of 2-3 GeV/c. While traveling through the decay volume the π^+'s decay as displayed in Equation 1.12:

$$\pi^+ \to \mu^+ \nu_\mu \qquad (1.12)$$

The transverse momentum of the μ and the ν_μ after the decay are small compared to the momentum of the pion. Thus the neutrino is emitted within a few 10 mrad from the forward direction (toward Super-K). Table 1.2 summarizes the beam composition just after the decay volume according to the beam Monte Carlo. The muons produced in the pion decay are detected by the MUMON detector at the beam dump. This muon monitor measures whether the beam is on target.

Beam Aim

Figure 1.9 shows the neutrino flux and neutrino energies off the beam axis. As you can see from Figure 1.9 it is imperative that the beam is aimed at
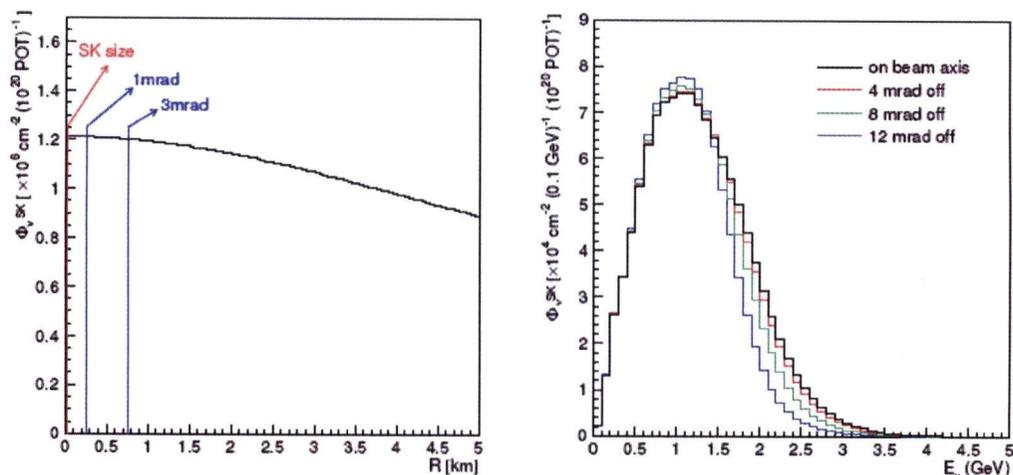
Figure 1.9: Monte Carlo simulation of the K2K neutrino beam without neutrino oscillation. The left gives the neutrino flux 250km downstream of the target at some transverse distance R from the Super-K detector. The right display gives the neutrino energy distribution on the beam axis and 4mrad, 8mrad and 12mrad off the axis [1].

Table 1.3: GPS Survey of K2K Target and Far Detector

K2K Component	Latitude	Longitude	Altitude
Target	$36°09'14.9531''N$	$140°04'16.3303''E$	70.218 m
Super-K Center	$36°25'32.5867''N$	$137°18'37.1214''E$	371.839 m

Super-K to within a milliradian to properly understand the flux and energy spectrum of the beam neutrinos. This has been accomplished through a GPS survey. Table 1.3 gives the locations of the target and the center of the far detector according to a GPS survey. Using this survey the required beampipe direction is determined to an accuracy of 0.01mrad [21]. The components of the K2K beam were aligned such that the beam is pointing at the center of the Super-K detector with an accuracy of 0.1mrad. The MUMON confirms the beam is lined up.
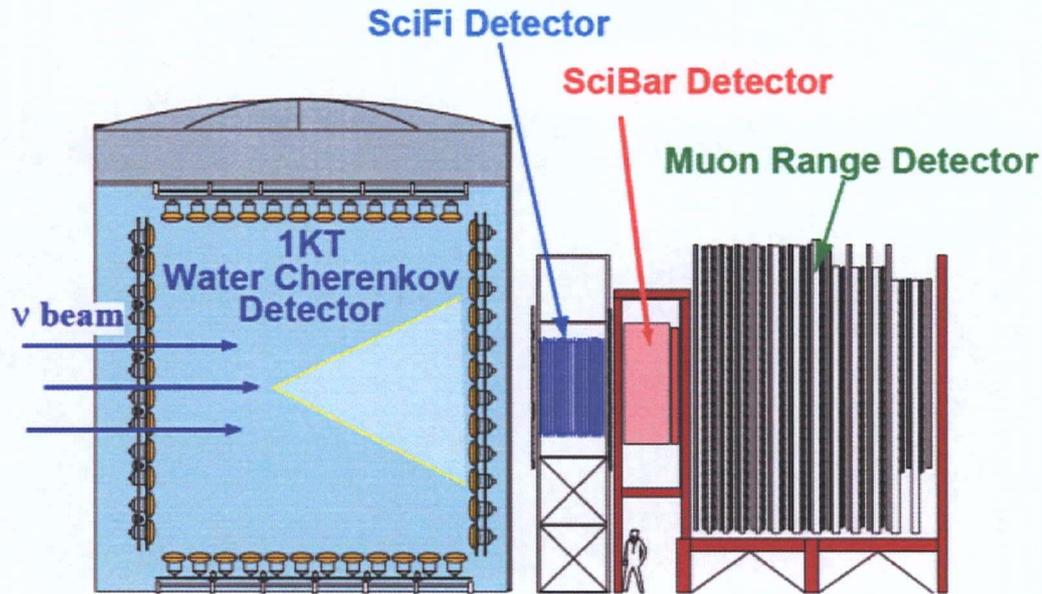
Figure 1.10: The Near Detector consists of four detector systems: The 1KT water Čerenkov detector, the SciFi, SciBar and MRD detectors [20]. The SciFi, SciBar and MRD together constitute the FGD system.

1.4 Near Detector

The near detector measures the ν_μ flux 300m from the production target along a line between the target and Super-K. Figure 1.10 shows the near detector components. The first part of the near detector heading along the particle beam is the 1KT water Čerenkov detector. Next is the SciFi detector, which is a water-based scintillating fiber detector. After the SciFi detector the neutrino beam moves through SciBar, a fine segmented, fully active scintillation tracker. Originally K2K was using a lead-glass calorimeter instead of SciBar. Last the neutrinos pass the Muon Range Detector (MRD). The SciFi, SciBar (previously Lead Glass Calorimeter) and MRD together are referred to as the Fine-Grained Detector system (FGD). This thesis concerns the calibration of the 1KT detector, thus I will focus on the 1KT here.

1.4.1 One Kiloton Water Čerenkov Detector

The 1KT detector is a smaller replica of the Super-Kamiokande (far) detector. The 1KT and the Super-K detectors measure the ν_μ flux and energy spectrum at both ends of the beam which are used to infer the oscillation parameters. Using the 1KT for the flux normalization is advantageous since the greatest uncertainties in the absolute flux measurement arise from the interaction cross-section for neutrinos with the detector material. Since the 1KT and the Super-K detector both use H_2O for the detector bulk this uncertainty cancels. The 1KT detector also gives a good high statistics measurement of neutrino-water interactions.

Physical Design

Figure 1.11 shows a schematic of the 1KT tank. The 1KT is a cylinder 10.8 m high and 10.8 m in diameter. Black and Tyvec sheets covering the metal support frame for the photomultiplier tubes separate the 1KT detector into two optically isolated parts:

- The Inner Detector (ID) is the volume inside the support frame. The ID forms a cylinder of 8.6 m in height and diameter. The ID is monitored by 680 20-inch R3600 Hamamatsu Photomultiplier Tubes. Table 1.4 summarizes the properties of the 20-inch PMTs used in the ID. Figure 1.12 gives a schematic view of a PMT. The 680 PMTs are arranged along the top, bottom and wall of the support frame on a grid spacing the centers of the PMTs 70 cm apart. The wall of the 1KT carries 456 PMTs organized in 38 columns of 12 PMTs each. The top and bottom are covered in 112 PMTs each.

- The Outer Detector (OD) is the water region between the support frame and the outer wall of the 1KT detector. This region is 1 m thick along the barrel and 0.6 m thick at the bottom of the tank. The OD is monitored by 68 8-inch PMTs that provide a veto against cosmic muons. Downgoing muons are rejected by the signal in the PMTs at the bottom of the 1KT.

The PMT arrangement in the inner detector is the same as in the Super-K detector giving a 40% optical coverage along the walls.
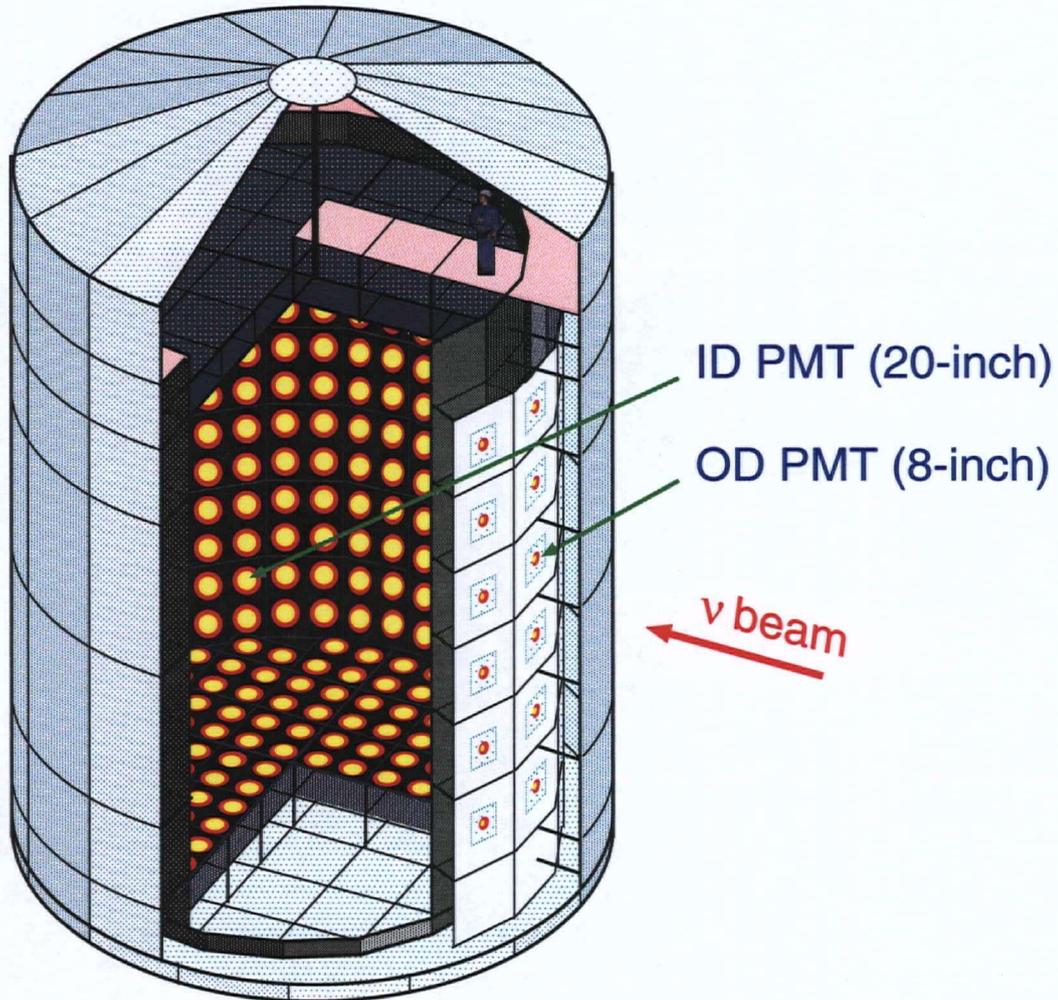
Figure 1.11: The 1KT is a water Čerenkov detector containing approximately 1000 tons of H_2O. Its inner volume is monitored by 680 20-inch Photomultiplier Tubes (PMTs). The outer detector volume is monitored by 68 smaller (8-inch) outward looking PMTs. The outward looking PMTs are mounted on the front third of the barrel (facing into the beam) and on the bottom of the support frame facing downward.

Table 1.4: Properties of the 20-inch Hamamatsu Photomultiplier Tubes (PMTs) used in the 1KT [1] and [3]

PMT Property	Value
Photo-cathode Area	50cm Diameter
Shape	Hemispherical
Window Material	Pyrex Glass 4-5mm
Photo-cathode Material	Bialkali (Sb-K-Cs)
Dynodes	11 stages, Venetian blind style
Quantum efficiency	22% at $\lambda = 390nm$
Sensitive Wavelength	300 to 600nm, peak at 390nm
Typical Gain	10^7 at ca. 2 kV
Dark Current	200 nA at 10^7 gain
Dark Pulse Rate	3kHz at 10^7 gain
Cathode non-uniformity	$< 10\%$
Anode non-uniformity	$< 40\%$
Manufacturer	Hamamatsu Photonics Corporation
Time Resolution for Single P.E.	$\sim$3ns
Time Resolution for Many P.E.	$\sim$0.5ns

< φ 520

photosensitive area > φ 460

(610±20)

~720

φ 254 ±10

φ 82 ±2

glass multi-seal

water proof structure

cable

φ 116

cable length

~70000

(mm)
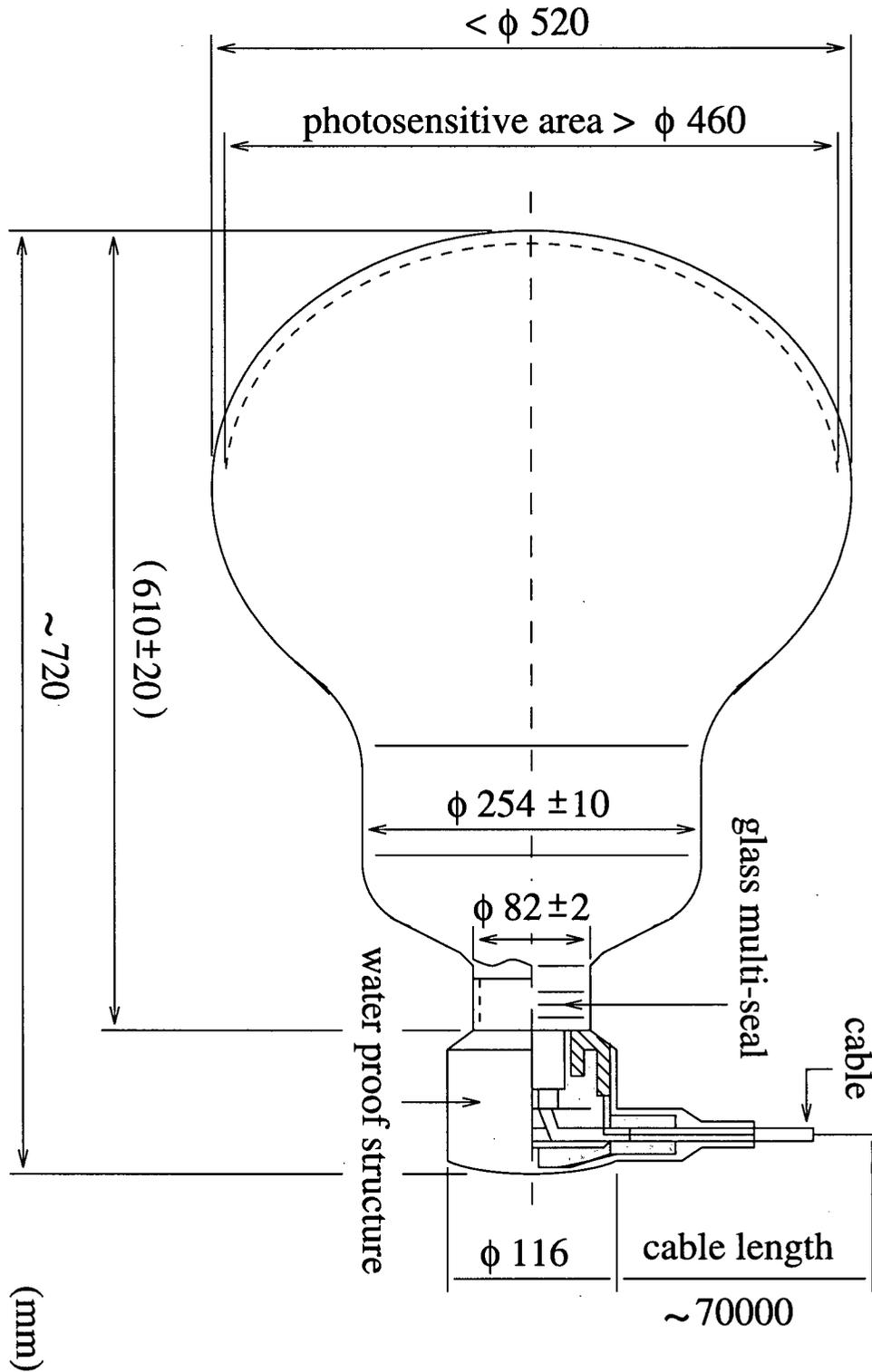
Figure 1.12: Schematic of the 20in PMT used in the 1KT detector
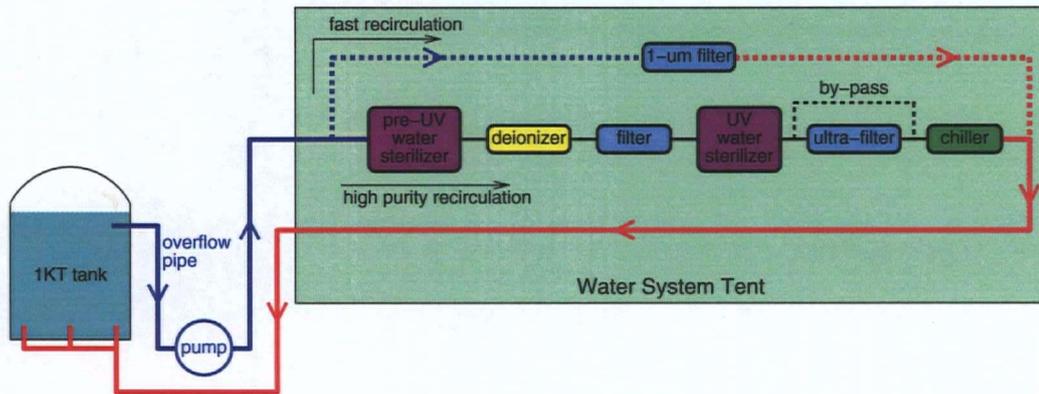
Figure 1.13: Schematic of the 1KT water purification system. Water is pumped through these filters at a rate of 20 tons per hour. Dotted lines are optional water pipes [1].

The Earth's magnetic field affects the PMT response. To cancel the geomagnetic field nine horizontal and seven vertical Helmholtz coils have been set up around the 1KT detector.

Figure 1.11 shows the room above the inner detector. This cavity permits access to the detector through a small ~1 m by 1 m hatch on the side of the upper deck.

The Water System

Particles dissolved in the detector's water volume will scatter the light traveling in the tank. Since scattering will change the timing signal from the PMTs in the 1KT the water must be as pure as possible. To ensure water quality the water in the 1KT is pumped through a series of filters at a rate of 20 tons per hour. Figure 1.13 is a schematic of the 1KT water purification system. A pump next to the 1KT in the near detector pit pumps the water out of the 1KT into the filter system. First the pre-UV and ultraviolet (UV) filters kill any bacteria in the water. Next metallic ions in the water are removed by a deionizer. Then a filter removes all particles larger than about 1 μm in diameter. Finally the ultra-filter removes particles larger then 10 nm in diameter. After the filtering process the chiller cools the water to 10°C.

The water purity is monitored by measuring the water's electrical resistivity. For regular operation the resistivity of the water is kept to 10 MΩ/cm.

The attenuation length of the water under these conditions was determined to be $\lambda = 50$ m using Čerenkov light (wavelength $\sim$390 nm) from cosmic rays [1].

The 1KT's Data Acquisition System

Figure 1.14 displays the general data flow for the data acquisition system of the 1KT detector. The raw signal from each PMT is transferred though a coaxial cable from the 1KT detector to an electronics hut. Sine the operation of the electronics is dependent on their temperature the electronics hut is always air-conditioned to keep the temperature below $25°C$.

PMTs are put into groups of 12. Next the signal from each PMT is split into four. The four signals lead into:

- Two independent analog-to-digital converters (ADCs). The conversion for the ADCs is 0.15 pC/count.

- A discriminator which sends its output to two time-to-digital converters. This discriminator also provides the timeout signal for the analog to digital conversion in the ADCs and TDCs. The discriminator threshold is set to a voltage corresponding to 0.3 photoelectrons, and the TDC conversion factor is 0.4 ns/count.

- The PMTSUM, which determines the analog sum of each PMT in a group of 12. All PMTSUM signals are added and sent to one Flash Analog to Digital Converter (FADC) with a 500 MHz sampling frequency and 8 bit resolution. The number of events in a spill are recorded by counting the number of peaks in the signal shape read out by the FADC.

The two ADCs and TDCs for each PMT channel are organized on Analog Timing Modules (ATMs) originally developed for Super-K. Each ATM holds the ADCs as well as TDCs for twelve PMTs and First In First Out (FIFO) data storage for each. The ATMs are organized into TKO modules as displayed in Figure 1.14. The TKO modules also hold a Super-Control-Head (SCH) data storage for the ADC and TDC signals from each ATM. Furthermore the TKO module has a Go/NotGo (GONG) module which tells the ATMs to store their data to the SCH if it receives a trigger 1.1 μs after the ATM gets hit with data from PMTs. Finally each ATM module has a discriminator that generates a rectangular voltage pulse 200 ns long and 10 mV
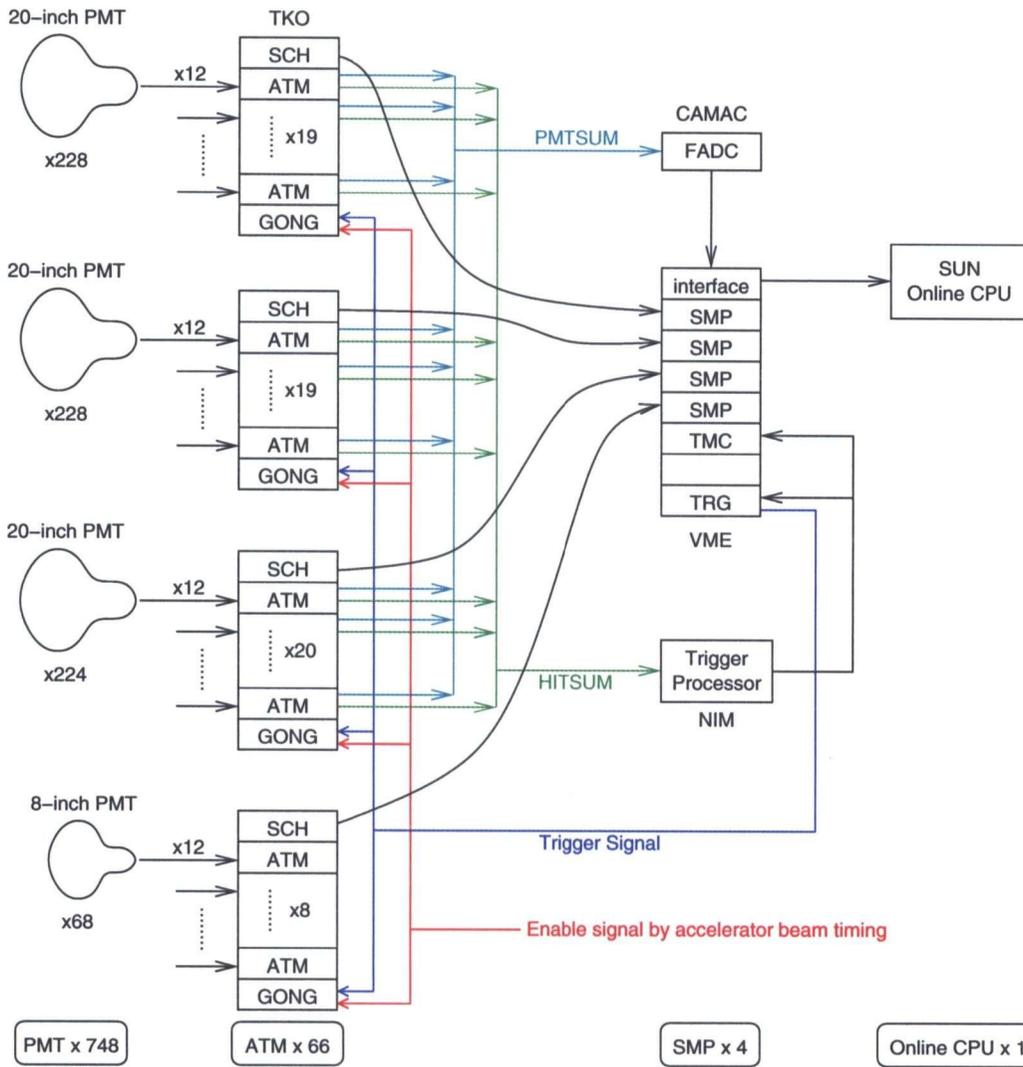
Figure 1.14: A flow chart displaying the data flow from the PMTs to the readout electronics[1].

Beam Coordinates   **Tank Coordinates**
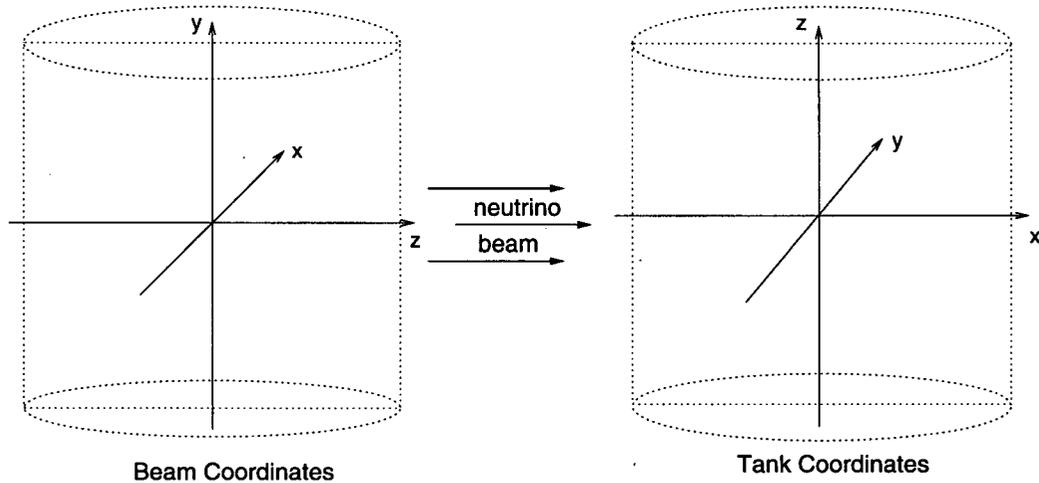
Figure 1.15: The beam and tank coordinate systems are important when working with the 1KT detector. In the figure the x-axis on the left and the y axis on the right point into the page.

high for each PMT that records a hit. This pulse is called the HITSUM and the combined HITSUM from all ATMs gives the number of hit PMTs (also called the occupancy) of the event.

For usual operation beam timing provides an enable signal synchronized with the beam spills letting the TKO modules (four crates containing the ATM modules for all the PMTs in the 1KT) receive data for 1.3 μs. The data taken for this thesis is all calibration data, and the beam timing signal is replaced by a trigger created by a photo diode pulsed by the calibration laser.

Four VME crates (one for each TKO module) are used to record the data from the SCH in the TKO modules. Finally, if more then 40 PMTs were hit the trigger crate enables the data read out and the computers read in the events. Since we may want to read out events with less than 40 hit PMTs for the optical calibration this trigger is not used here either, and instead all triggered events are read out.

1KT Coordinate Systems

Figure 1.15 shows the two coordinate systems that are important in the 1KT detector, the:

- Beam Coordinate System, and

- Tank Coordinate System

The tank coordinate system is used for our calibration analysis. The beam coordinate system is used for the regular data analysis in the 1KT tank and the official Monte Carlo.

Fiducial Volume

Figure 1.16 shows the three fiducial volumes that are used in the 1KT neutrino analysis:

- Volume A is a large cylinder aligned with the 1KT, 6m in height and 6m in diameter. Volume A is centered on the center of the 1KT.

- Volume B also is a cylinder centered on the center of the 1KT, but the axis of the cylinder is aligned with the neutrino beam. Volume B is 4m in length and 4m in diameter.

- Volume C is the upsteam half of volume B.

For neutrino data in the 1KT we consider events that have a vertex originating in fiducial volume C. Volume A is used to measure the neutrino beam profile and volume B is used to ensure the stability of the neutrino event rate.

1.4.2   The Fine Grained Detector

The fine grained detector (FGD) gives a neutrino flux and spectrum measurement independent of the 1KT water Čerenkov detector. The basic concepts of the FGD will be outlined here for completeness, but since the calibration of the 1KT only marginally depends upon the FGD this description will not be so detailed.

The fine grained detector measures all of the charged particles produced in neutrino interactions, which the 1KT cannot do very accurately, since some of the heavier particles are below Čerenkov threshold in the 1KT. The 1KT measures the neutrino flux to compare to the flux at Super-K. This the 1KT can do better than the FGD because the target material is the same as for Super-K thus cancelling the significant uncertainty in the neutrino interaction cross-section for the detector materials.
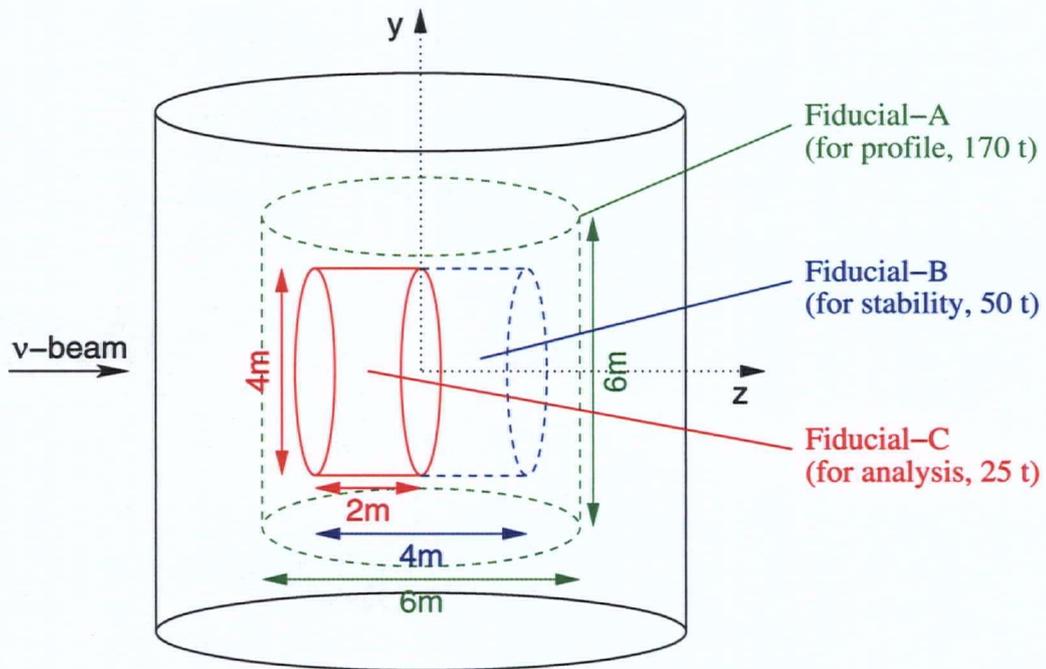
Figure 1.16: Only neutrino events that reconstruct in fiducial volume C are considered for the neutrino flux and energy measurement used in the K2K analysis [1].

Scintillating Fiber Tracker

The SciFi detector is composed of twenty 2.6 m by 2.6 m tracking modules containing two layers of horizontal and vertical scintillating sheets made of 0.692 mm fibers. The tracking layers are placed 9 cm apart. In between the 20 tracking layers 19 aluminum tanks contain a total of 6 tons of water. Charged particles produced in neutrino interactions are tracked using the scintillation light they cause in the fibers in the tracking layers. The scintillating fibers are read out by CCD cameras with image intensifiers.

Scintillating Bar

The Scintillating Bar (SciBar) detector was an upgrade to K2K replacing the lead glass calorimeter. A total of 14,848 scintillating bars, each 1.3 cm thick, 2.5 cm wide and 300 cm long, were produced at Fermilab [22] for use in the SciBar detector. Now they are arranged in 64 alternating layers of horizontal and vertical bars. This gives a $3 \times 3 \times 1.7$ m fully active detector volume. Wavelength shifting fibers guide the scintillation light produced by charged particles traveling in the SciBar detector to multi-anode photomultiplier tubes (MAPMTs) that read out the signal.

Muon Range Detector

The MRD is a range calorimeter composed of 864 tons of iron intended to stop muons products of neutrino interactions in the previous detector systems, in order to get the muon energy by its range. The metal is arranged in twelve 7.6 m by 7.6 m by 10 cm thick sheets. Around the iron sheets are 13 sets of horizontally and vertically arranged drift tubes. The 6632 drift tubes are filled with a gas mixture containing 90% Argon (Ar) and 10% Methane (CH_4). The drift chambers are read out by TDCs.

1.5 The Super-Kamiokande Detector

Figure 1.17 shows the Super-K detector which is located 1 km underground in the Mozumi mine of the Kamioka Mining and Smelting Co [23]. Table 1.5 summarizes the information on the Super-K detector.Like the 1KT the Super-K detector is a cylinder. The entire Super-K detector is 41.4 m high and 39.3 m in diameter. A cylindrical frame in the detector (36.2 m high and

Table 1.5: Basic Information on the Super-Kamiokande Detector

Detector Part	Statistic
Outer Dimensions	41.4m High, 39.3m Diameter Cylinder
Inner Dimensions	36.2m High, 33.8m Diameter Cylinder
Outer Water Mass	18,000 tons
Inner Water Mass	32,000 tons
Outer Monitoring PMTs	1,885
Inner Monitoring PMTs	11,146
PMT Readout Timing Resolution	0.40 ns (1.2 μs Range)
PMT Readout Charge Resolution	0.2 pC (550 pC Range)
Energy Range	5.7 MeV - 8 GeV
Energy Resolution	2.5% (at 1 GeV)

33.8 m in diameter) hold 11,147 PMTs looking inward into the inner detector volume. A similar but larger frame surrounding the first frame holds 1885 PMTs looking outward at the outer detector volume. Each of the two frames are covered in opaque sheets, optically isolating the inner and outer detector, but also creating a 55 cm dead region between the two. Super-K is sensitive to $e^-(\nu_l, e^-)\nu_l$ and $X(\nu_l, l)X'$ interactions.

1.6 The Global Positioning System

To distinguish K2K beam neutrino events from atmospheric neutrinos at the far (Super-K) detector the GPS system is used to provide an accurate time stamp between Super-K and KEK. A 1 Hz timing signal from the GPS system is sent to calibrate a local clock at both KEK and Super-K. The local clocks operate at 50MHz giving a 32-bit time signal that is used as a time stamp on the recorded events. This time stamp is used in the analysis to tell beam events from atmospheric events, relying on the spill times at KEK to predict the neutrino arrival time at Super-K.
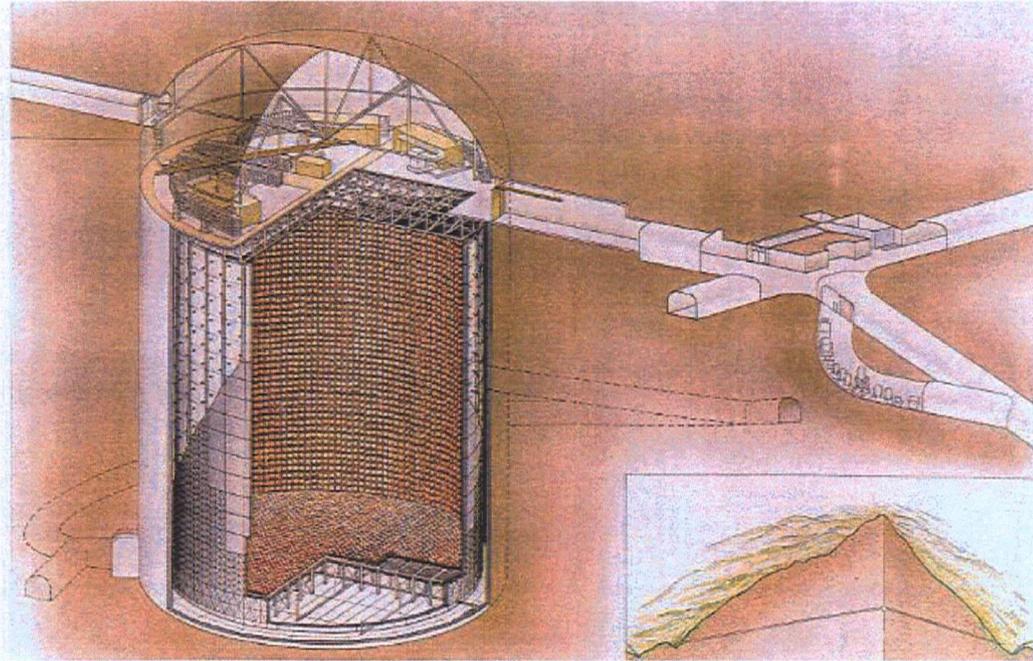
Figure 1.17: The Super-Kamiokande Detector

Chapter 2

1KT Exploration With A Diffuser Ball On A String

The 1KT detector has previously been calibrated using a

- Laser diffuser ball to get the TQ-Map,

- Xenon lamp diffuser ball to equalize the PMT Gain,

- Comic ray muons to determine the energy scale,

- Nickel source to measure quantum efficiencies, and

- Laser beam to calibrate for scattering and reflection.

The TQ-map is a time correction for each PMT that is supposed to correct differences in the time signal arising from signal travel time in the PMTs and wires as well as any effects the charge deposited in the PMT may have on the measured time. The setup to generate the TQ-map is the same as for this laserball study (and will be described in Section 2.1). For the TQ-map the laserball is kept at the center of the 1KT. In the 2003 TQ-map it was noticed that the laserball seemed to be shifted by a few centimeters in the z-coordinate (tank system). One motivation for this laserball study is to find out whether this is a problem with the reconstruction or with the laserball placement.

The xenon lamp study uses a setup similar to the laserball, just that instead of the laser a xenon lamp is mounted on the optical table and a different diffuser ball is used. To be able to calibrate the PMT gain throughout the 1KT, first 103 of the 680 PMTs in the inner detector had their voltage supply calibrated to give the same gain before they were installed. A ratio of the charge signals from the uncalibrated PMTs over the calibrated PMTs is used to adjust the PMT voltage to set all PMTs to the same gain.

Muons from cosmic rays are put in two categories for the cosmic ray calibration. Vertically travelling muons are tagged by the coincidence of

two scintillator pads set up above the 1KT (over the CRP described in Section 3.2). Horizontally travelling muons are identified by a coincidence between a signal in the upsteam part of the outer detector and a veto trigger plane set up downstream of the 1KT.

The laser described in the next section was used to shine a laser beam down the Cosmic Ray Pipe parallel to the central axis of the 1KT. From comparing the data to the 1KT Monte Carlo simulation of a light beam, Rayleigh scattering and the reflection of the PMTs and the black sheets isolating the inner and outer detectors are inferred. Further investigation of the timing of MC events as compared to real data reveals a timing difference between the top and bottom PMTs [24]. The observed timing difference motivated this laserball study to determine what the impact on the optical position reconstruction was.

2.1 Detector Setup for Optical Calibration

To take calibration data using the diffuser ball (or laser ball) an optical table is set up in the 1KT control room at KEK. Figure 2.1 shows a schematic of the laser setup for optical calibration using the laserball. A VSL-337 air cooled nitrogen laser is set up on the optical table. The laser receives a 10Hz external trigger signal and fires a 4 ns pulse of light at $\lambda = 337$ nm [25]. A laser dye is used to tune the wavelength of the laser-light to 390 nm. The laser light is sent though a beam splitter that sends half the laser light through a fiber-optic cable into a photo diode with a fast response to the laser light. The signal from the photo diode is sent to trigger electronics of the 1KT to supply a timing reference and start the data collection. The other half of the laser light goes through a series of filters and though a 200 m long fiber optic umbilical cord into the diffuser ball. The diffuser ball or laserball scatters the light isotropically through the tank. The diffuser ball is a glass sphere of approximately 3 cm diameter that contains MgO impurities and silica gel to scatter the light from the laser isotropically. The fibre optic umbilical enters the laserball through a 2.5 cm deep and 4 mm wide hole, and is held there by transparent, waterproof glue.
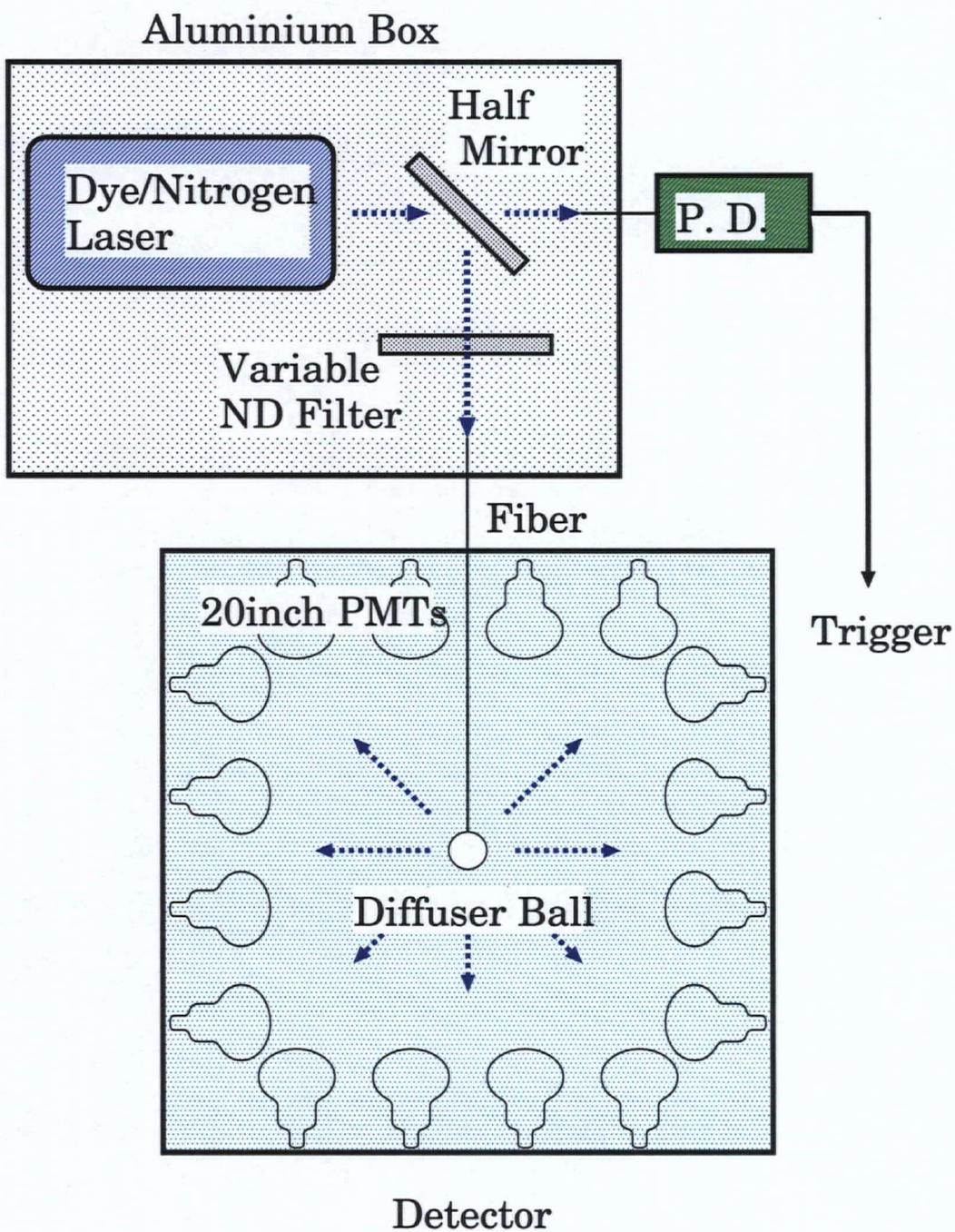
Figure 2.1: The setup for the optical calibration using a laserball. Laser light passes through a beam splitter, letting half the laser light go into the 1KT tank and reflecting the other half into the photodiode, which provides the timing trigger. The photo diode is labelled P.D. in the figure.

2.1.1   Laserball Data

While the beam was shut down for the K2K experiment in October 2003, July 2004 and June 2005, the Canadian K2K group took some data using the above setup. In October 2003 only two runs were taken, one at the center and one close to the top of the 1KT. The data in July 2004 was taken at all locations the ball on a string could reach. Various runs were taken along the entire vertical axis of the 1KT. The position of the laserball was also measured more carefully since the uncertainty in the nominal position of the previous data made further conclusions about the optical reconstruction impossible. The final set of laserball runs were taken after the manipulator data run to provide an absolute positioning reference for the manipulator ball positions.

For the 2004 and 2005 laserball data we took multiple runs at each position in the 1KT using different filters for the laser light. Using these filters the laser light intensity was varied between:

- Low occupancy: Most PMTs are not hit, and those PMTs that are hit usually see a single photoelectron. For this analysis any run with PMTSUM signaling less than 110 PMTs is considered low occupancy. That corresponds to less than 120 photoelectrons (pe's) in the 1KT.

- Medium occupancy: Most PMTs in the 1KT are hit by at least one photon ($110 \leq PMTSUM < 390$ that is 120 to 580 pe's) .

- High occupancy: All PMTs in the 1KT are hit with many photons ($PMTSUM \geq 390$ that means 580 or more pe's).

All data taken is summarized in Appendix A. Note that the high occupancy runs with the given cut on PMTSUM have an average number of hits of 500 to 680 PMTs in an event.

2.2   Optical fit for Laserball Position

The position of the laserball is determined run by run. A timing histogram integrating over the entire run is formed for each PMT. Since the PMTs vary in their distance from the ball we subtract an estimated time of flight for light to go from the nominal position of the ball to the PMT. This localizes all

the timing peaks around 1000ns. The assumed speed of light in water is 21.66 cm/ns at $\lambda = 390$ nm.

The histograms record the timing information in 0.1 ns bins from 900 ns to 1100 ns. An integration gate 4 ns wide is slid across the histogram to find the timing window with the largest number of hits inside the integration gate. The peak is then determined by taking the mean of the channels in the integration gate. An uncertainty on this mean is estimated by taking the width of the peak inside the window as measured by the standard deviation over the square root of the number of events in the time window. Figure 2.2 shows an example using a 10 ns wide integration gate. Integration gates of different widths were tested. In Section 2.3.1 the effect of the width of the integration gate will be discussed further.

Once the timing peaks for each of the histograms are determined we add the estimated time of flight back to the result. Now a χ^2 minimization is run to fit the ball position to the set of 680 PMT times for the run. Figure 2.3 shows that the time of flight from the ball to each PMT is given by:

$$t_i^{th} - t_{off} = \frac{d}{v} = \frac{|\vec{x}_i^{pmt} - \vec{x}^{ball}|}{v} \qquad (2.1)$$

where $\vec{x}_{ball}$ is the fit position of the ball, $\vec{x}_{PMT}$ is the position of the PMT under consideration and $v = 21.66$ cm/ns is the group velocity of light with wavelength 390 nm traveling through water. t_i^{th} is the time expected for PMT number i to be hit and t_{off} is the time offset between the photodiode trigger and the point at which the laser light leaves the laserball. Hence we minimize:

$$\chi^2 = \sum_{i=1}^{N_{pmt}} \left(\frac{t_i^{pmt} - t_i^{th}}{\sigma_i} \right)^2 \qquad (2.2)$$

by varying $\vec{x}^{ball}$ and t_{off}. Here N_{pmt} is the number of PMTs used in the fit, t_i^{pmt} is the time measured by the PMT and σ_i^2 is the sum of the variance in the mean of the timing peak of the PMT plus a systematic error in the time charge correction:

$$\sigma_i^2 = \frac{\sigma_{pmt,i}^2}{N} + \sigma_{sys}^2$$

Where $\sigma_{sys} = 0.4$ ns is estimated by looking at the variance of the PMT times during one run. To find the error in the reconstructed position, we divide the 680 tubes into N non-overlapping subgroups selected isotropically thoughout the 1KT tank, where N = 2, 3, 4 ... 40. We fit the ball position

Figure 2.2: A 10ns wide integration gate slides across the histogram containing all the time-of-flight-adjusted PMT times in the run for a single PMT. In the time range with the largest number of events inside the gate we calculate the mean and $\sigma/\sqrt{N}$ to be the time and uncertainty on that time estimate. The picture shows normalized high and low occupancy timing histograms.
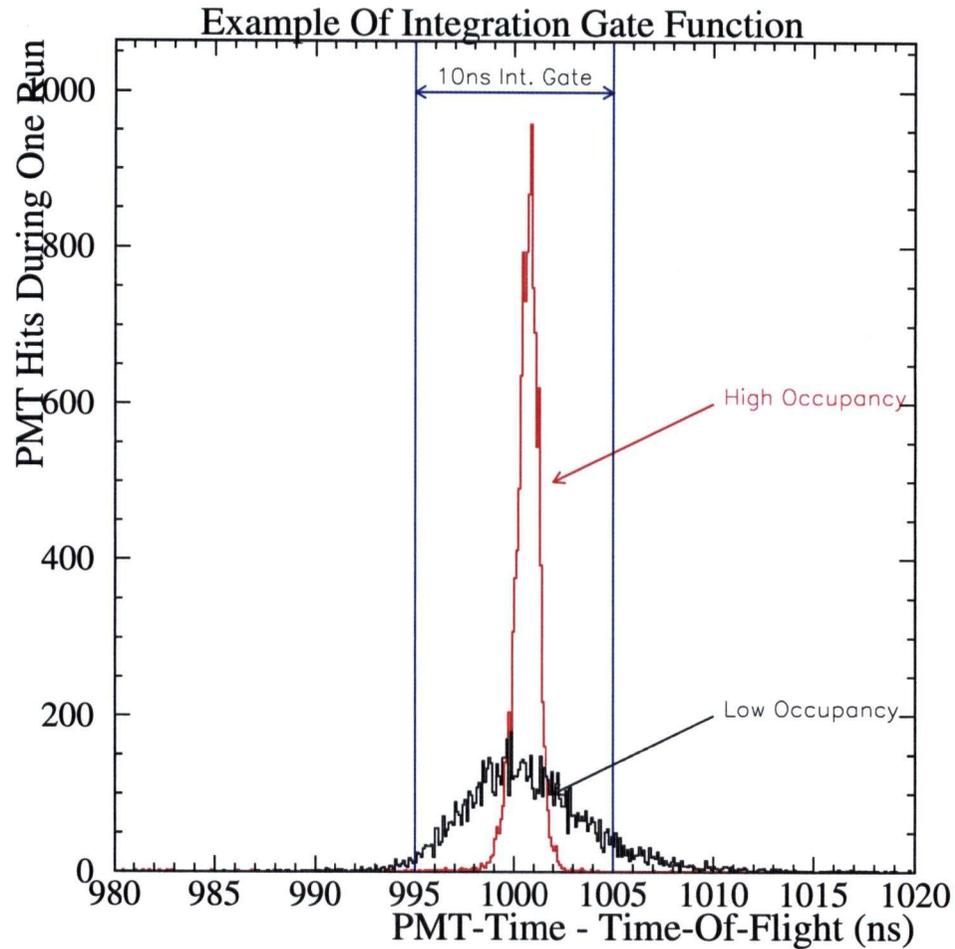
Figure 2.3: Optical Fitting for the Laserball Position
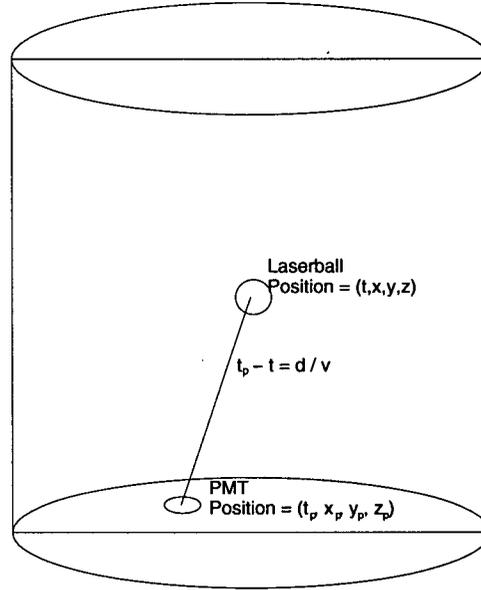
using the N subgroups, then calculate the variance of the N fitted positions. Next we fit the plot of the fitted position variance versus N to the function:

$$\sigma(N) = \sigma_0 \sqrt{N} \qquad (2.3)$$

where N is the number of groups, and σ_0 is the uncertainty for a single group of 680 PMTs (the result used for the ball position). The uncertainty on the variance at the value of N is given by:

$$\Delta\sigma(N) = \frac{\sigma(N)}{\sqrt{2(N-1)}}$$

Figure 2.4 shows $\sigma(N)$ for one sample run. The results from using every 12th, 24th, or 36th PMT are anomalous because this selects exactly one ring of PMTs along the 1KT wall, and so do not give isotropic subgroups. Thus we ignore the results from using 12, 24, and 36 subgroups (by assigning them a very large error). Once we understand this anomalous behavior Equation 2.3 fits the data exceptionally well.
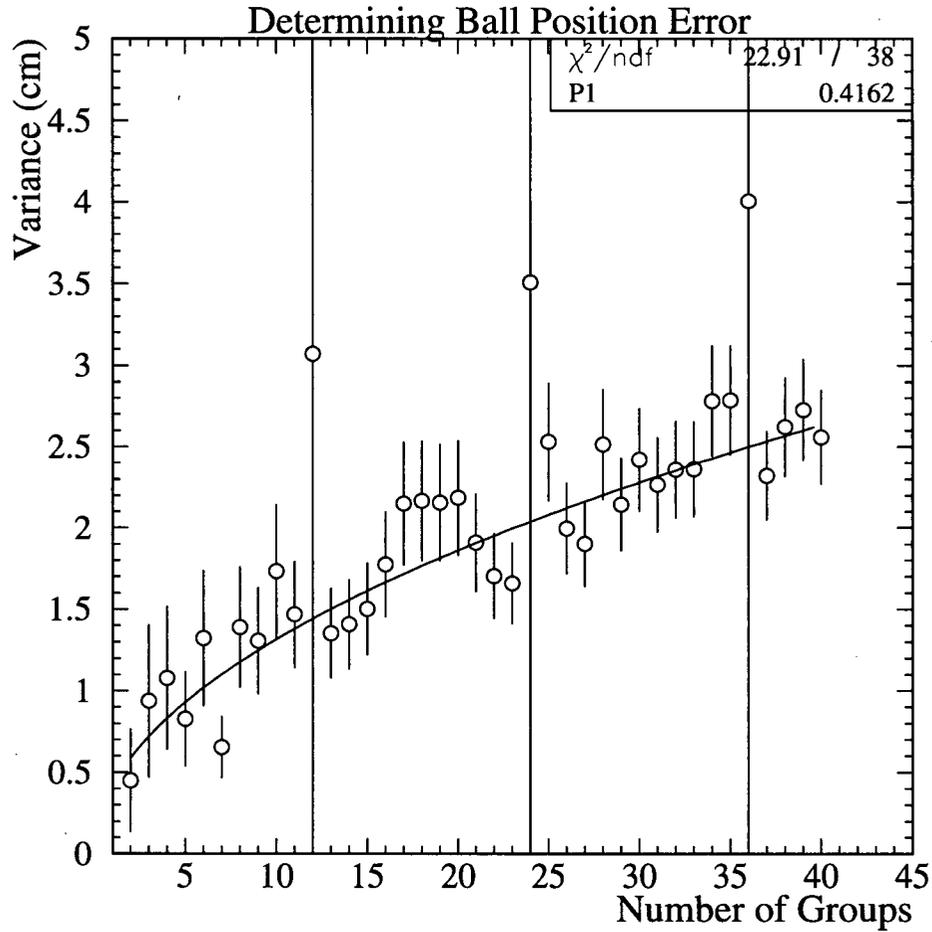
Figure 2.4: The error on the laserball position is calculated by fitting to the variance of position fits using subgroups of PMTs. The error is given by the fit parameter $\sigma_0 = P1$, which is the extrapolated uncertainty for a single subgroup of 680 PMTs.

2.3 Position Bias and the Time Charge Correction

2.3.1 Width of the Integration Gate

To choose the proper size for the integration gate we must look at the time histograms used to determine the PMT timing peak. Figure 2.2 shows the timing histograms for a low and a high occupancy run. The figure also shows a 10 ns integration gate. The high occupancy peak does not show a scattering tail while the low occupancy peak does. This is expected since in a high occupancy run each PMT gets hit by many photons and the electronics will register the first hit as the time on the PMT. Thus it is likely that in a high occupancy run the PMTs get hit by light that has not been scattered. In a low occupancy run each PMT is hit by about one photon, thus for some fraction of the PMT hits we should see scattered light only. The scattered light will not travel a straight path to the PMT but will hit the PMT a few nanoseconds after direct light. Thus the large integration gate will be pulled to a higher time by the scattering tail in low occupancy runs. A small integration gate will be influenced by statistical fluctuation, especially in the low occupancy regime.

The integration gate used initially was taken to be 20 ns wide. This resulted in a strong scattering effect for low occupancy data. Using the 10 ns gate displayed in Figure 2.3 reduced this effect. After closer examination of the PMT histograms a 4 ns gate was used which eliminated the scattering tail completely, but is unaffected by statistical fluctuations which are of the order of a few 0.1 ns.

2.3.2 Time Charge Correction Problem

Early analysis of the timing calibration data encountered many problems. Figure 2.5 shows the results of the first reconstruction using the 10 ns gate. The most obvious result is that the ball reconstructs 10 cm higher than we measured. The next is that the medium and high occupancy data show a significant (ca. 2%) slope. The offset could be explained by a simple mismeasurement of the reference mark on the wire suspending the ball (Appendix A explains how the nominal position is determined). The slope in the line fitted to the reconstructed positions shows that the fitted ball position is in fact closer to the center than it should be. Since this slope only depends on how
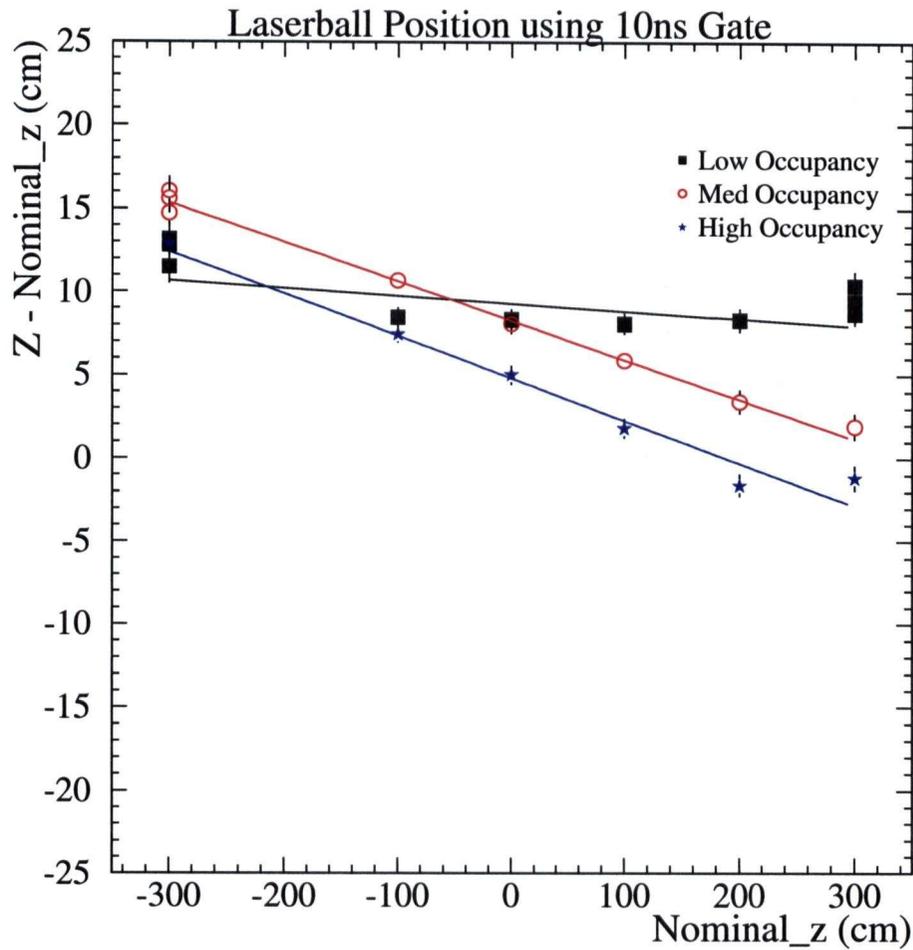
Figure 2.5: When comparing the position fitted using the 10ns gate to the nominal position we find that all measurements are displaced by approximately 10cm. Medium and high occupancy data also shows a slope. The data plotted here is from the 2004 data set with the old TQ-map.

the nominal position measurements are done relative to each other there is no simple explanation for the slope. Since the charge deposited in PMTs closer to the laserball is greater than in those far away the slope suggests a problem with the time-charge correction for the 1KT detector.

This prompted Dr. Shaomin Chen, who is in charge of the time charge correction for both the Super-K and the 1KT detector, to redo the TQ-map in 2004. The TQ-map is a correction to the PMT timing signals that incorporates PMT to PMT differences in signal travel time (due to cable length differences) and effects on the measured time from the amount of charge deposited in the PMT. The PMT times are measured in a similar way to the method used for this analysis. The TQ-map uses a 100 ns integration gate to find the mean and RMS of the timing peak. The final PMT time is measured by taking the mean of all events within a $^{+2.0}_{-1.5}\sigma$ window around the previous mean. The new TQ-map uses a 50 ns window for this calculation. Furthermore the new TQ-map restricts the charge bin measured in different runs to be similar to the average charge deposited in the 1KT. Using this cut avoids using PMTs that have a high fluctuation of the secondary electrons produced in the low occupancy runs in the high charge correction from the TQ-map. It is important to do this since, as explained before, the high occupancy data is not as affected by scattering as the low occupancy data. Finally a new pedestal correction was used in the TQ-map generation to eliminate some low charge anomalies in some PMTs.

Along with the revision of the TQ-map the constant characterizing the buffer amplification for the PMTs was corrected as well. Figure 2.6 shows the result of the position reconstruction with the new TQ-Map and the corrected buffer amp constant. The low and high occupancy runs now agree relatively well with the nominal position. The medium occupancy runs however show a significant slope.

2.3.3   Reconstruction Bias

Even with the reworked TQ-map and the corrected buffer amp constant, Figure 2.6 shows some anomalies. The medium occupancy data has a strong (1%) slope indicating that the data reconstucted closer to the center than it should have. The low and high occupancy data agree and show an insignificant (0.2%) slope in the opposite direction of the medium occupancy data (ie. the fitted positions are closer to the wall then they should be).

To see if the bias in the results from the laserball study can be explained,
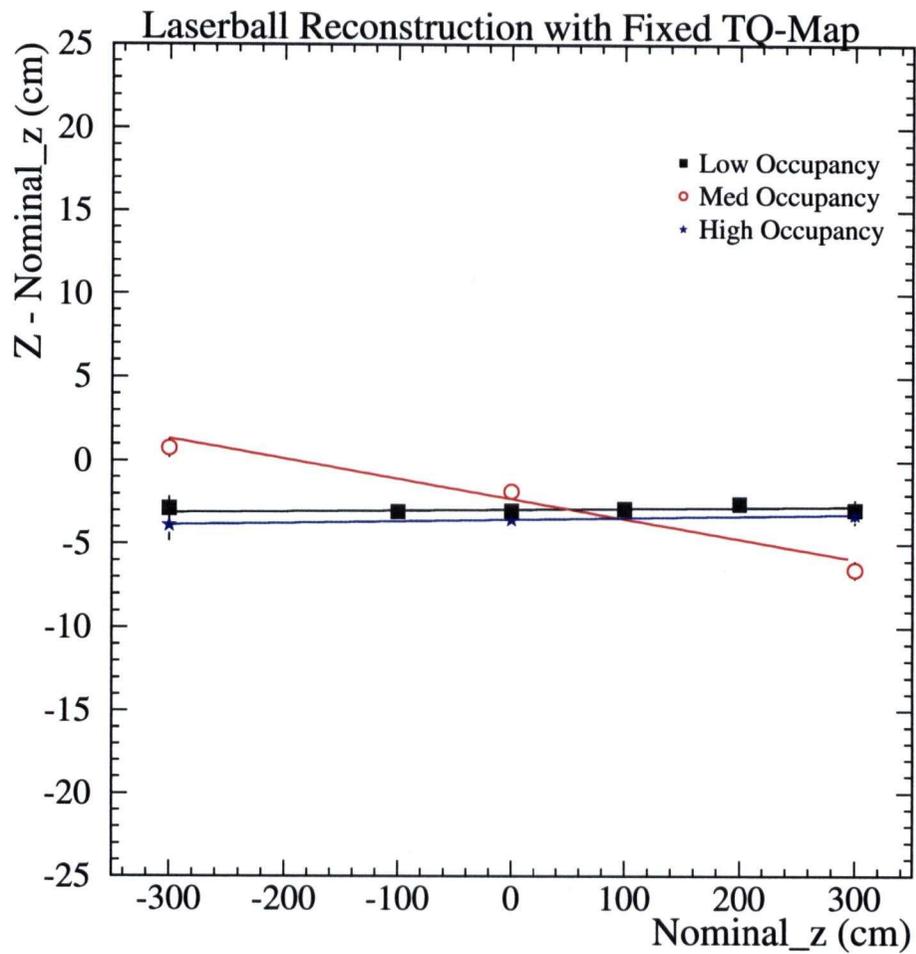
Figure 2.6: The reconstruction as in Figure 2.5 but using the new TQ-map and new buffer amp constant, for the data from Spring 2004. The slope seen in the medium occupancy data here is different from what we see in the manipulator data later; this may be because we changed what we call low, medium and high occupancy.

the full 1KT Monte Carlo was run at the positions we placed the laserball. Figure 2.7 shows the results of running the position reconstruction on data generated with the 1KT Monte Carlo. Here the nominal ball positions are exact, so any deviation is due to problems in the reconstruction. In the first laserball simulation we suppressed scattering and absorption, thus the mean times for each of the PMTs should not be pulled by scattering. Later we turned on scattering and eventually a slope similar to the one seen in the medium occupancy data can be observed. All the MC data was run simulating low occupancy which should be more sensitive to scattering. That is, in medium and high occupancy runs the PMTs are struck by many photons, thus chances are that the PMT will be hit by at least one unscattered photon in each light pulse. Since the TDC will record the arrival time of the first signal, our analysis should effectively eliminate scattering for high occupancy and reduce it for medium occupancy. However the slope in the medium occupancy data is opposite to what can be explained by scattering. Furthermore if scattering was the problem it should be most prominent in the low occupancy data not medium occupancy. Running the MC on positions throughout the entire tank volume showed that ball positions along the x and y axis of the tank coordinate system reconstruct well (ie. there is no slope or offset in plots similar to Figure 2.7 for the x and y axis).

2.4   Conclusion on Laserball Study

Since the Monte Carlo position reconstruction does not match the data from the laserball either the analysis is flawed or we cannot trust the Monte Carlo results. This means it would be of interest to study the entire detector volume (x, y and z axis) for the bias effect seen in Figure 2.6 to see how the Fiducial Volume of the 1KT is affected.

Furthermore the uncertainty in the position reconstruction is around 1cm in the x, y and z directions, so to make any further conclusion we need to locate the laserball with a precision of 1cm in each direction.
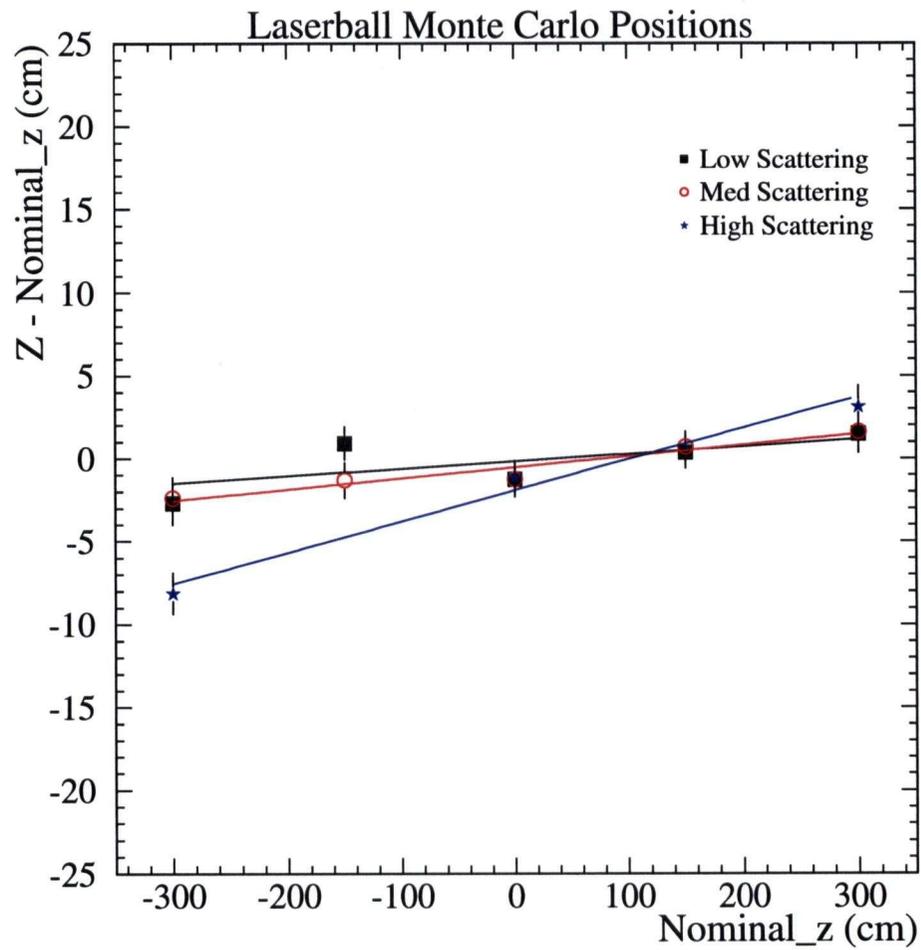
Figure 2.7: Results of the laserball position reconstruction using the 1KT Monte Carlo. Amount of scattering is varied. The ball positions are known precisely.

Chapter 3

Manipulator Construction

The manipulator is a robotically controlled arm that maneuvers the laserball throughout the 1KT tank, including off axis positions.

3.1 Motivation

The study of the 1KT tank using the laserball deployed along the central axis showed unexpected reconstruction biases as evidenced by the slope in the position reconstruction. We need to understand the effect on the fiducial volume of the 1KT since the fiducial volume error is one of the major errors on the far-near extrapolation. Section 2.4 described the basic goals for the construction of the manipulator arm, which are:

- Reach the entire 1KT tank volume,

- Locate the laserball to within 1-2cm in each dimension, and

- Do not touch the any PMTs in the 1KT.

While making all this possible we cannot change anything in the 1KT's current setup.

3.2 Hardware

As displayed in Figure 1.11 the only access to the 1KT tank is from above the detector volume. The 1KT detector volume itself has two possible access points from the access room above the detector:

- The central laserball access hole (center of the tank), and

- The cosmic ray pipe access port (CRP) (x = -70 cm ,y = 70 cm in tank coordinates).

Due to the lack of access points along the side of the 1KT a setup using three wires controlling the ball from three points around the top of the tank is impossible. The remaining option is an arm with mobile sections inserted in one of the access points. This means the central laserball access hole cannot be used since it leads though a curved pipe. Hence we must lower our assembly into the tank through the CRP access port.

Figure 3.1 shows a schematic of the manipulator when deployed in the 1KT tank. The manipulator is lowered into the 1KT tank from the cavity above the detector volume through the CRP access hole. The first problem is that the 1KT tank is 8.6 m deep and has a diameter of 8.6 m, thus the manipulator needs to be long so that it can explore the detector volume. The manipulator also needs to be rigid so we can achieve the desired 1cm position resolution in each direction. But the room above the 1KT is 1.35 m high along the outside of the cavity and 2.7 m high at the center of the room. Furthermore the CRP port lies beneath a support structure holding up the roof of the 1KT tank, where a pipe in the center of the cavity supports the roof through a number of small pipes. The CRP access port itself is 1.5 m long and 0.30 m in diameter. That means the longest section of the manipulator can only be about 2 m long to fit into the 1KT.

To meet the above challenges we use this design for the manipulator arm:

- A 5 m long x 15 cm wide vertical section (VS). To be able to insert the vertical section into the 1KT though the CRP port under the roof and roof support the 5 m VS needs to be divided into three parts, that are connected through hinges, such that the VS may bend. To allow the VS to be rigid during the operation of the manipulator the three sections are clamped together once in place

- Three moving sections:

  - A-Arm: 2.00 m long x 8 cm wide rigid section, attached to VS, that may rotate through 360° in a vertical plane

  - B-Arm: 1.50 m long x 5 cm wide rigid section, attached to A-arm, that may rotate through 360° in a vertical plane

  - C-Arm: 0.20 m long x 5 mm wide rigid section, attached to B-arm, that may rotate through 360° and holds the laserball

The entire manipulator arm is held by a turntable, which may rotate through 360° in azimuth. The manipulator and turntable are held by a structure

* circles denote travel of individual arms and the total combined reach
* preliminary length of inner arm = 1500mm
* preliminary length of centre arm = 1370mm
* preliminary distance from outer arm hinge centre to outside of laser ball = 130mm
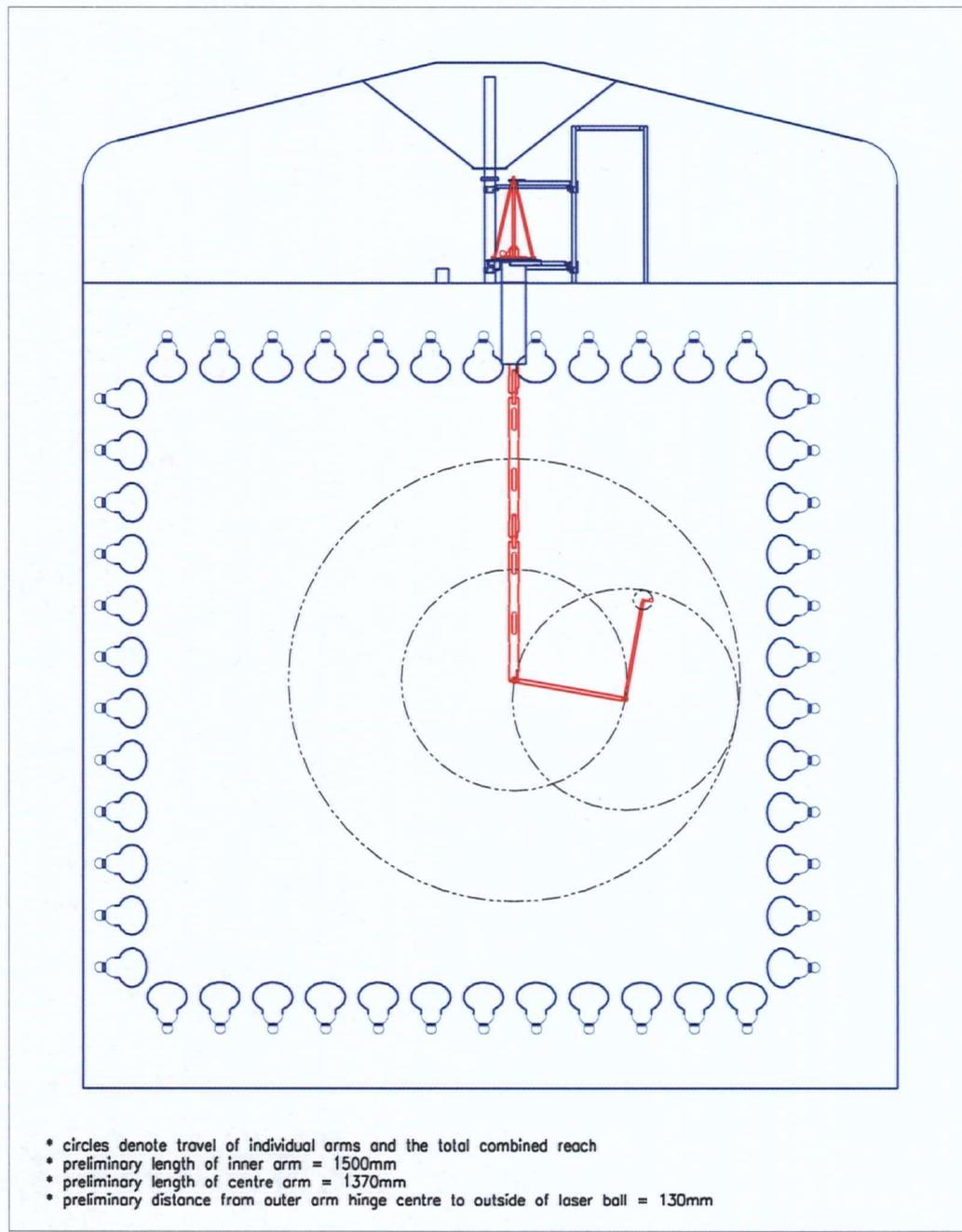
Figure 3.1: A schematic of the manipulator arm deployed in the 1KT tank.
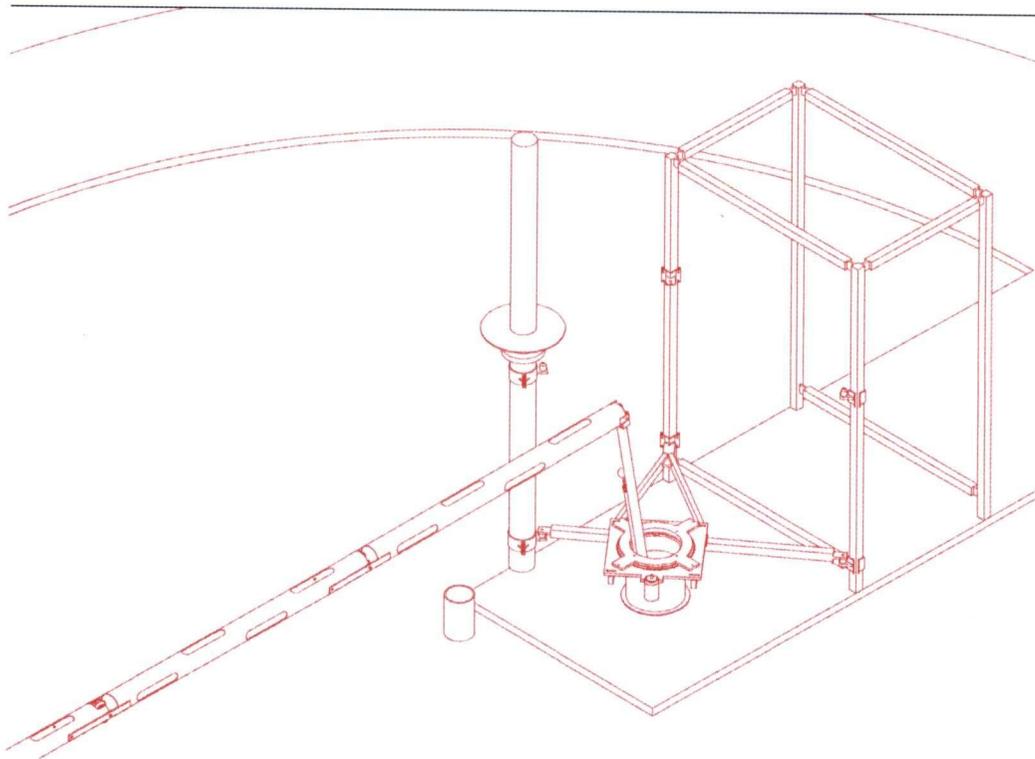
Figure 3.2: Concept drawing of the manipulator support structure while the manipulator is being inserted.

clamped onto the support beam for the roof of the 1KT and a cage that has already been set up to hold equipment for the CRP. Figure 3.2 shows how this support is set up in the cavity above the 1KT detector. The fact that the vertical section is cut into three pieces that have to be attached rigidly to each other causes some issues that will be addressed further in Section 3.5.

Since the manipulator will operate in ultra pure water the arms are made of stainless steel. To make it possible to drive the arms they are designed with waterproof cavities such that the arms are neutrally buoyant. A Galil motor controller drives two large and one small Pittman brushed DC motors with optical encoders, and output shaft gearboxes supply the driving force for the A, B, and C arms. The motors are mounted on the turntable above the water. The small motor drives the C-arm. The driving force from the motors is transmitted down the manipulator using a polyurethane chain. To minimize backlash the polyurethane chain is used only around the sprockets that pass
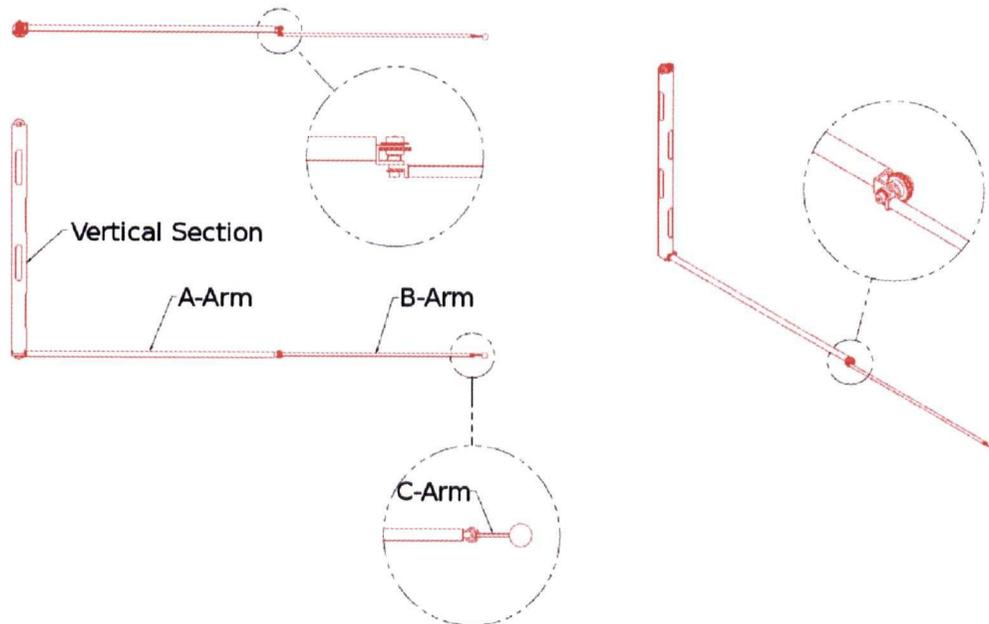
Figure 3.3: The joints between the moving sections of the manipulator arm are shown with the sprockets that are used to drive the arm with polyurethane chain supplying the drive force from the motors.

on the force from the chain. These sections of chain are linked by stainless steel wires. Linked sprockets are used to move the driving force down the manipulator. Figure 3.3 shows the sprockets used at the manipulator joints to transmit the driving force to the arms. Finally the turntable is driven by a large Pittman motor mounted on the turntable support.

To reduce reflection off of the arms the A, B, and vertical section of the manipulator are wrapped in black plastic. Strips of the plastic are wrapped around the A and B arms under the drive chains and secured with thin nylon rope. Each of the three pieces of the vertical section are also wrapped in black plastic sheets secured using white plastic tie wraps.

3.3 Electronics

Figure 3.4 displays the organization of the control system for the manipulator. We interact with the manipulator through a Graphical User Interface

Table 3.1: Specifications for the Pittman motors used to drive the manipulator. Encoder Accuracy is given in counts per turn.

Property	Large Motor	Small Motor
Model number	GM9234S033-R1	GM8724S029-R1
Driving voltage	24V, DC	24V, DC
Gear ratio	218.4:1	187.7:1
Encoder accuracy	500	500

(GUI) designed with Matlab. The GUI communicates with a Maximum Integrated Data Acquisition System (MIDAS) online database (ODB) [26]. The database can also be accessed directly through a database editor. Two front end programs continually scan the ODB for updates. The motor controller front end (feMotor) looks for updates to the manipulator destination in the database and communicates these to the Galil motor controller. The motor positions are determined though the internal motor encoders. For the motors driving the A, B, and C arms an auxiliary encoder is installed on the sprocket attached to the motors. The auxiliary encoder for the turntable motor is attached at the top of the tripod, above the ball bearing holding the manipulator. The auxiliary encoders provide a second measurement of the arm positions that does not suffer from backlash within the motors, but is affected by backlash in the polyurethane chains. Both sets of encoder measurement are read into the MIDAS ODB through the motor controller and then the motor front end.

In total four systems are used to track the manipulator position, to be absolutely sure of the manipulator position:

- Motor encoders,

- Auxiliary encoders, and

- Two inclinometer systems.

The inclinometer systems denoted Limit and Safety are described in the next section. The motor encoders are quadrature encoders that record the motor position with four disks having 500 counts per turn giving a total of 2000 steps every 360°. The motor encoders suffer from motor and chain backlash. The auxiliary encoders are attached to the sprockets on the motor drive shaft. That means they only suffer from chain backlash. The auxiliary encoders
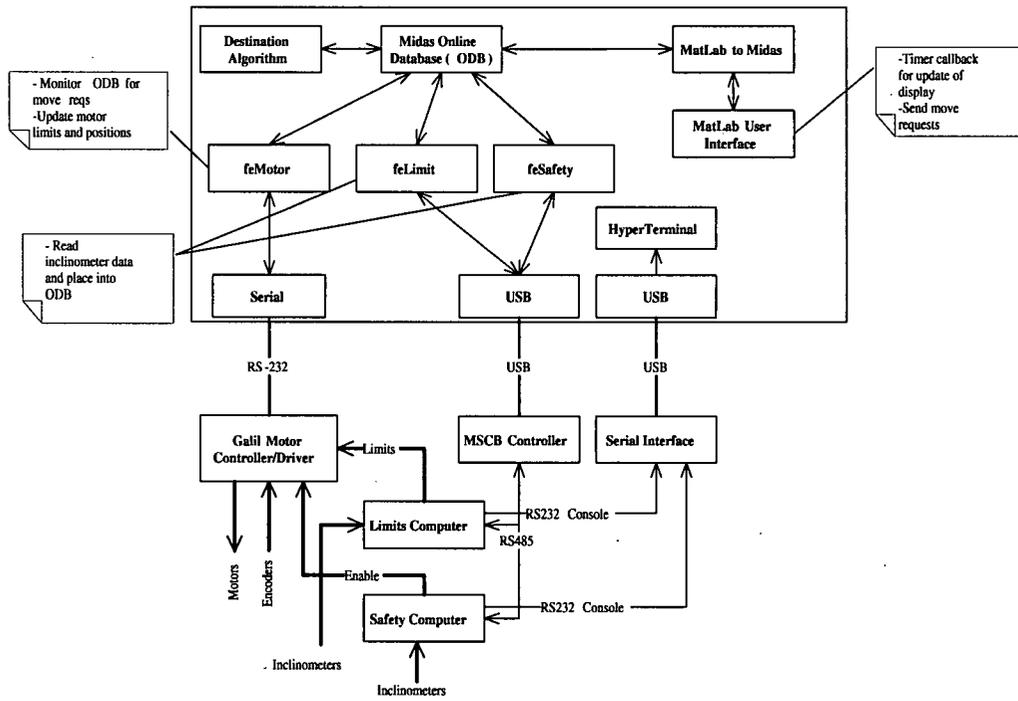
Figure 3.4: Schematic of the Manipulator Control System [4]

have an index mark recorded in the database, thus they provide an absolute measurement with 2,500 counts per turn per disk or 10,000 steps for 360°. The index mark is measured during the calibration and was to be used to set the angle on the motor encoders after the setup at KEK. However the record of the index mark was lost during the travel to Japan. To use the encoders we set the encoder angle using the limit inclinometer readout.

Ten accelerometers are used as inclinometers in two positioning systems described in the next section, independent of the motors. Pairs of inclinometers are placed on electronics chips that are attached to the manipulator. Three pairs read out the angles of the A, B and C arms. Two boards are placed on the vertical section to determine its orientation. One of these boards reads the angle in the plane of swing of the arms, the other records the angle perpendicular to it.

3.3.1 Limit and Safety Systems

The inclinometers are MEMSIC MXS2020EL accelerometers. They provide an absolute orientation with respect to the direction of gravity. The inclinometers are read out by 8051-based microprocessors that compute the position of the arm. If at any point the arm leaves a set of boundary conditions set in the ODB the limit computer will send a stop signal to the motor controller. The boundaries for the safety system are less stringent than those for the limit system, however if the safety system triggers on a boundary violation it shuts down power to the motors.

The accelerometers use an electric heat source and four thermocouples arranged in a plane around the heat source inside an air cavity. Under no acceleration the temperature of the air in the cavity decreases radially outward from the heat source and all the thermocouples read the same. If accelerated the heat gradient in the air cavity changes, and thus do the readings of the different thermocouples. The thermocouples modulate the peak width of a 100 Hz square wave. The width of the pulse on the square wave encodes the acceleration between two thermocouples. We have such a set of thermocouples monitoring the heat source along two perpendicular axis (x and y). First we need to determine the acceleration in each direction from the square wave:

$$a_x = \frac{A_x}{P}$$
$$a_y = \frac{A_y}{P}$$

(3.1)

Here a_x and a_y are the acceleration in the x and y direction measured in relative units. A_x and A_y are the widths of the two output square wave peaks, and P is the period of the square wave (all measured in μs). Thus a vertical inclinometer can measure its absolute orientation by measuring the x and y component of the gravitational acceleration it feels.

The inclinometer readout is a function of the ambient temperature. This can be corrected with a calibration [27]. Since the temperature for running in the 1KT is very stable the temperature calibration is not necessary. The calibration is done using Equation 3.2:

$$a_x^c = \frac{A_x}{P} - \frac{A_x^\circ}{P^\circ} - T_x^c \cdot \Delta T$$
$$a_y^c = \frac{A_y}{P} - \frac{A_y^\circ}{P^\circ} - T_y^c \cdot \Delta T \tag{3.2}$$

Here A_i° and P° are an offset intrinsic to each inclinometer and the period at 25°C. The second term accounts for slight differences in inclinometer chips. T_i^c are correction constants that must be measured for each inclinometer and ΔT is represents a temperature difference that manifests itself as a change in the pulse period. ΔT is given by Equation 3.3:

$$\Delta T = 0.13 \cdot (P - P^\circ) \tag{3.3}$$

The details of this procedure and the code for the inclinometer readout are available from MEMSIC [27]. Finally the angle of the inclinometer makes with respect to gravity is given by Equation 3.4:

$$\theta = \arctan \frac{a_y^c}{a_x^c} \tag{3.4}$$

To get a measurement of the arm position then we mount an inclinometer on the A, B, and C arms in the plane of swing of the arm. Figure 3.5 shows the MEMSIC accelerometers mounted on the arm. Equation 3.4 only works if the inclinometer x and y axes are perpendicular and parallel to the arms central axis and in the plane of the arms swing respectively. To do this the mounts for the inclinometers are designed to be parallel to the central axis of the arm and parallel to the plane of swing for the arm. Section 3.5 explains how to correct for any error in the inclinometer chip alignment.

The boards are waterproofed using polyurethane coating. You can see four sets of wires leading the A_x and A_y signals from the two chips to the limit and safety computers. The resolution of the inclinometers is less than one milli-gravity, which works out to be 0.09° in arm inclination [4].

The angle of the turntable for the Limit and Safety systems is read out by a double potentiometer.
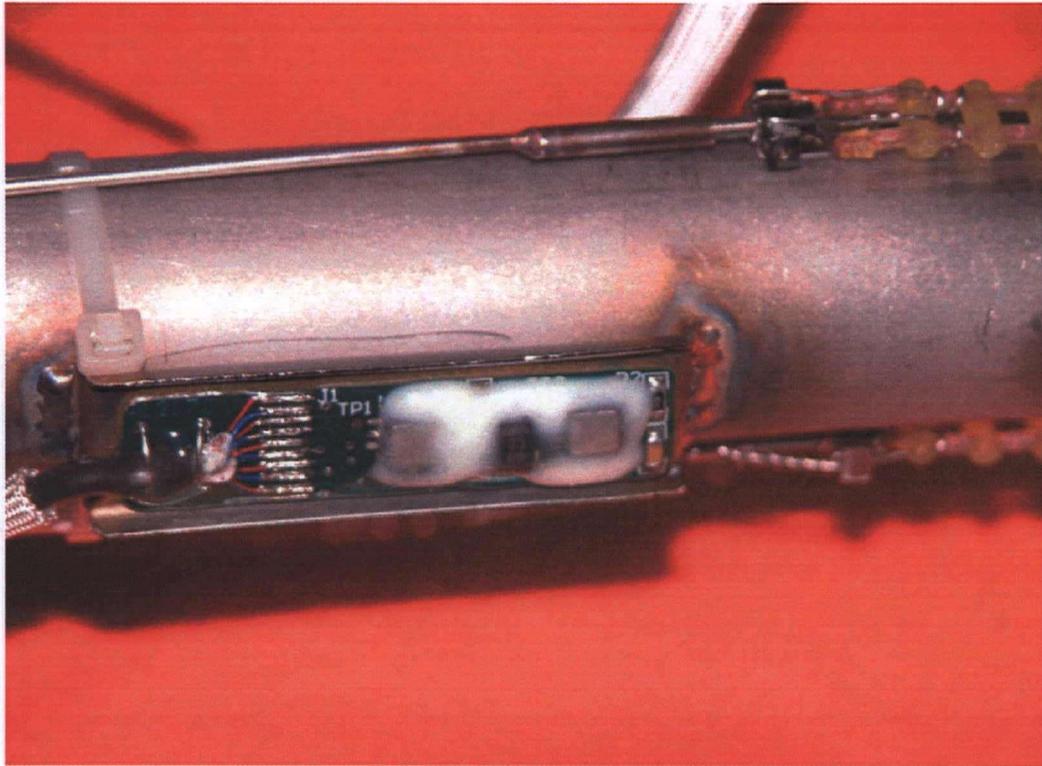
Figure 3.5: The inclinometer board holding the Limit and Safety inclinometers for the B-Arm. The board is mounted on a holder welded to the arm. The board is coated with polyurethane to make it water resistant. Some extra epoxy coating was added for additional safety.

3.3.2 The Manipulator Coordinate Systems

We use three coordinate systems to keep track of the manipulator in the 1KT tank. First we use a two-dimensional coordinate system in the plane of swing of the A, B, and C arm. The line in this plane parallel to the 1KT Axis is the vertical height axis. The origin of this axis is at the height of the bottom of the vertical section. The horizontal in the arm plane is measured from the projection of the 1KT axis onto the plane containing the manipulator arms. The height in this coordinate system is the z coordinate in the tank coordinate system. Figure 3.6 and 3.7 show the top and side view of this coordinate system in the 1KT. To transform the ball position (ie. the tip of the C-Arm) into a point in the primed coordinate system (x', y') we use Equation 3.5.

$$\begin{pmatrix} x' \\ y' \end{pmatrix} = \begin{pmatrix} R_{off} \\ 0 \end{pmatrix} + r \cdot \begin{pmatrix} \cos\phi \\ \sin\phi \end{pmatrix} \tag{3.5}$$

This primed coordinate system is a calculation tool to ease the transformation from (r, h, θ) coordinate to tank coordinates. Finally we transform into the Manipulator Coordinate system displayed in Figure 3.8. The h axis for the manipulator and z axis of the detector coordinates are the same, and the x and y axis of the manipulator coordinate system are in equal but opposite direction as those in the detector coordinate system.

$$\begin{pmatrix} x \\ y \\ z \end{pmatrix} = \begin{pmatrix} -x_{manip} \\ -y_{manip} \\ z_{manip} \end{pmatrix}$$

3.3.3 Manipulator Position

The following algorithm to calculate the position of the joints of the manipulator arms is used by both the encoder and the inclinometer systems.

The computers find the angles θ_i from the encoder or inclinometer output and use the lengths (L_i) of the manipulator sections (VS and Arms A, B and C) supplied by the ODB to calculate the arm position using equations 3.6:

$$\begin{aligned} r_j &= r_o + \sum_{i=1}^{j} (L_i \cos\theta_i) \\ h_j &= h_o + \sum_{i=1}^{j} (L_i \sin\theta_i) \end{aligned} \tag{3.6}$$

Here r_o is distance of the vertical section from the center of the 1KT along the line in which the moving arms of the manipulator are pointing (see Figure 3.7
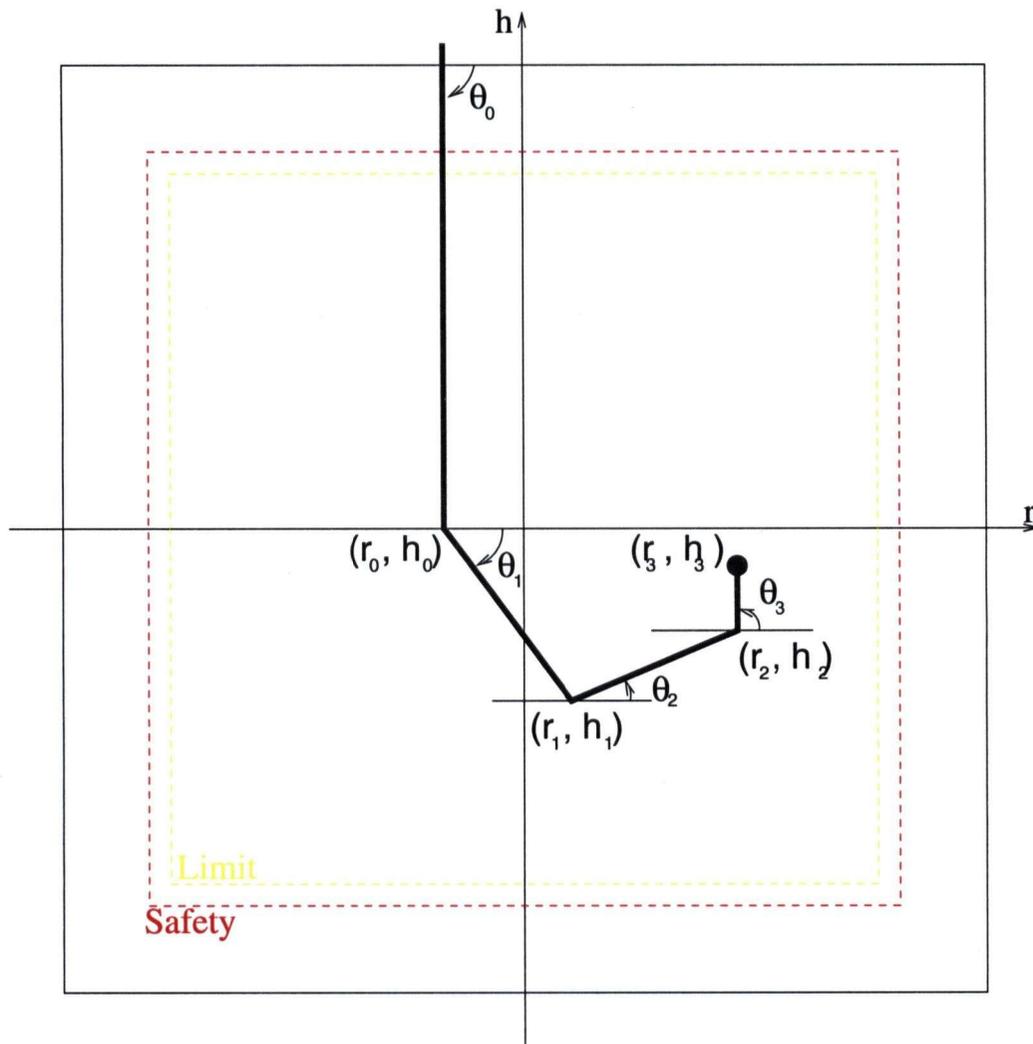
Figure 3.6: Side view of manipulator coordinate system. The origin is defined by the finding the projection of the 1KT axis onto the manipulator's plane of swing, and finding the height on the projected axis at the same hight as $z = 0$ m in the1KT. The positive r direction defines $\theta_i = 0$.
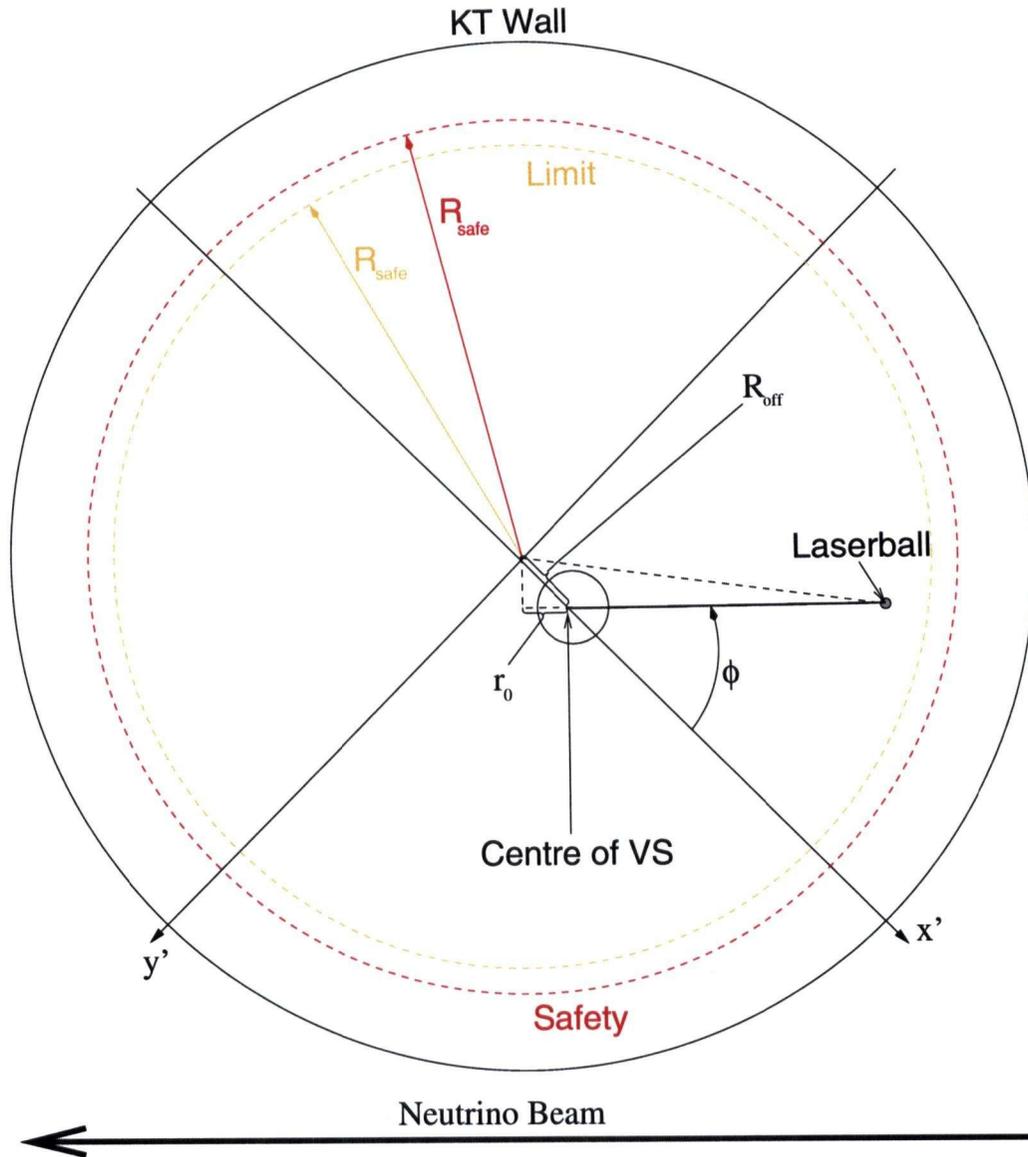
Figure 3.7: Top view of the manipulator coordinate system. The primed coordinate system is a temporary x and y axis used only to ease the calculations. $R_{off} = 1.03$ m is the distance between the center of the 1KT and the insertion hole. The coordinates of the insertion hole in the tank coordinate system are $x = 0.75$ m and $y = 0.705$ cm.
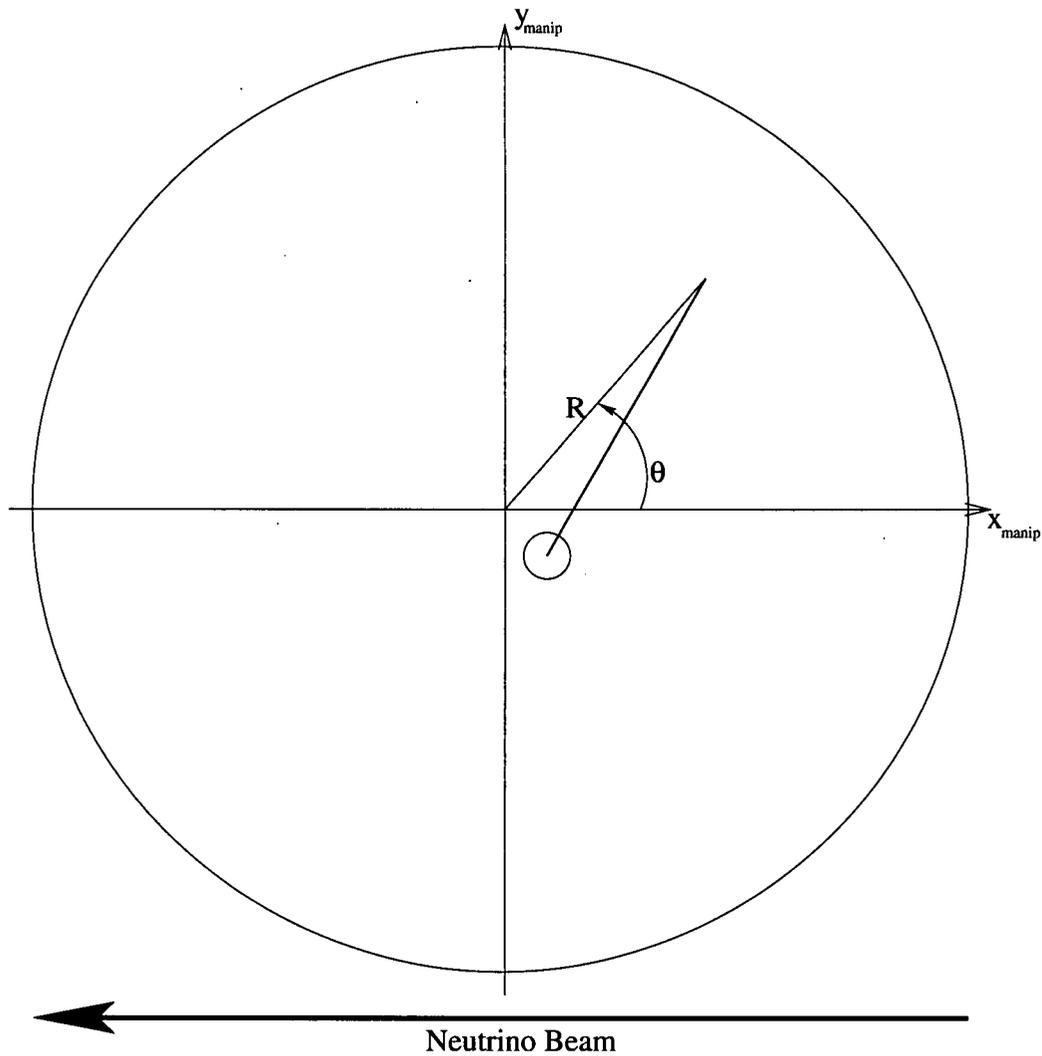
Figure 3.8: Top view of the Manipulator coordinate system. The z-axis is the same as the z-axis in tank coordinates (out of the page in this figure). Here θ is the azimuthal angle in the manipulator coordinate system used for in the GUI which is described in Section 3.3.4

Table 3.2: Boundaries for the Manipulator Limit And Safety Systems [4]

Rule	Boundary	Limit	Safety
Roof	B or C tip Approaching Top	$|h| < 3.3$ m	$|h| < 3.5$ m
Floor	B or C tip Approaching Bottom	$|h| < 3.3$ m	$|h| < 3.5$ m
Center	B or C tip Approaching VS	0.20 m	0.18 m
Radial	B or C tip Approaching Wall	$|r| < 3.3$ m	$|r| < 3.4$ m
VA	Minimum Angle Between VS and A	40°	38°
AB	Minimum Angle between A and B arms	15°	12°
BC	Minimum Angle between B and C arm	15°	12°
Turntable	Over-rotation of the Turntable	5°	10°

for clarification) and h_o is the height of the bottom of the vertical column along the central axis of the 1KT (the same as the z-coordinate in the tank coordinate system). r_o depends on the orientation of the manipulator as described in Equation 3.7. r_j and h_j are the radial distance from the central axis and height along the central axis of the 1KT of the tip of the jth arm respectively (Figure 3.6 gives an illustration):

$$r_o = R_{off} \cos \phi \qquad (3.7)$$

As shown by Figure 3.7 R_{off} is the distance from the axis of the 1KT to the insertion hole. ϕ is the angle between the manipulator arms and the line from the top center of the 1KT through the insertion hole. The manipulator is designed to make $h_o = 0$ cm, and this is what the encoder system uses. The inclinometer systems use the angle read out by the VS inclinometer in the plane of swing of the manipulator arms to determine r_o and h_o as described in Equation 3.8:

$$\begin{aligned} r_o &= L_o \cos \theta_o \\ h_o &= L_o \left(1 - \sin \theta_o\right) \end{aligned} \qquad (3.8)$$

Here θ_o is the angle of the vertical section in the plane of the arms (ideally $\theta_o = 0°$). The coordinate systems used to locate the manipulator are explained further Section 3.3.2. After this computation the limit computers check whether any of the manipulator's parts violate the boundary conditions summarized in Table 3.2. Determining the wall limit is nontrivial since the manipulator is offset from the center of the 1KT tank. The allowed radii in the coordinates calculated by the limit and safety computers are given by

Equation 3.9.

$$r_{safe} = R_{off}\cos(\pi - \phi) \pm \sqrt{R_{safe}^2 - R_{off}^2\sin^2(\pi - \phi)} \qquad (3.9)$$

Figure 3.7 explains the meaning of the values needed in for this calculation. These were measured on site due to lack of structural drawings and then entered into the ODB.

3.3.4 The Manipulator GUI

The main tool used to control the manipulator is the Matlab GUI created to communicate with the ODB. Figure 3.9 shows how this GUI displays the current position of the manipulator according to all three positioning systems. The graph in the left shows the height-radius coordinate system of the arm position in the plane of swing of the arms. On the right you can see the position of the laserball from the top (the view is similar to the one outlined in Figure 3.7). The display is color-coded to show the position according to the inclinometer or encoder systems. The bottom left shows the angles read out from the four position systems. The GUI will also indicate if a limit is triggered and which further motion is prohibited. In the low center you can read the position of the ball in the manipulator coordinate system. Another display shows the current status of the front end programs running on the control computer. In the bottom right you may enter the desired position of the manipulator. The control code computed the arm positions necessary to reach the given coordinate with the ball given the desired concavity. The movement of the A, B and C arms is divided into a number of continuous steps. Before the arm moves, each of the positions the ball should arrive at is checked for limit violations. If any are found the move is not allowed and the position has to be reached using the manual control GUI.

Sometimes it may be advantageous to order one arm of the manipulator to move to a specific angle (especially for the turntable). To do this the manual control GUI was developed. The manual menu in the main GUI opens the window displayed in Figure 3.10. The primary and secondary fields show the reading from the motor and auxiliary encoders. The Destination field lets you enter a target angle for the motors. The last stop indicates why that particular arm stopped moving last. If the arm hit a limit the checked boxes will indicate which way the arm may not move.
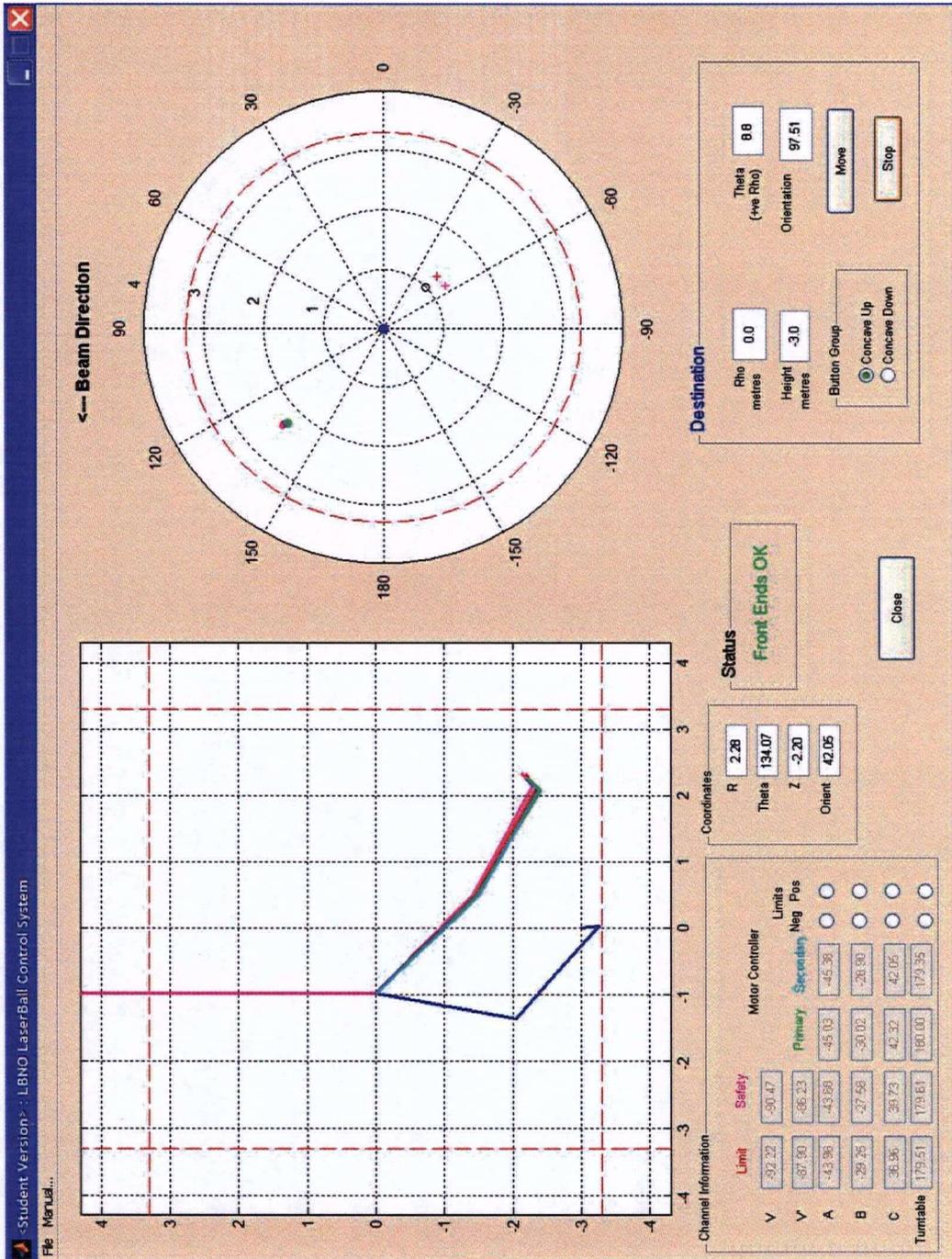
Figure 3.9: Screen-shot of the Main Graphical User Interface for the manipulator arm.
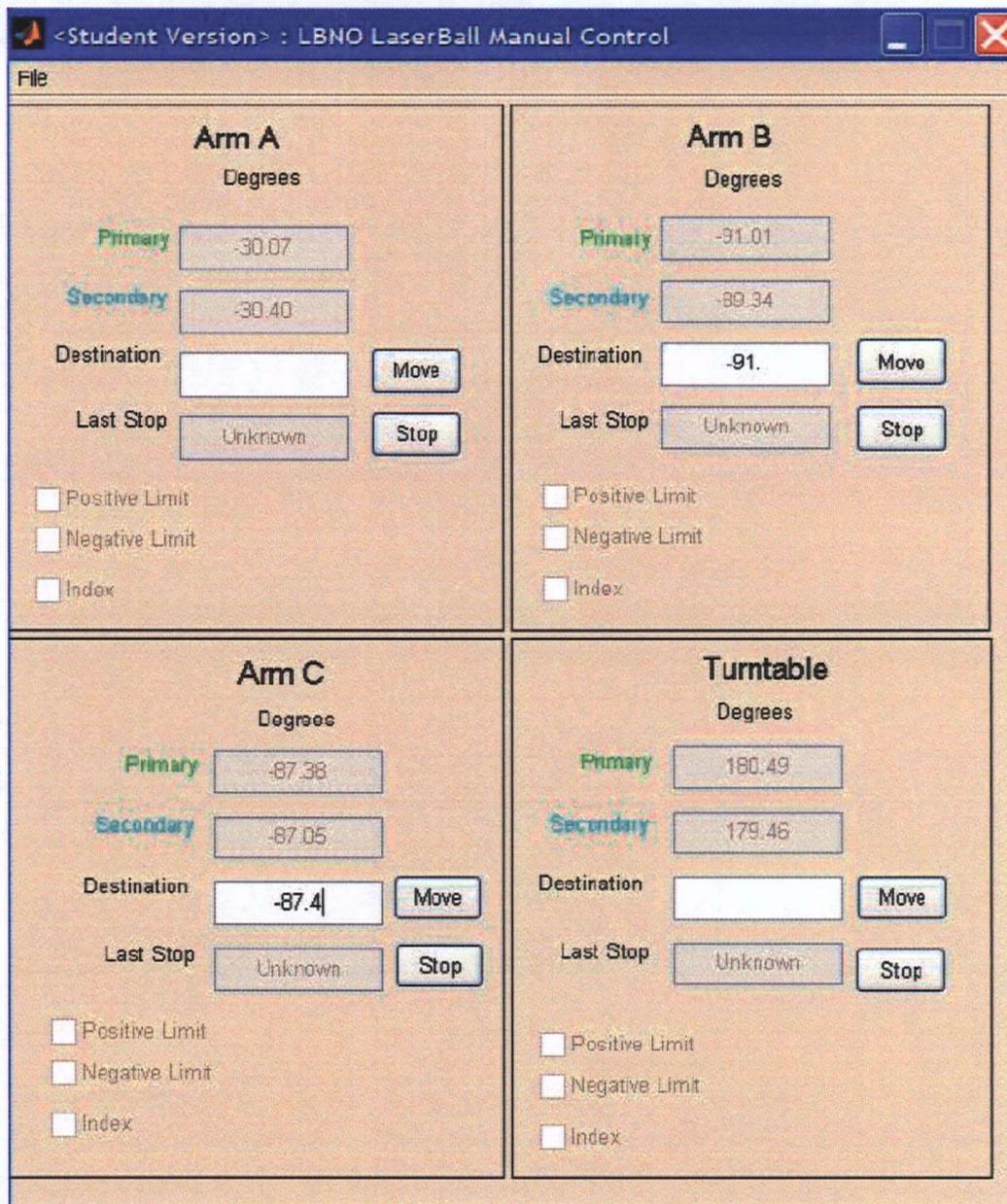
Figure 3.10: The Manual Control GUI for the Manipulator. This GUI allows the user to move one arm to a specific angle.

3.4 Construction and Assembly

The design drawings for the manipulator were done professionally by Mark Lenckowski of the University of Victoria design workshop and Corrie Holmberg from the TRIUMF design workshop. The parts of the arm were machined at the machine shops at TRIUMF, the University of British Columbia Physics department, and the University of Victoria. Most of the machining required very precise work and was done by professionals, while a few parts requiring less accuracy were machined by me. All the parts from the different machine shops were assembled at TRIUMF by Rich Helmer, Keith Hoyle and myself for calibration. Some problems, such as the stability of the tripod supporting the turntable, were recognized and fixed during the test assembly at TRIUMF. The final assembly was carried out by the entire K2K Canada group, with help from Keith Hoyle, Mark Lenkowski and David Morris.

3.5 Calibration

Before the manipulator was deployed in the 1KT it was tested and calibrated at TRIUMF. The robot arm was suspended from the roof of the proton hall. Figure 3.11 shows the imitation of the 1KT access that was set up at TRIUMF on the roof of the proton hall. Figure 3.12 shows the manipulator setup in the proton hall at TRIUMF. Since the manipulator is not in water the A and B arms are not neutrally buoyant. So to allow the A and B arms full range of motion, pipe counterweights were used. The counterweight on the A-arm did not properly balance and it was only possible to move the A-arm though small angles at a time for the calibration of the manipulator. The angle between the vertical section and the turntable was tested to be perpendicular with a carpenters edge around its circumference of the vertical section. Aluminum spacers were placed between the vertical section mounts and the turntable until the angle between the turntable and the vertical section was perpendicular. Using the carpenters level this measurement is probably accurate to 0.4°. Next the turntable supporting the manipulator was adjusted until a machinist's level set on the turntable supporting the vertical section read level.

Figure 3.11: Mockup of the 1KT access at TRIUMF. The support structure for the manipulator is set up on imitations of the roof support beam and the CRP cage. The weight of the Manipulator is on the joint at the top of the tripod. The tripod holds the turntable and manipulator in place.

Figure 3.12: View of the manipulator suspended from the ceiling of the proton hall at TRIUMF

3.5.1 Wobble

Due to the length of the vertical section and the fact that it is composed of three sections the bottom of the vertical section moves in a small circle as the turntable rotates. This motion is reproducible, thus we measured the rotation of the bottom of the vertical section. This was accomplished by mounting two plumb bobs on opposing sides at the bottom of the vertical section and recording their positions throughout one rotation. The center point between the two plumb bob locations was taken to be the center of the manipulator. A reading from the auxiliary encoder for the turntable was taken with each position, however we needed to change the index position when we set the manipulator up at KEK. This means that we need to rotate the position of the circle. Figure 3.13 shows the result from these measurements.

The wobble of the bottom of the main section is caused by two problems with the manipulator set up. First the vertical section of the manipulator may not be perpendicular to the turntable. This would cause the bottom of the vertical section to describe a circle centered on the center of the turntable. The second problem is that the turntable may not be perfectly level. This means that the center of the bottom of the vertical section may not coincide with the center of the turntable, thus causing the vertical section to wobble about a point not below the center of the turnable.

3.5.2 Total Station

The A and B arms were taken though their entire range of motion while monitored with a Leica 5005 Total Station. The total station uses two small targets that were attached to the A and B arms and measures the positions of these targets relative to the total station by lining up its sights with marks on the targets. Using the position information of the two targets on each arm the orientation of the arms in space can be measured with an accuracy of 0.33 arc-seconds. The readout of all the manipulator position systems was taken as each arm was rotated through 360°. It was expected that the inclinometer chips were not perfectly aligned with the plane of motion of the arms. This would result in a sinusoidally varying offset of the inclinometer angle from the real angle. Figure 3.14 shows the result for the A-arm correction and Figure 3.15 shows the result for the B-arm correction. The best approximation to the real offset was taken sine fit for the A-arm and a to be a linear interpolation between data points for the B-arm.
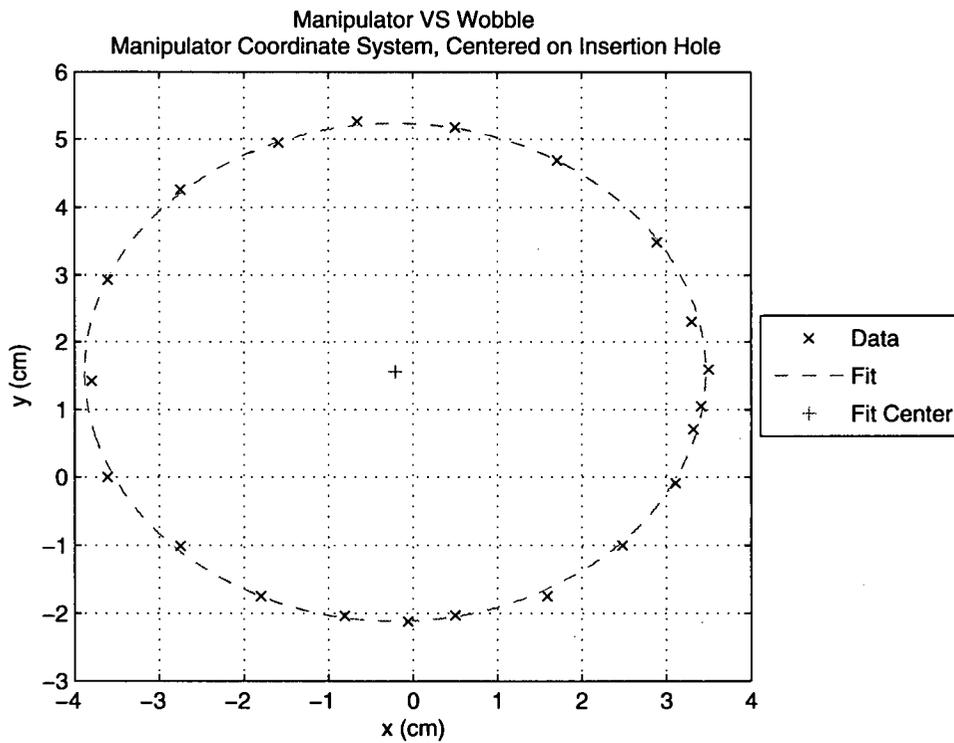
Figure 3.13: The circle traced out by the bottom of the vertical section of the manipulator in the manipulator coordinate system. The origin of this plot lies below the turntable center.
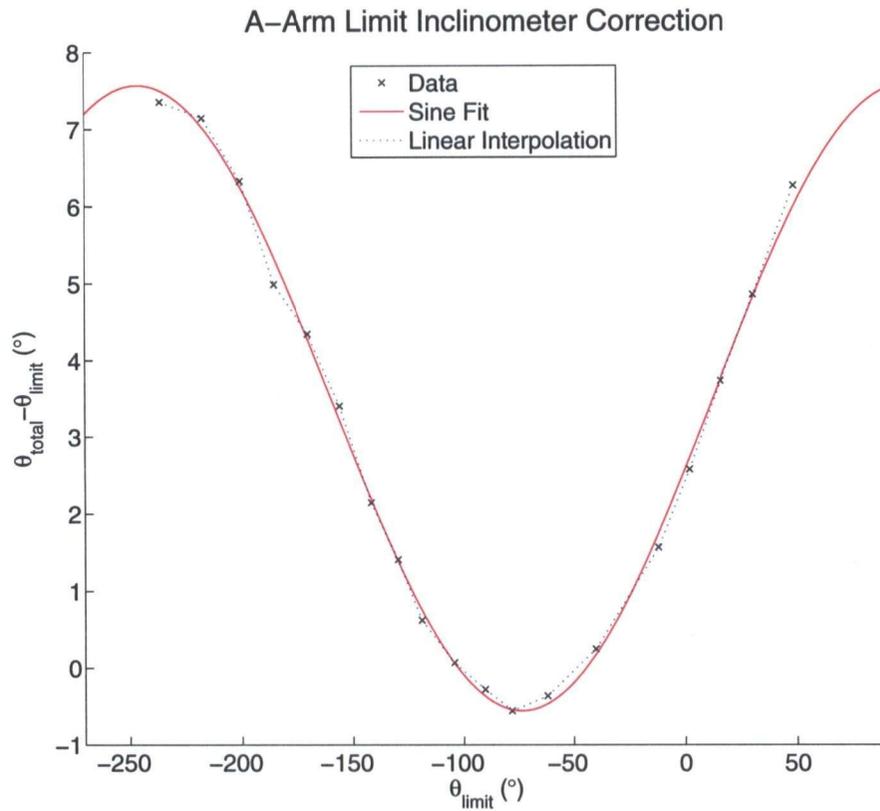
Figure 3.14: The correction for the limit inclinometer on the A-arm.
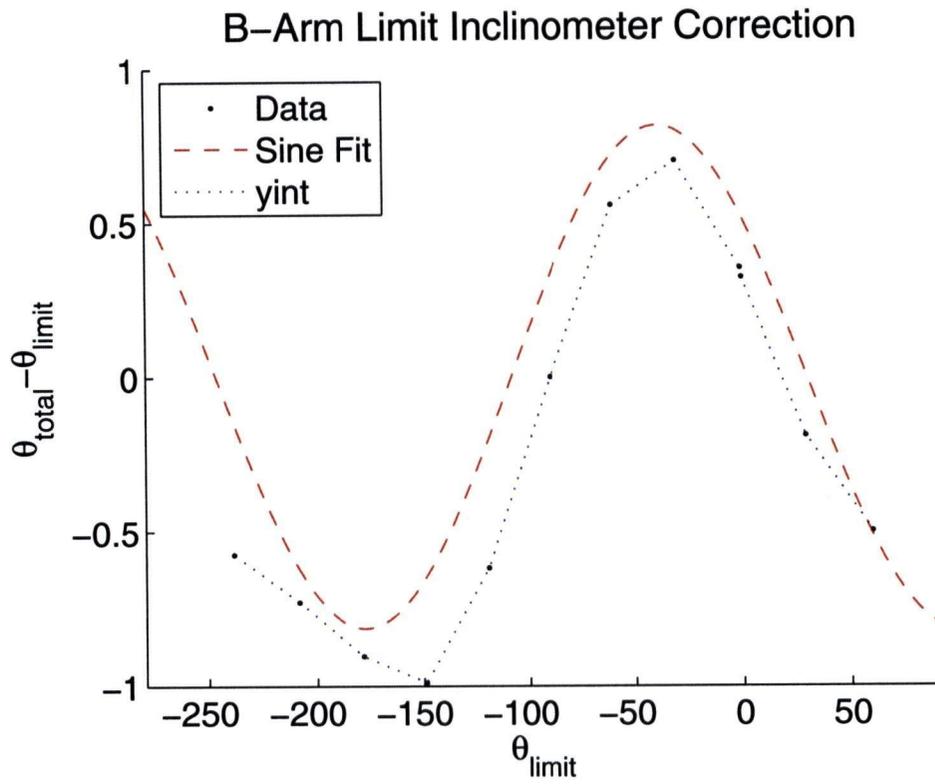
Figure 3.15: The correction for the B-arm limit inclinometer.

3.6 Manipulator Setup At The 1KT

After testing at TRIUMF the manipulator was taken apart and shipped to Japan. It arrived on April 21, 2005. The first data was taken April 30, 2005 and the 1KT was collecting calibration data only interrupted by a few problems with the 1KT DAQ until it was taken down on June 14, 2006. The manipulator was taken apart and shipped back to Canada two weeks later.

The manipulator was assembled inside the free room above the 1KT since it could not fit inside the front door of the 1KT fully assembled. We could fit the moving sections and the first vertical section into the 1KT at the same time as long as the chains were not hindering the full range of motion of the arms. So once this first part of the manipulator was inside the 1KT the chain drives and the black plastic coat were installed. Since the entire manipulator is too large to fit into the room above the detector volume and too large to easily fit through the CRP we need to lower the manipulator section by section starting with the B and C arm and moving on toward the vertical sections. Once the A, B and C arms were in the detector volume there was enough room to fit the last two parts of the vertical section. The joints and chain drive along the vertical section were assembled in the tank. Finally the vertical section was lowered in the 1KT piece by piece. When the second and third parts of the VS were lowered into the 1KT the brackets fastening the VS parts together in a solid section needed to be tightened before the section was lowered into the detector. Figures 3.16 to 3.18 display this step-by-step procedure showing the insertion of the second part of the vertical section.

After the manipulator on its turntable was put into the 1KT the support structure was finished and its position aligned to match the calibration setup at TRIUMF. The machinist's level we used to ensure that the turntable was horizontal turned out to be broken when we used it at KEK, which made it impossible to exactly recreate the setup at TRIUMF. Thus another level was used and we recorded the setup at KEK which we later reproduced to perform a back calibration of the manipulator at TRIUMF.

Another problem we encountered was that we lost the booklet which had the recorded index marks on the auxiliary encoders used at TRIUMF to set the motor encoder angles. Since the 0° reading of the limit inclinometers was known to be good, we set the motor and auxiliary encoders using the limit inclinometer reading. Because of this we use the limit inclinometer to give us the nominal position of the laserball for the manipulator analysis. With the corrections from the total station the inclinometer readings are precise

Figure 3.16: Example of the step-by-step insertion procedure used to fit the manipulator into the 1KT. Here the second part of the vertical section is lifted off the makeshift assembly table, before it can be lowered into the detector.
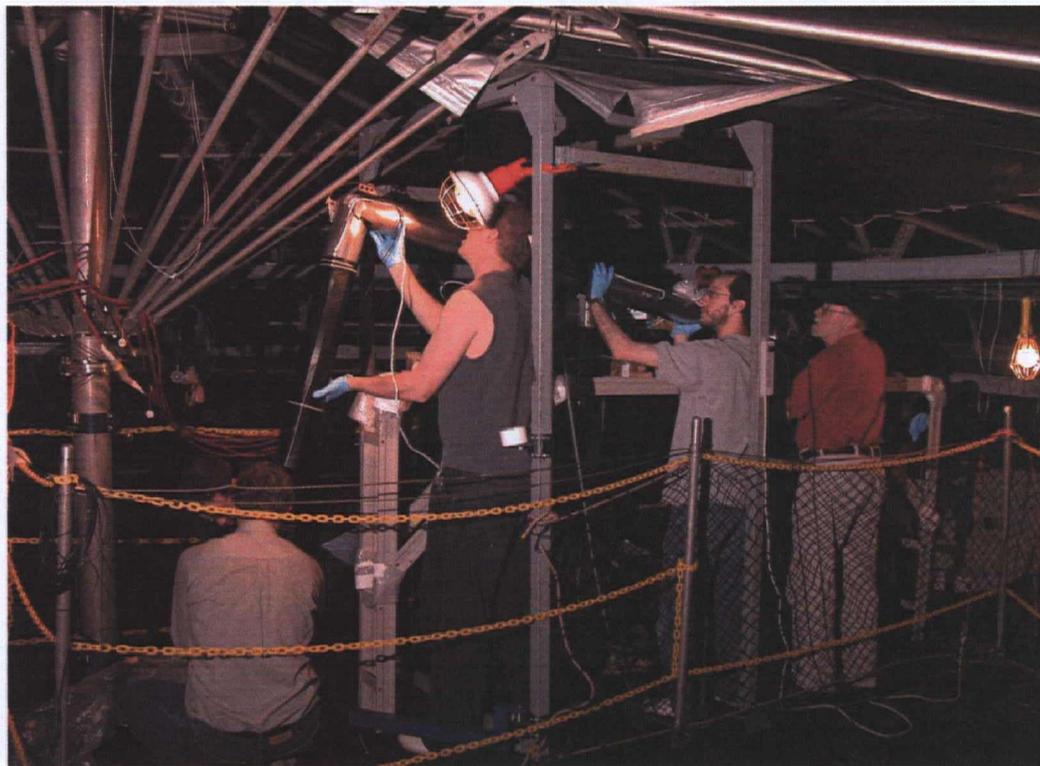
Figure 3.17: The stage of the manipulator insertion that is most critical, fitting the VS pieces into the CRP under the roof support.

Figure 3.18: Before lowering part 2 of the VS into the 1KT the clamp holding parts one and two straight must be fastened.

Figure 3.19: The manipulator group just after the manipulator assembly and insertion had been completed. From left to right: Mark Lenckowski, Rich Helmer, Scott Oser, Frank Berghaus, Akira Konaka, and David Morris

to 0.3° which translates into an 1cm uncertainty in the ball position, thus matching our design goals.

The manipulator was covered in black tarp to minimize reflection except for the joints attaching the polyurethane chains to the stainless steel sections. Figure 3.6 shows the Canadian group around the manipulator fully assembled and inserted into the 1KT tank.

Chapter 4

Manipulator Data and Analysis

4.1 Data Taken In Japan

Data was collected by the manipulator in order to study:

- Position reconstruction throughout the 1KT,

- Effect of the manipulator shadow on the reconstruction,

- Position reproducibility,

- Fiducial volume error,

- Optical parameters:

  - Attenuation length, and
  - Angular response of the PMTs,

- Detector asymmetry from:

  - Vertical position, and
  - Magnetic fields in 1KT, and

- Effects of laserball orientation.

To achieve all this we took data using the manipulator with these motions:

- Ball rotation and flips to study:

  - Laserball asymmetry, and
  - Shadow effects

- Swings of a single moving arm to study:

  - Manipulator position accuracy, and

- Position reconstruction

- Scans along the different axes in the 1KT to study:

  - Position reconstruction, and
  - PMT Acceptance and optical properties

- Tracing out hexagons at different heights to study:

  - Detector asymmetry, and
  - Position reconstruction

- A Grid through the FV to study:

  - Position reconstruction, and
  - PMT acceptance, and

- Off center TQ-map data.

Appendix B summarizes all the data that was taken with the manipulator.

4.1.1 Reconstruction Bias and Fiducial Volume Study

The error in the fiducial volume is the dominant uncertainty in the 1KT measurement for the far/near ratio. To know the flux measurement of the 1KT we need to be able to correctly identify the volume of the 1KT we are considering for fully contained (FC) events. A FC event has a neutrino interaction vertex in the 1KT and all light detected during the event must be in the inner detector volume.

4.1.2 Up/Down Asymmetry and Energy Scale

Some of the manipulator data is specifically designed to study the up-down asymmetry in the 1KT. A 1.7% horizontal-vertical asymmetry in the energy of muons stopping in the detector can be observed using cosmic rays [28]. The axis scans done with the manipulator may be able to characterize this asymmetry more.

4.1.3 Scattering and Particle Identification

Scattering and reflections inside the 1KT have a strong effect on particle identification (PID) and Ring counting in the 1KT. This effect is particularly strong on multi-ring electron-like events. The data throughout the 1KT taken with the manipulator will aid the understanding of scattering of light in the 1KT tank.

4.2 Reconstruction

In this thesis we will only be studying the effects revealed by the position reconstruction. The basic algorithm for the laserball reconstruction is the same as described in Section 2.2. When making the PMTs timing histograms we started by excluding PMT events on which the ADC saturates, since the time and charge reading on these events are inaccurate.

The presence of the manipulator requires that the shadow it casts on the PMTs must be taken into account. We also need to find PMTs that are hit by light from grazing reflection of the manipulator. Three methods are used to identify shadowed PMTs and exclude them from the fit. We cut PMTs using:

- Geometrical location of the manipulator shadow,

- A timing cut:

$$|t_{pmt} - tof - \overline{t_{pmt}}| \geq 20 \ ns \qquad (4.1)$$

  where t_{pmt} is the time measured by the PMT, tof is the time of flight, and $\overline{t_{pmt}}$ is the average tof-corrected time over all PMTs, and

- An outlier cut: PMTs with 5σ and larger fit residuals.

The timing cut identifies PMTs that have times very far away from the mean time-of-flight corrected time: most likely a bad PMT, or one measuring a lot of reflected/scattered light. Figure 4.1 shows the distribution of PMT times for a run with the laserball on a string. So all PMTs with a time of more then 20ns from the mean can be regarded as broken or seeing a lot of light from reflection off of the manipulator. This cut allows a lot of room for outlying PMTs. These will show up with large fit residuals since their time will be very different from the mean times of surrounding PMTs. These outlying PMTs will get tagged by the outlier cut.
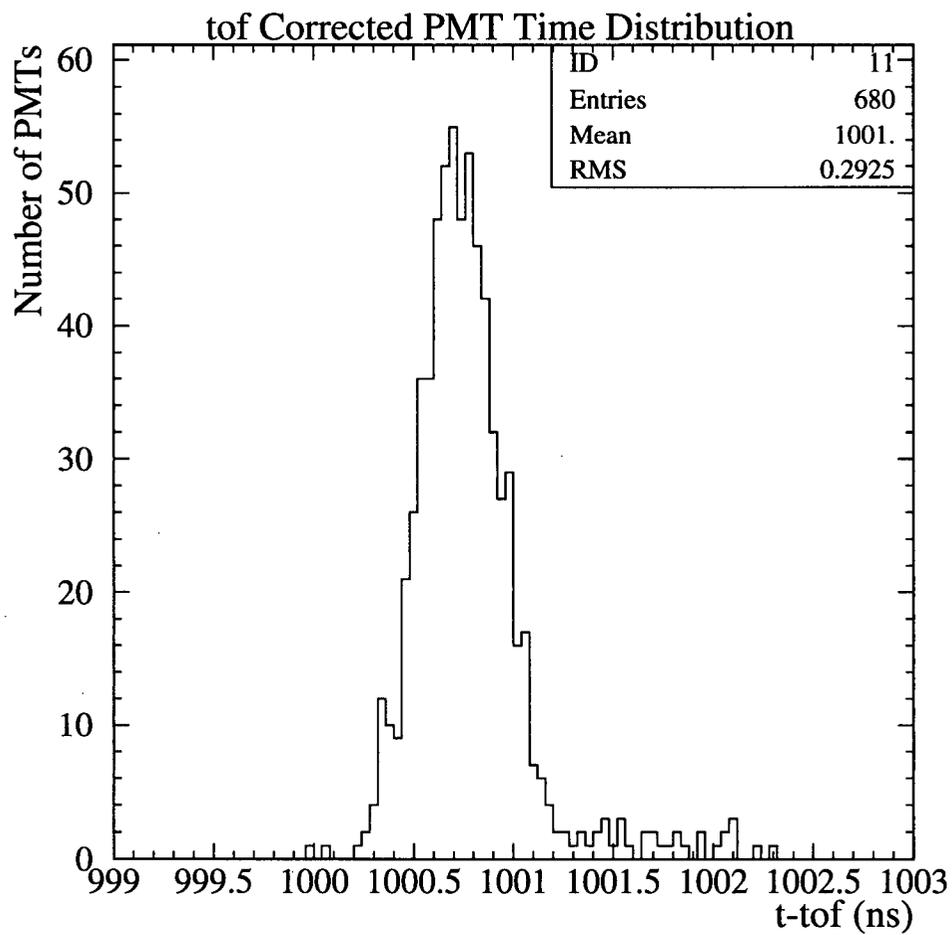
Figure 4.1: Time distribution from a run using the ball on a string. Note that all PMTs gave mean times within a window less than 3 ns wide.

4.2.1 Saturation Cut

Since no documentation on the ADC saturation signal for the 1KT PMTs exists we scanned the two ADC channels of the PMTs for all PMTs in a high occupancy run looking for a cutoff. The ADC saturation spike is clearly visible at the right hand of Figure 4.2. The ADC output channel for a saturated PMT is 1166012416. Considering the PMTs are read out by 12-bit ADCs this value makes little sense, and no clarification has been forthcoming. The meaning of the spike on the plot is clear enough though. Thus any PMT events with a raw ADC output equal to 1166012416 in either channel from the PMT are cut.

4.2.2 Geometrical Shadow Cut

To explain how the location of the shadow of the manipulator is determined first consider any point on the wall, top or bottom of the 1KT. Knowing the ball position we calculate the vector from the laserball to that point on the wall. This gives us the line from the laserball to the point on the wall, let's call it the light ray. Knowing the position of the beginning and end of each arm we can draw a line along the central axis of the arm. Next we determine the point on the light ray and the point on the arm that are the closest to each other. If the distance between those points is less than the radius of the arm being considered we call the point on the 1KT shadowed. Figure 4.3 shows the shadowed region of the 1KT as calculated by this routine for one run. We flag any PMT as shaded if the shadow reaches anywhere within 10 cm of the edge of the PMT. The loose requirement for the shadow is motivated the limitations on the knowledge of the absolute position of the manipulator in the 1KT. This cut is responsible for almost all excluded PMTs.

4.2.3 Timing and Outlier Cut

To identify PMTs with unreasonable times we determine the mean of the time-of-flight corrected PMT times. Then all PMTs are scanned, and PMTs that are 20 ns from the mean are flagged. This removes PMTs that see mostly light reflected off of the manipulator.

To determine any left-over outliers the fit is run once. Any PMT with a fit residual greater than five times the error on the PMT mean time (5σ) is flagged. Almost no PMTs are flagged by this last cut. This cut removes
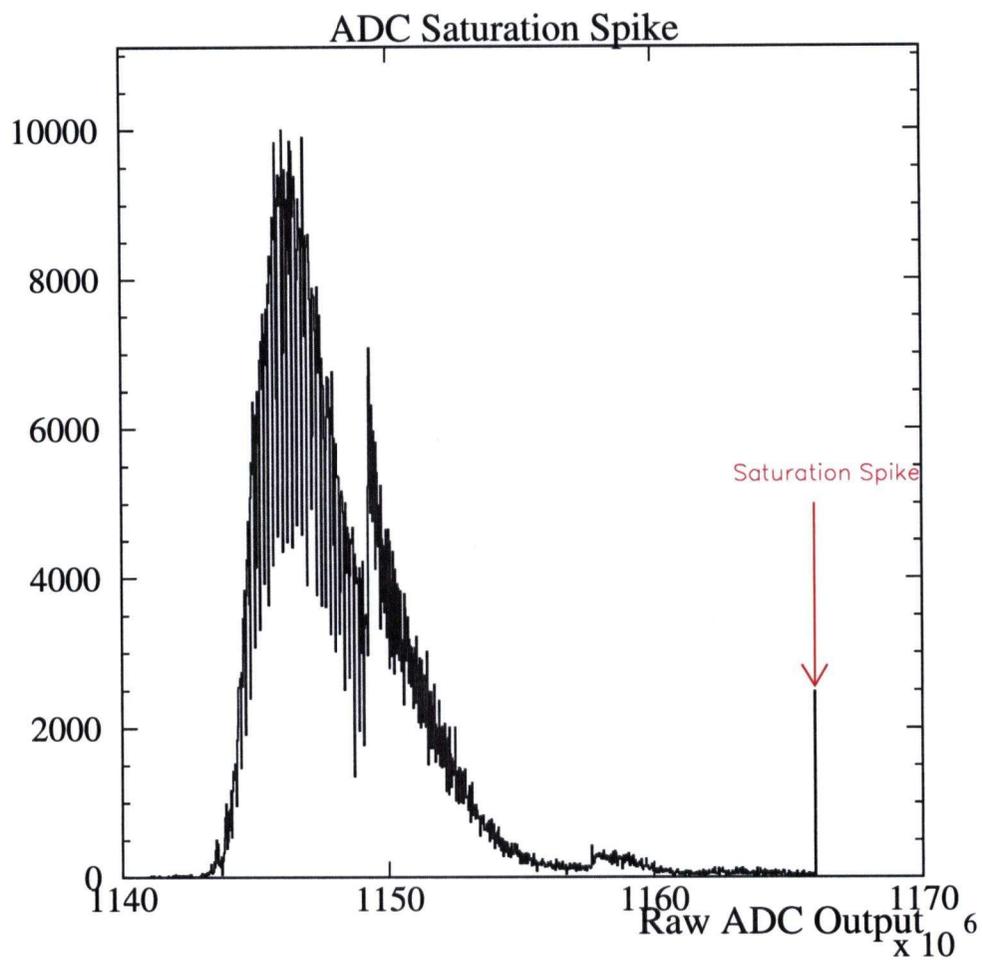
Figure 4.2: The ADC cutoff is clearly visible with the spike at channel 1166012416. The multiple peaks represent the two channels of raw ADC output from the PMT. All ADCs seem to saturate at the same raw ADC output value.
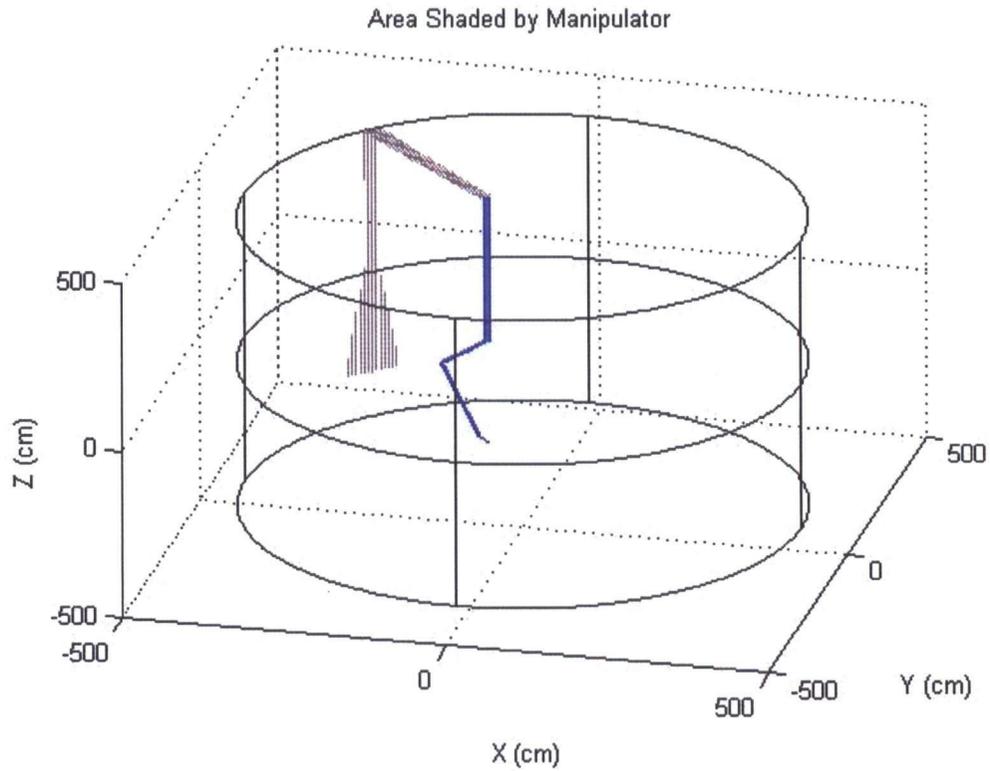
Figure 4.3: Manipulator shadow as determined by geometrical ray tracing. The crooked line in the middle represents the location of the arms.

PMTs that are passed by the PMT timing cut, but have very different times from their neighbors. This would be caused reflection effects of the manipulator.

4.2.4 Nominal Laserball Position

The nominal position of the laserball is determined using the information from the limit inclinometer system. We use the fits displayed in Figures 3.14 and 3.15. These corrected angles are used to determine the nominal position of the laserball using the algorithm outlined in Section 3.3.3. The correction for the vertical section wobble is not properly understood, since it was difficult to properly relate the orientation of the wobble as measured at TRIUMF to the manipulator position in the 1KT detector. Therefore the wobble correction was not applied.

4.2.5 Results of the Reconstruction

Before applying the inclinometer position correction and the cuts for shadow and reflections our reconstructed positions agree with the nominal positions to about 6 cm. Figure 4.4 shows this agreement between uncorrected nominal and fit positions. Figure 4.5 shows that the fitted position agrees with the nominal position better than 3 cm for low occupancy data after accounting for shadows, scattering, inclinometer offsets, and saturation. Figure 4.6 shows that the high occupancy data has a large spread between the nominal and fitted positions even after all the corrections. The offsets in the x, y and z positions are due to our uncertainty in placing the manipulator relative to the 1KT tank. Since no design drawings of the 1KT were available it is expected that the positions are off by a few centimeters. The variance of the difference between fitted and nominal ball positions represents how well we understand the positions of the manipulator relative to each other, thus it is the interesting number to look at. Since the problems with the position reconstruction of the high occupancy runs were not resolved by the saturation cut, the error in the reconstruction of the high occupancy data may be the result of another systematic effect.

Figures 4.7 and 4.8 show the laserball position reconstruction throughout the tank volume without and with all corrections respectively. The most curious feature of Figure 4.8 is the consistent agreement between low and medium occupancy, while the high occupancy data always seems different.
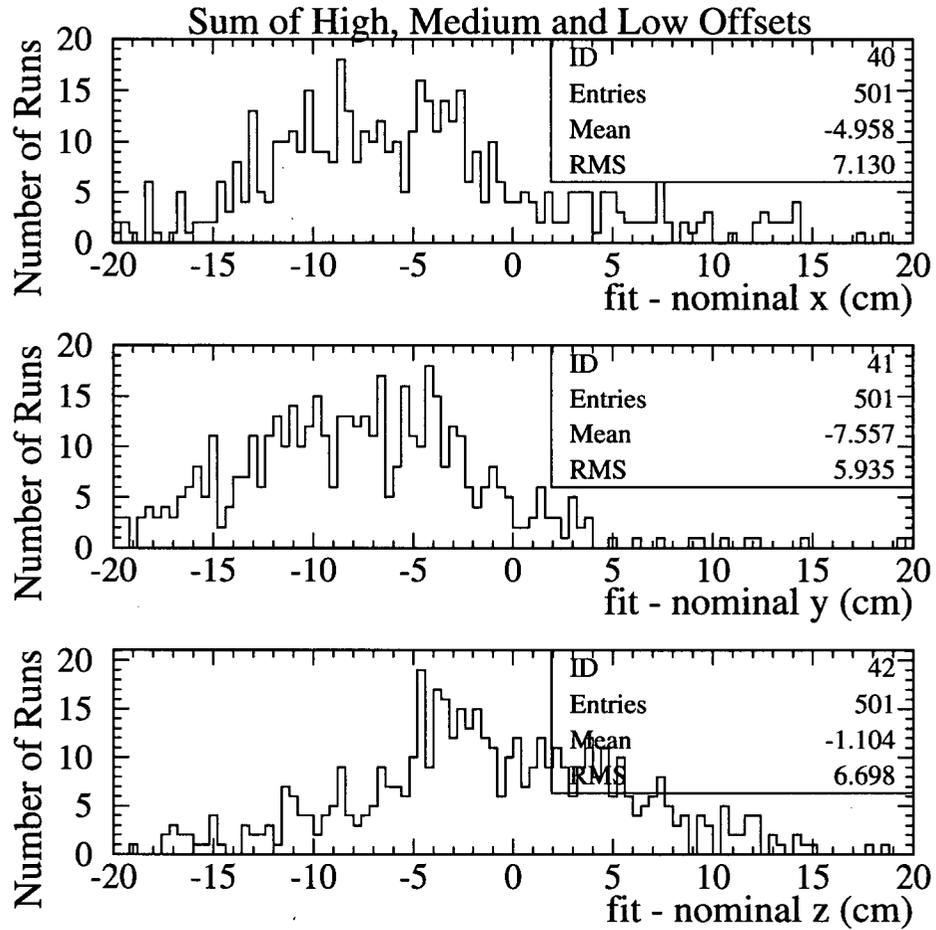
Figure 4.4: Offset between uncorrected nominal and fitted positions for all manipulator runs. Each 'event' in one of these histograms is one run. You can see that nominal and fitted positions do not agree very well without any corrections or cuts.
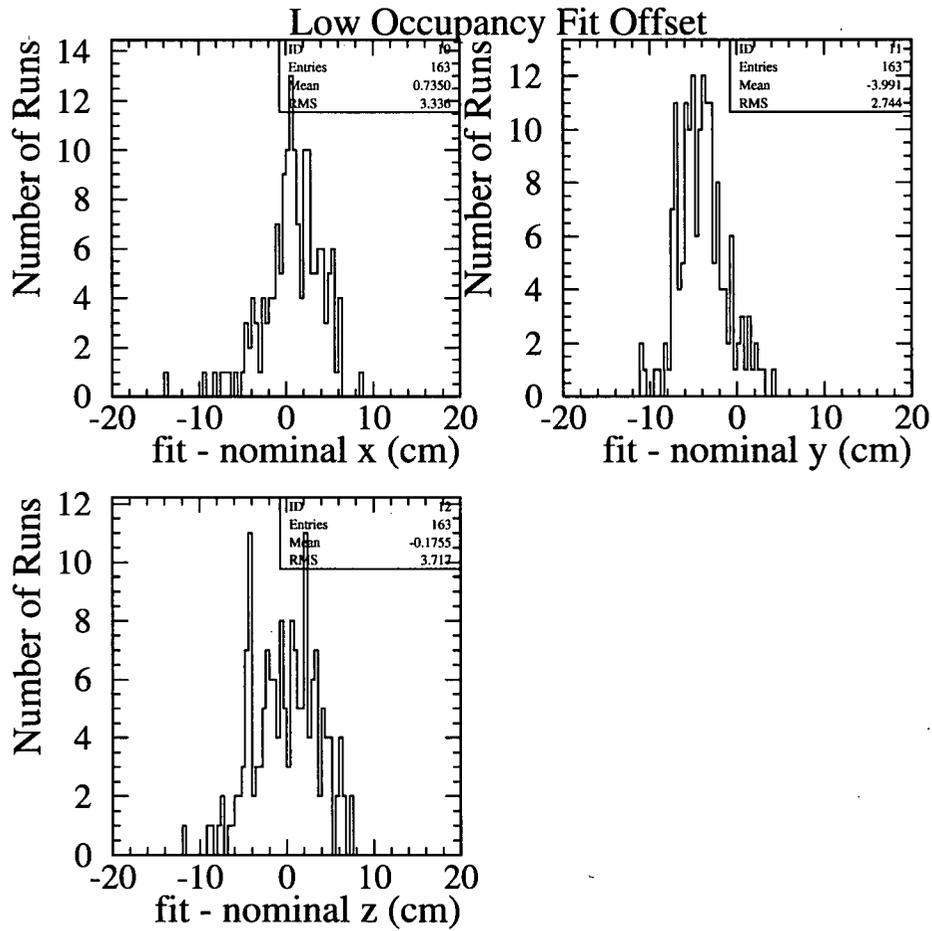
Figure 4.5: Good agreement between nominal and fit positions for the low occupancy data with all cuts and corrections.
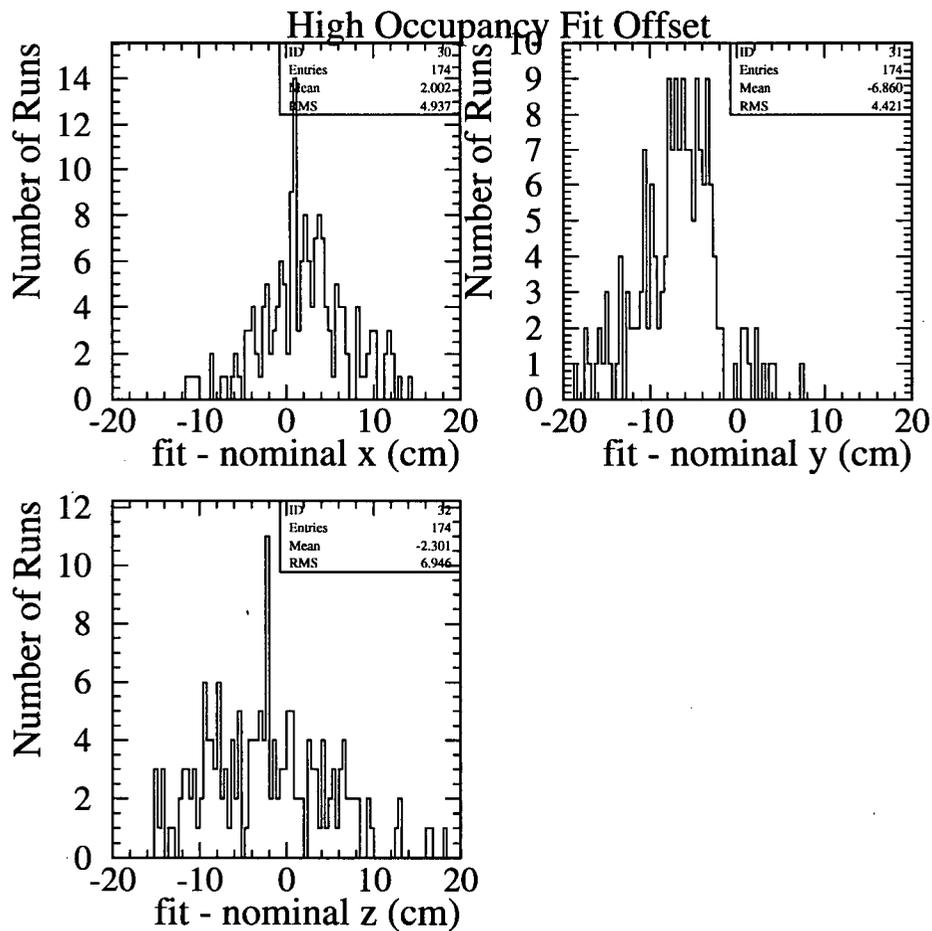
Figure 4.6: The nominal and fit positions for the high occupancy data disagree even after all cuts and corrections are applied.
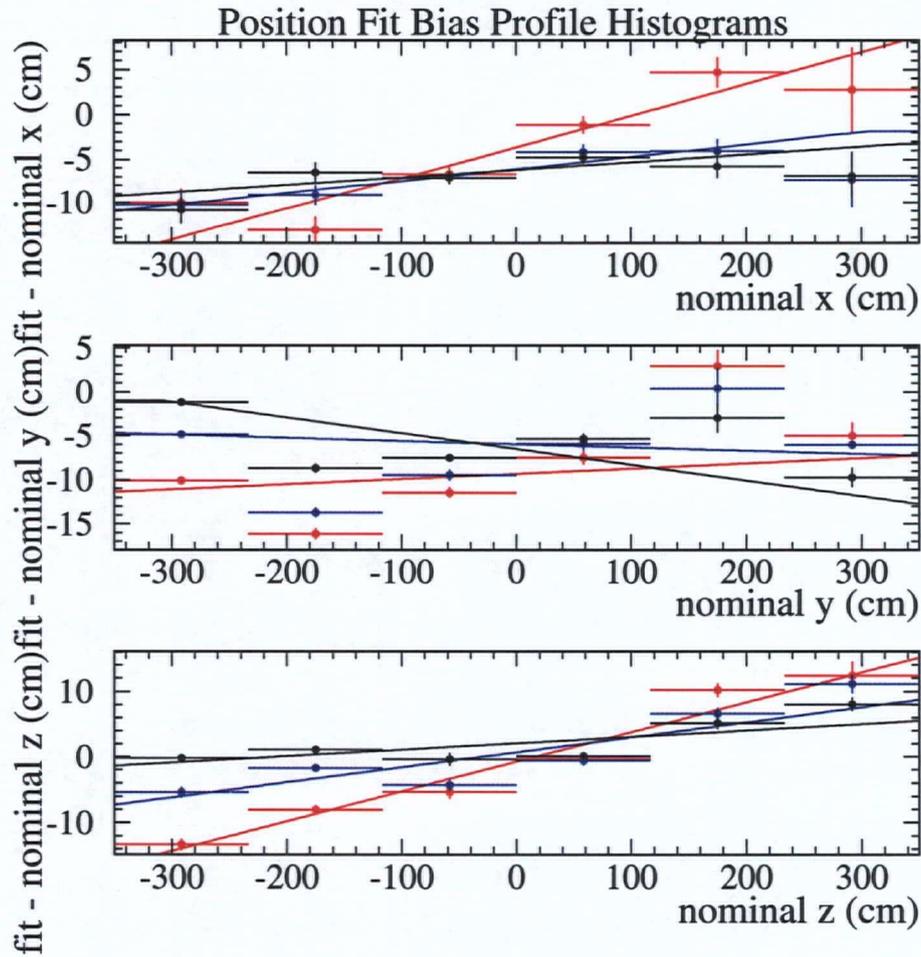
Figure 4.7: Without corrections to the nominal positions and cuts to the data used in the fits the optical reconstruction shows significant deviations throughout the tank. The results along the vertical axis show a very strong slope.
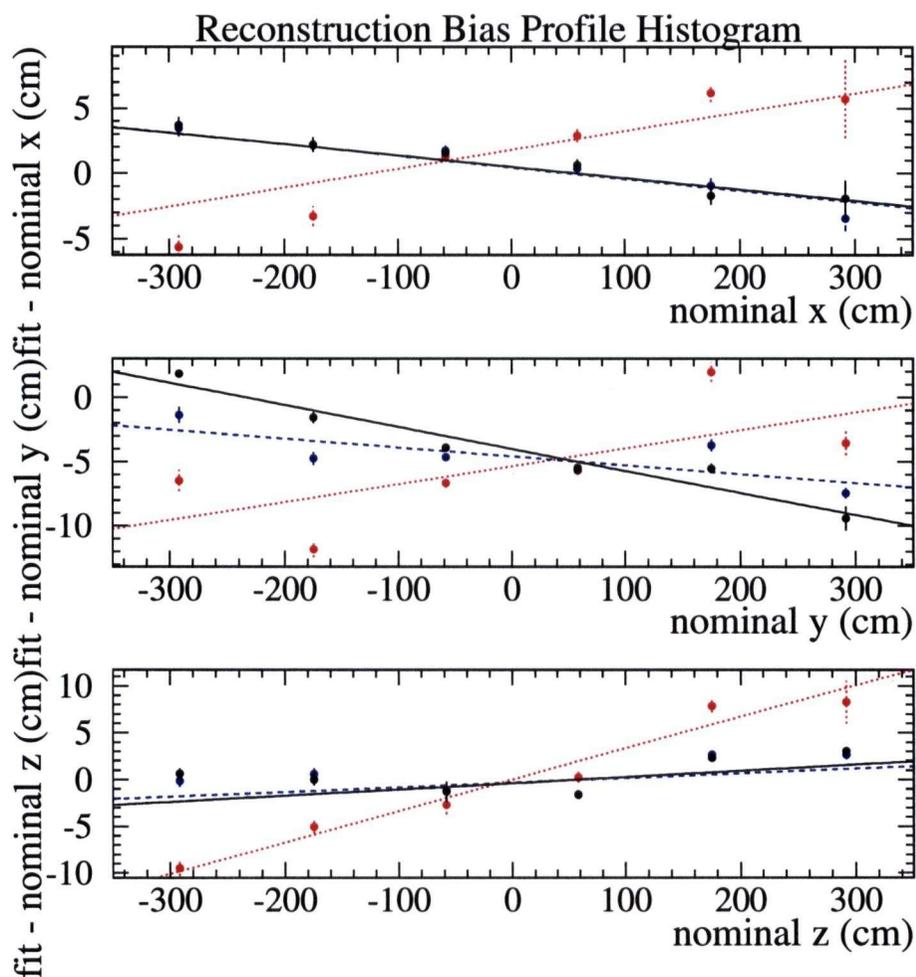
Figure 4.8: Offset between fitted and nominal (real) laserball position for the manipulator data. Black and solid represents low, blue and dashed medium and red or dotted high occupancy. The lines are a log likelihood fit to the points, which are the average of all the manipulator positions in their vicinity. The error bars represent the variance of the laserball positions used to determine the point.

Since the low and medium occupancy data agree well with the nominal ball positions and the high occupancy data does not we can conclude that there is a problem in the high charge and occupancy regime. Figure 4.9 displays the fit agreement with the nominal position for all the manipulator data.

Considering this consistent difference between low and high occupancy data we would like to investigate whether there is a relation between the positions the high and the low occupancy data fit. Figure 4.10 shows that the high occupancy data consistently constructs $\sim 3\%$ further outward than the low occupancy data.

To figure out why the high occupancy fit so disagrees with medium and low occupancy we investigate the timing over all the PMTs in the 1KT tank. Figure 4.11 shows the PMT times for high and low occupancy runs as a function of the distance from PMT to the laserball. This effect seems to be consistent with a higher effective speed of light for the high occupancy data.

4.3 Discussion

Further investigation into the construction process of the TQ-map revealed that it uses a larger integration gate than the $\pm 2ns$ gate in our analysis (see Figure 2.2). This means that the low occupancy data for the TQ-map should be affected by the scattering. In fact the scattering tail would have the TQ-map believe that all the PMTs are slow in low occupancy runs, thus subtracting from the time signal of low charge PMTs. This would effectively pull the optical fit toward the low charge PMTs since their time is wrongly corrected to an earlier value than it should be. This means that in high occupancy data the ball should reconstruct closer to the center of the 1KT since the PMTs on the side far from the laserball have a lower time than they should. This is precisely opposite to the effect displayed in Figure 4.8.

Another possible explanation is that the PMTs respond faster to photons that hit the central area of the photocathode. This is known to happen with the 20-inch Hamamatsu PMTs used in the 1KT. PMTs that are hit in a high occupancy run would alway respond to the first signal they see, which comes from that central region. For low occupancy runs only a fraction of all events hit the photocathode close to the center. The TQ-map should take out this effect, but since TQ-map only uses data from runs with the laserball in the center of the 1KT it may not correctly identify this effect for off-center low
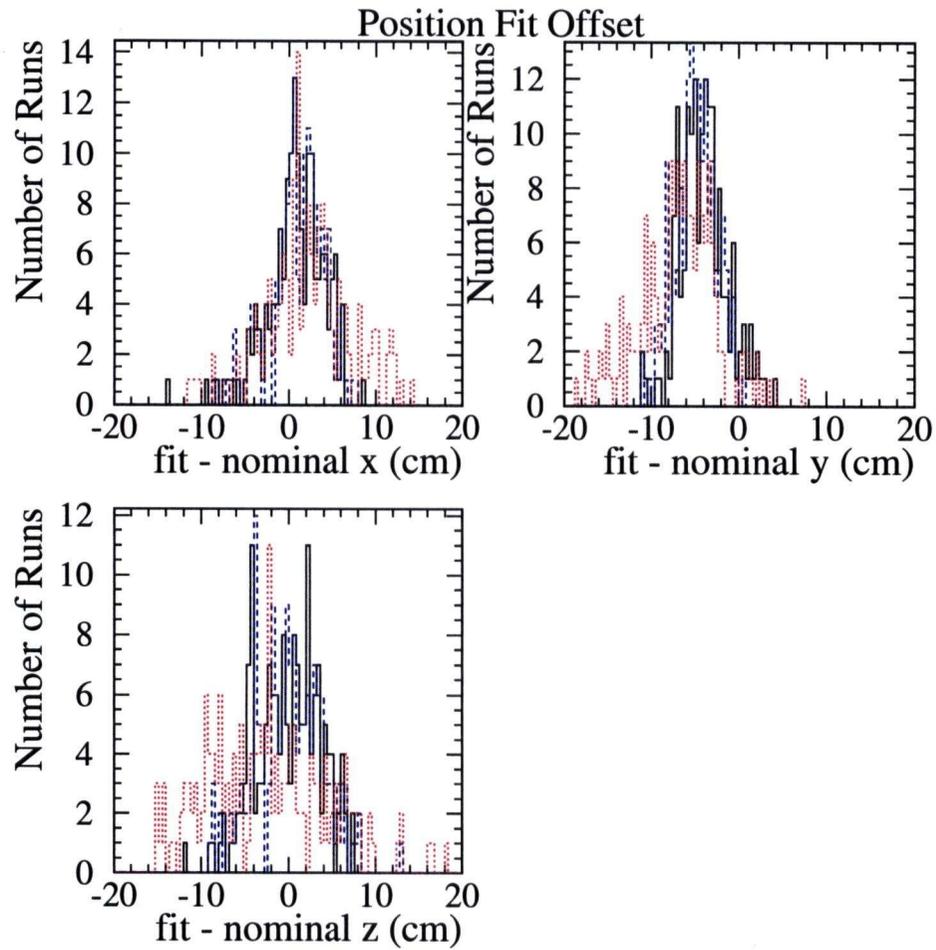
Figure 4.9: Agreement between fit and nominal positions for all manipulator data. Black and solid is low, blue and dashed is medium and red and dotted is high occupancy. Note that the high occupancy histogram is much wider than the black or blue histograms.
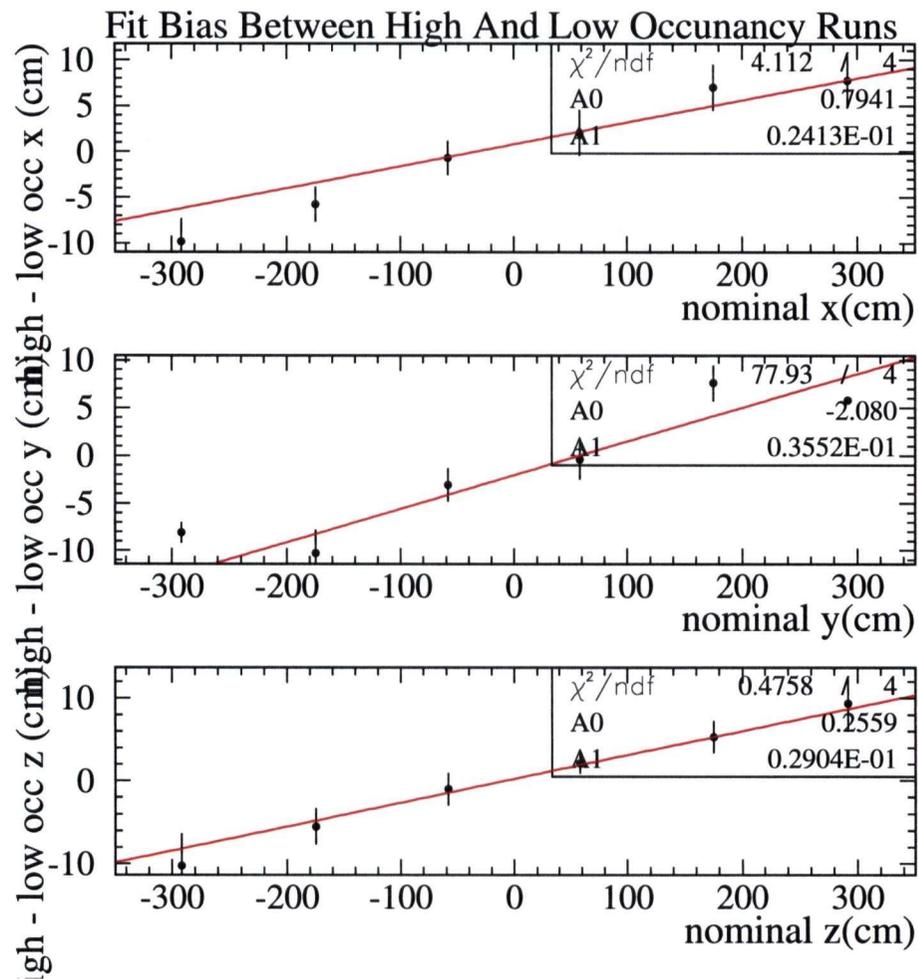
Figure 4.10: Position reconstruction bias between high and low occupancy data
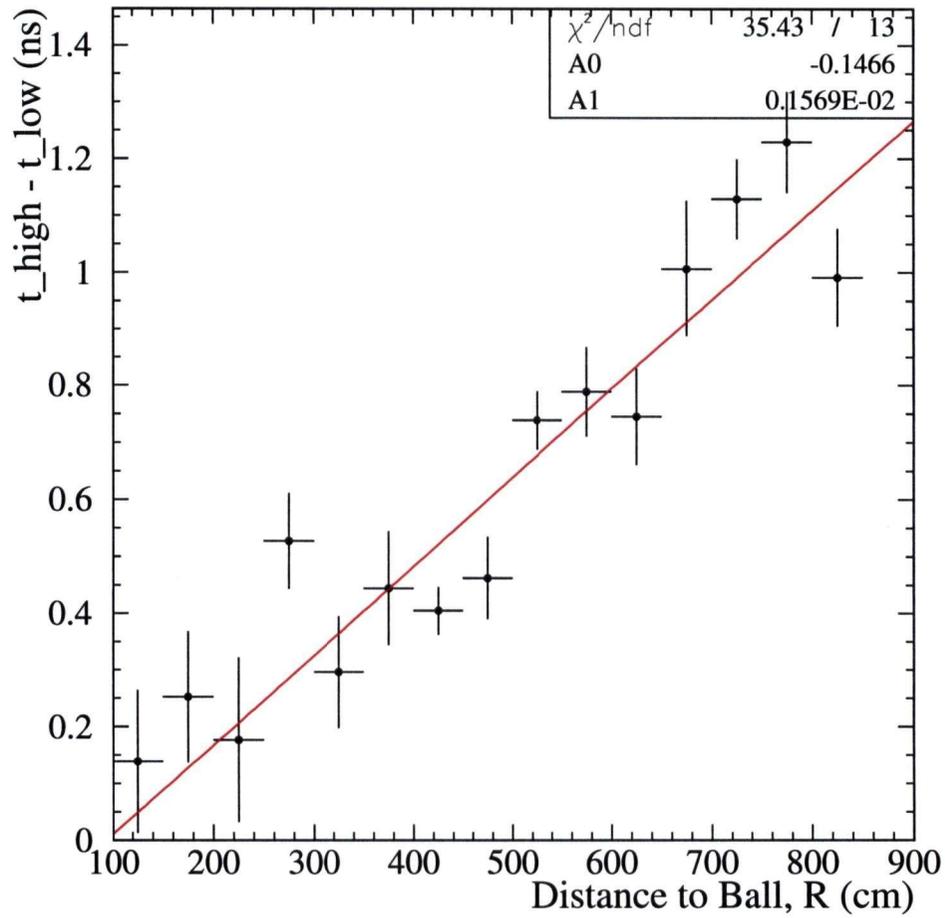
Figure 4.11: Average PMT timing differences between high and low occupancy as a function of distance between PMT and laserball.

Table 4.1: Solid angle subtended by more and less responsive areas of the photodiode as seen by the laserball moving closer to the PMT. The photodiode is modeled as a hemisphere. The central part is 0° to 2° from the top of the of the hemisphere. The middle part is defined as 2° to 10° from the top of the hemisphere. The rest is qualified as the Outer part.

Distance	Fraction of Solid Angle		
to ball	Central	Middle	Outer
430 cm	0.0031	0.0731	0.9238
330 cm	0.0031	0.0742	0.9227
230 cm	0.0032	0.0762	0.9205
130 cm	0.0035	0.0824	0.9141
30 cm	0.0086	0.1811	0.8103

occupancy runs. It is more likely for photons from the laserball to strike the PMTs in the central area of the photocathode if the laserball is closer to the PMTs. Table 4.1 shows the solid angle subtended by the sensitive areas of the PMT as the ball approaches the PMT. The quickly responding central area only becomes significant in size as the laserball gets much closer to the PMTs than we allowed the manipulator to get. Thus this effect cannot be responsible for the difference between high and low occupancy we see here.

The laserball fluoresces when excited by the large number of photons traveling though it during a high occupancy run. Thus we could have light of different wavelength in the 1KT. This could cause a different effective speed of light. But for this to be true the PMTs should respond at a different time for a high occupancy run than low occupancy run since for the ball in the center the light from the fluorescence line will travel at a different speed then the laser light. However if the light from the fluorescence were faster then the laser light we would get a slope opposite to what we see in figures 4.8 and 4.10. If the fluorescence light is slower than the laser light the PMT will record the time it was hit by the laserlight, thus negating the effect.

Chapter 5

Conclusion

A diffracting ball suspended by a string in the 1KT tank of the K2K experiment was used to demonstrate a problem with the understanding of the timing reconstruction of the 1KT. An optical position reconstruction revealed that the positions of the laserball were reconstructed about 3 cm too low, and for medium occupancy with a significant bias, pulling the position fit outward. These problems motivated the construction of the manipulator arm which allowed the exploration of the entire 1KT volume with the laserball. The positioning accuracy reached in this study is ∼3 cm, but there are still some unresolved issues in the calibration of the manipulator. The optical reconstruction of the laserball on the manipulator was possible after shadowing, scattering and reflections caused by the manipulator were identified. We find the high occupancy data reconstructs further away from the center than expected. This reconstruction bias is consistent with a lower effective speed of light in high occupancy data but the cause for this effect has not been identified.

Bibliography

[1] Issei Kato. *Indications of Neutrino Oscillation in K2K Experiment*. PhD thesis, Kyoto University, July 2005.

[2] The K2K Collaboration. A measurement of neutrino oscillations by the k2k experiment (tenative title). *Phys. Rev. Letters*, 2006.

[3] The K2K Collaboration. tdcres.dat. Code in k2k04a/skam/const/tdcres.dat, 2004.

[4] David Morris et al. An optical calibration manipulator system. Technical report, TRIUMF, 2006. Accepted for publication.

[5] John N. Bahcall, Aldo M. Serenelli, and Sarbani Basu. New solar opacities, abundances, helioseismology, and neutrino fluxes. *Astrophys. J.*, 621:L85–L88, 2005.

[6] Y. Ashie et al. A measurement of atmospheric neutrino oscillation parameters by super-kamiokande i. *Phys. Rev.*, D71:112005, 2005.

[7] Laurie M Brown. The idea of the neutrino. *Physics Today*, September 1978.

[8] C. L. Cowan, F. Reines, F. B. Harrison, H. W. Kruse, and A. D. McGuire. Detection of the free neutrino: A confirmation. *Cambridge Monogr. Part. Phys. Nucl. Phys. Cosmol.*, 14:38–42, 2000.

[9] G. Danby et al. Observation of high-energy neutrino reactions and the existence of two kinds of neutrinos. *Phys. Rev. Lett.*, 9:36–44, 1962.

[10] K. Kodama et al. Observation of tau-neutrino interactions. *Phys. Lett.*, B504:218–224, 2001.

[11] R. Davis. Solar neutrinos. ii: Experimental. *Phys. Rev. Lett.*, 12:303–305, 1964.

[12] Masao Takata and Hiromoto Shibahshi. Solar models based on helio-seismology and the solar neutrino problem. *The Astrophysical Journal*, 504:1035–1050, September 10 1998.

[13] Pontecarvo. *Sov. J. Nocl. Phys.*, 42.

[14] Vivek Agrawal, T. K. Gaisser, Paolo Lipari, and Todor Stanev. Atmospheric neutrino flux above 1 gev. *Phys. Rev.*, D53:1314–1323, 1996.

[15] G. Barr, T. K. Gaisser, and T. Stanev. Flux of atmospheric neutrinos. *Phys. Rev.*, D39:3532–3534, 1989.

[16] E. Aliu et al. Evidence for muon neutrino oscillation in an accelerator-based experiment. *Phys. Rev. Lett.*, 94:081802, 2005.

[17] Z. Maki, M. Nakagawa, and S. Sakata. Remarks on the unified model of elementary particles. *Prog. Theor. Phys.*, 28:870, 1962.

[18] Scott Oser. A walk through the neutrino mixing matrix. Talk, 2004. A talk held at TRIUMF and UBC.

[19] B. Aharmim et al. Electron energy spectra, fluxes, and day-night asymmetries of b-8 solar neutrinos from the 391-day salt phase sno data set. *Phys. Rev.*, C72:055502, 2005.

[20] The K2K Collaboration. K2k website. http://neutrino.kek.jp/, 2005.

[21] H. Noumi et al. Precision positioning of superkamiokande with gps for a long-baseline neutrino oscillation experiment. *Nucl. Instrum. Meth.*, A398:399–408, 1997.

[22] Anna Pla-Dalmau. Extruded plastic scintillator for the minos calorimeters. *Conference Proceedtings*, 2006. To be published in the proceedings of 9th Conference on Calorimetry in High Energy Physics (CALOR 2000), Annecy, France, 9-14 Oct 2000.

[23] Super Kamiokande Collaboration. Official super kamiokande website. http://www-sk.icrr.u-tokyo.ac.jp/sk/, 2006.

[24] Joanna Zalipska. Detector tuning laser calibration and cr muons. Talk reviewing laser scattering study done for the 1KT, 2004.

[25] Newport Corporation. Vsl-337 nitrogen laser product detail. http://www.newport.com.

[26] MIDAS Group. Midas triumf homepage. http://midas.triumf.ca, 2006.

[27] Ricardo Dao. Temperature compensated 360° inclinometer with asynchronour serial output. Reference Design #RD-00MX-001, MEMSIC Inc., 2004.

[28] Shunichi Mine. Energy scale. K2K Collaboration Meeting, 2005.

Appendix A

Data With Laserball On A String

The setup for collecting the optical calibration data using the laserball is described in Section 2.1. The laserball data taken is summarized in tables A.1, A.2 and A.3. The laserball could be positioned accurate to 10 cm for the data taken in October 2003, 5 cm for the data taken in Spring 2004 and about 3 cm for data taken in the Summer of 2005.

The nominal position of the laserball is determined by measuring the desired height from a piece of tape on the wire holding the ball in the tank that indicating where to put the ball to suspend it in the center of the tank. Then the wire is fixed at the measured position.

Note that for runs 613342 to 98 the voltage supply to the photo-diode was turned off. This means the timing signal supplied by the photo-diode is unstable making the position reconstruction for these runs very inaccurate.

Table A.1: Summary of data taken with laserball on a string. Height in tank is the z position of the ball in the tank coordinate system (see Figure 1.15)

Run Number	Height (cm)	Occupancy	Events	Notes
October 2003 Data:				
603039	0	45	13,000	
603041	300	45	25,000	
Spring 2004 Data:				
602960	0	57	20,000	
602963	0	79.5	20,000	
602964	0	140	20,000	
602965	0	200	20,000	
602966	0	300	10,000	
602969	0	400	10,000	
602972	0	500	10,000	
602973	0	580	5,000	
602974	0	600	5,000	
602975	0	605	5,000	
602976	0	619	5,000	
602978	0	650	5,000	
602980	0	675	3,000	
602981	0	675	3,000	
602983	0	675	3,000	
602984	0	675	3,000	
602985	0	675	3,000	
602986	0	675	3,000	
602987	0	675	2,000	
602988	0	675	2,000	
602989	0	675	2,000	
602993	0	680	2,000	
602994	0	680	2,000	
602995	0	680	2,000	
602996	0	680	2,000	
602997	0	680	2,000	
602998	0	680	2,000	
603000	-200	678	5,000	Problems with timing
603002	-200	60	40,000	
603004	-200	160	29,000	
603039	0	45	12,000	
603041	300	45	20,000	
603045	0	150		
603047	0	150	10,000	

Table A.2: Data taken with laserball on string Part 2

Run Number	Height (cm)	Occupancy	Events	Notes
July 2004 Data:				
603050	-200	250	7,000	
603051	200	250	10,000	
613342	-300	45	20,000	Photo diode Voltage is off
613346	-300	375	3,000	Photo diode Voltage is off
613348	-300	300	4,500	Photo diode Voltage is off
613350	-300	25	30,000	Photo diode Voltage is off
613351	-300	50	40,000	Photo diode Voltage is off
613352	-300	100		Photo diode Voltage is off
613353	-300	190	16,000	Photo diode Voltage is off
613354	-300	230	2,000	Photo diode Voltage is off
613356	300	150	6,000	Photo diode Voltage is off
613364	300	low		Photo diode Voltage is off
613374	300	30		Photo diode Voltage is off
613389	300	400	25,000	Photo diode Voltage is off
613391	300	180	30,000	Photo diode Voltage is off
613393	300	25	67,000	Rotate ball by 180°
				Photo diode Voltage is off
613396	200	420		Rotate ball back
				Photo diode Voltage is off
613398	200	200		Photo diode Voltage is off
613399	200	200 → 70		
613401	200	30		
613402	200	30		Rotate ball by 180°
613405	100	200 → 150		Rotate ball back
613408	100	600		
613410	100	25		
613412	100	25		Rotate ball by 180°
613414	0	580		Rotate ball back
613417	0	25		
613419	0	25		Rotate ball by 180°
613421	-100	520		Rotate ball back
613423	-100	200		
613425	-100	25		

Table A.3: Data taken with laserball on string Part 3

Run Number	Height (cm)	Occupancy	Events	Notes
June 2005 Data:				
615632	0	20	5,000	
615633	0	500	5,000	
615634	0	679	20,000	
615636	-298	680	5,000	
615637	-298	500	5,000	
615638	-298	20	20,000	
615641	-170	20	20,000	
615642	-170	500	5,000	
615643	-170	680	5,000	
615645	127	680	5,000	
615646	127	500	5,000	
615647	127	20	20,000	
615649	273	680	5,000	
615650	273	500	5,000	
615651	273	20	20,000	

Appendix B

Manipulator Data

The laser setup for the these runs using the manipulator is the the same as the setup for the laserball on a string described in Section 2.1. The Manipulator and its operation is described in Chapter 3. The runs here were taken between April 25, 2005 and June 14, 2005.

The ball position is given in the tank coordinate system. In low occupancy runs 20, medium occupancy runs 480 and high occupancy runs 680 PMTs are hit on average. The nitrogen laser broke during run 615550 and was replaced. The missing runs between 615550 and 615597 were used find the problem and test the replacement laser.

The data from the online database summarizing the complete manipulator status during each run is available at:

http://trshare.triumf.ca/~berghaus/work/manipulator/online/odb/

Sketches of the manipulator orientations in each of the run plan sections are available at:

http://phys01.comp.uvic.ca:8080/t2k/Members/frank/Runplan/view/

Table B.1: Summary of manipulator runs taken at KEK

Run Plan	Run Number	X (cm)	Y (cm)	Z (cm)	Occupancy
A3	615026	-77.50	73.28	-301.34	low
A3	615027	-77.50	73.28	-301.34	medium
A3	615028	-77.50	73.28	-301.34	high
A4	615029	-76.27	71.90	-296.18	high
A4	615030	-76.27	71.90	-296.18	medium
A4	615031	-76.27	71.90	-296.18	low
A5	615032	-72.64	67.95	-296.75	low
A5	615033	-72.64	67.95	-296.75	medium
A5	615034	-72.64	67.95	-296.75	high
A6	615035	-71.70	66.98	-304.18	high
A6	615036	-71.70	66.98	-304.18	medium
A6	615037	-71.74	66.96	-304.01	low
B1	615038	172.90	-199.58	-127.81	high
B1	615039	172.90	-199.58	-127.81	medium
B1	615040	172.90	-199.58	-127.81	low
B1	615041	172.90	-199.58	-127.81	low
B2	615043	-76.32	71.94	-132.60	high
B2	615044	-76.32	71.94	-132.60	medium
B2	615045	-76.32	71.94	-132.60	low
B3	615046	47.26	-60.05	-311.38	high
B3	615047	47.26	-60.05	-311.38	medium
B3	615048	47.26	-60.05	-311.38	low
B4	615049	173.43	-200.11	-128.46	low
B4	615050	173.43	-200.11	-128.46	medium
B4	615051	173.43	-200.11	-128.46	high
B5	615052	65.88	-81.42	-201.64	high
B5	615053	65.88	-81.42	-201.64	medium
B5	615054	65.88	-81.42	-201.64	low
B6	615055	41.50	-54.31	-93.42	low
B6	615056	41.95	-54.37	-93.48	medium

Table B.2: Manipulator runs table 2

Run Plan	Run Number	X (cm)	Y (cm)	Z (cm)	Occupancy
B6	615057	40.78	-55.19	-93.57	high
B7	615058	45.87	-60.72	-311.89	high
B7	615059	46.63	-60.25	-311.61	medium
B7	615060	46.53	-60.13	-311.85	low
C1	615061	99.34	-204.60	-198.20	low
C1	615062	99.34	-204.60	-198.20	medium
C1	615063	99.34	-204.60	-198.20	high
C2	615064	-133.41	-195.40	-197.01	high
C2	615065	-134.27	-195.41	-197.01	medium
C2	615066	-133.41	-195.42	-197.13	low
C3	615067	-243.27	10.47	-198.27	high
C3	615068	-242.96	10.38	-198.22	medium
C3	615069	-243.03	10.56	-198.05	low
C4	615070	-120.17	204.17	-199.87	high
C4	615071	-120.01	204.09	-200.05	medium
C4	615072	-119.82	203.87	-199.75	low
C5	615073	110.79	198.14	-196.13	high
C5	615074	110.79	198.01	-196.12	medium
C5	615075	110.91	197.63	-195.77	low
C6	615076	220.54	-7.37	-196.81	low
C6	615077	220.74	-7.35	-196.95	medium
C6	615078	220.66	-8.33	-196.85	high
C7	615079	219.66	-7.14	207.20	high
C7	615080	219.78	-7.18	207.25	medium
C7	615081	220.04	-7.24	207.03	low
C8	615082	109.71	198.95	206.31	high
C8	615083	109.71	198.95	206.31	medium
C8	615084	109.71	198.95	206.31	low
C9	615085	-118.68	199.84	206.71	high
C9	615086	-118.60	199.92	207.07	medium

Table B.3: Manipulator runs table 3

Run Plan	Run Number	X (cm)	Y (cm)	Z (cm)	Occupancy
C9	615087	-118.71	199.91	206.85	low
C10	615088	-236.48	13.31	204.82	high
C10	615089	-236.43	13.33	204.64	medium
C10	615090	-236.50	13.61	204.61	low
C11	615091	-132.32	-186.29	207.34	high
C11	615092	-132.31	-186.59	207.35	medium
C11	615093	-131.18	-186.63	207.29	low
C12	615094	94.46	-196.03	210.89	high
C12	615095	94.52	-196.06	210.84	medium
C12	615096	94.09	-196.32	211.04	low
D1	615097	190.81	-218.11	13.19	high
D1	615098	191.77	-217.18	13.38	medium
D1	615099	191.28	-217.67	12.99	low
D2	615100	183.62	-214.11	14.61	high
D2	615101	185.03	-212.79	14.63	medium
D2	615102	183.59	-214.08	14.46	low
J1	615103	66.70	-83.91	220.43	medium
J1	615104	66.70	-83.91	220.43	high
J1	615105	65.88	-84.54	220.31	low
J2	615106	65.83	-82.94	-202.03	high
J2	615107	64.88	-83.44	-202.17	medium
J2	615108	65.17	-83.23	-202.22	low
J3	615109	170.18	-195.77	-144.71	high
J3	615110	169.26	-196.51	-144.66	medium
J3	615111	173.56	-192.36	-144.43	low
J4	615112	-116.39	115.76	-150.52	high
J4	615113	-116.18	115.67	-150.19	medium
J4	615114	-116.45	115.81	-150.50	low
E1	615115	-75.07	68.37	-296.46	high
E1	615116	-75.09	68.00	-296.32	medium

Table B.4: Manipulator runs table 4

Run Plan	Run Number	X (cm)	Y (cm)	Z (cm)	Occupancy
E1	615117	-75.07	68.27	-296.38	low
E2	615118	-76.42	70.56	-296.54	high
E2	615119	-76.24	70.55	-296.63	medium
E2	615120	-76.32	70.54	-296.61	low
E3	615121	-74.91	72.39	-296.59	high
E3	615122	-74.91	72.32	-296.30	medium
E3	615123	-74.92	72.33	-296.52	low
E4	615124	-72.21	70.39	-296.75	high
E4	615125	-71.93	70.36	-296.83	medium
E4	615126	-72.24	70.36	-296.75	low
F1	615127	-283.86	81.40	-316.49	high
F1	615128	-283.92	81.98	-316.56	medium
F1	615129	-284.06	81.99	-316.49	low
F1	615130	-295.62	82.86	-295.67	high
F1	615131	-295.62	82.86	-295.67	high
F1	615132	-295.59	81.87	-295.71	medium
F1	615133	-188.94	76.45	-296.31	low
F2	615134	-189.14	76.58	-296.37	high
F2	615135	-188.79	76.49	-296.27	medium
F2	615136	-189.17	76.31	-296.27	low
F3	615137	28.32	67.01	-296.96	high
F3	615138	28.32	67.01	-296.96	medium
F3	615139	28.32	67.01	-296.96	low
F4	615140	28.21	66.46	-296.73	high
F4	615141	28.33	66.48	-296.50	medium
F4	615142	28.31	66.31	-296.76	low
F5	615143	122.87	63.48	-294.68	high
F5	615144	122.44	62.43	-294.95	medium
F5	615145	122.65	62.48	-295.13	low
G1	615146	129.21	62.79	-297.51	high

Table B.5: Manipulator runs table 5

Run Plan	Run Number	X (cm)	Y (cm)	Z (cm)	Occupancy
G1	615147	129.15	63.95	-297.76	medium
G1	615148	56.44	226.41	-297.99	low
G2	615149	-277.64	80.01	-298.58	high
G2	615150	-277.63	81.29	-298.55	medium
G2	615152	-277.37	81.15	-298.67	low
G3	615153	-278.71	81.22	-196.80	high
G3	615154	-278.71	81.70	-196.84	medium
G3	615155	-278.46	81.68	-196.38	low
G4	615156	130.01	62.24	-195.55	high
G4	615157	129.51	62.20	-195.72	medium
G4	615158	122.35	63.10	-88.87	low
G5	615159	121.95	62.95	-88.86	high
G5	615160	122.37	62.55	-89.11	medium
G5	615161	121.99	63.29	-88.74	low
G6	615165	-271.51	81.30	-90.22	high
G6	615166	-271.33	81.37	-90.17	medium
G6	615167	-271.60	80.43	-90.22	low
G7	615168	-279.79	79.88	0.34	high
G7	615169	-280.11	81.42	0.33	medium
G7	615170	-279.87	80.71	0.14	low
G8	615171	129.70	62.54	1.37	high
G8	615172	129.98	61.77	1.68	medium
G8	615173	129.85	61.90	1.44	low
G9	615174	129.33	61.69	102.57	high
G9	615175	129.26	62.15	102.06	medium
G9	615176	129.16	62.27	102.18	low
G10	615177	-279.69	81.53	101.16	high
G10	615178	-279.74	81.62	101.11	medium
G10	615179	-279.47	81.17	100.79	low
G11	615180	-275.84	81.32	206.95	high

Table B.6: Manipulator runs table 6

Run Plan	Run Number	X (cm)	Y (cm)	Z (cm)	Occupancy
G11	615181	-275.55	81.39	206.82	medium
G11	615182	-276.03	81.55	206.54	low
G12	615184	124.73	62.39	208.06	high
G12	615185	124.75	60.58	208.27	medium
G12	615186	124.53	61.78	208.19	low
G13	615187	115.78	62.11	310.88	high
G13	615188	115.61	62.44	311.11	medium
G13	615189	115.60	62.71	311.05	low
G14	615190	-267.10	80.53	310.06	high
G14	615191	-267.09	80.20	309.94	medium
G14	615192	-267.01	81.25	310.06	low
H1	615193	-13.08	4.16	312.22	high
H1	615194	-13.85	3.65	312.59	medium
H1	615195	-12.96	4.50	312.76	low
H2	615196	-7.76	-2.75	211.29	high
H2	615197	-7.66	-2.61	211.13	medium
H2	615198	-7.07	-2.29	211.25	low
H3	615199	-5.25	-5.23	105.33	high
H3	615200	-5.43	-5.54	105.61	medium
H3	615201	-5.50	-5.46	105.38	low
H4	615202	-6.95	-2.90	4.31	high
H4	615203	-6.95	-2.90	4.31	medium
H4	615204	-7.25	-3.31	4.24	low
H5	615205	-0.82	-9.23	-96.53	high
H5	615206	-0.11	-8.44	-96.53	medium
H5	615207	-0.65	-9.67	-96.83	low
H6	615208	2.03	-12.86	-197.24	high
H6	615209	1.97	-12.77	-196.94	medium
H6	615210	1.89	-12.70	-196.95	low
H7	615211	1.73	-12.53	-295.82	high

Table B.7: Manipulator runs table 7

Run Plan	Run Number	X (cm)	Y (cm)	Z (cm)	Occupancy
H7	615212	1.48	-12.53	-295.83	medium
H7	615213	1.83	-12.35	-295.84	low
L1	615214	3.77	268.28	-191.21	high
L1	615215	4.26	268.09	-191.06	medium
L1	615216	3.18	268.67	-191.33	low
L2	615217	1.71	199.09	-192.75	high
L2	615218	1.62	199.10	-192.85	medium
L2	615219	1.66	198.68	-192.73	low
L3	615220	-1.05	98.38	-196.34	high
L3	615221	-0.87	98.62	-196.00	medium
L3	615222	-0.56	98.81	-193.71	low
L4	615223	-6.91	-3.19	-189.01	high
L4	615224	-7.09	-3.23	-188.98	medium
L4	615225	-6.81	-3.29	-188.78	low
L5	615226	-13.50	-98.19	-183.57	high
L5	615227	-13.52	-98.04	-184.89	medium
L5	615228	-13.45	-98.32	-184.97	low
L6	615229	-19.92	-195.88	-187.14	high
L6	615230	-16.38	-195.04	-187.67	medium
L6	615231	-16.27	-195.31	-187.86	low
L7	615232	-16.57	-272.90	-190.01	high
L7	615233	-21.24	-273.60	-189.96	medium
L7	615234	-20.06	-273.50	-189.66	low
K1	615235	260.15	-13.49	-191.75	low
K1	615236	260.74	-11.74	-191.51	medium
K1	615237	260.39	-12.95	-191.44	high
K2	615238	189.56	-9.27	-187.05	high
K2	615239	190.04	-8.96	-186.68	medium
K2	615240	116.49	-18.15	-200.45	low
K3	615241	90.68	-6.93	-186.66	high

Table B.8: Manipulator runs table 8

Run Plan	Run Number	X (cm)	Y (cm)	Z (cm)	Occupancy
K3	615242	91.13	-6.42	-187.44	medium
K3	615243	90.88	-6.30	-187.14	low
K4	615244	-7.63	-2.39	-185.20	high
K4	615245	-7.76	-2.50	-186.33	low
K4	615246	-7.91	-2.34	-186.24	medium
K5	615247	-108.56	2.16	-190.26	high
K5	615248	-107.78	1.81	-190.34	medium
K5	615249	-108.02	1.49	-190.49	low
K6	615250	-204.67	7.79	-189.12	high
K6	615251	-205.43	9.86	-189.52	medium
K6	615252	-204.51	8.22	-190.35	low
K7	615253	-270.36	12.05	-186.25	high
K7	615254	-269.80	12.11	-185.79	medium
K7	615255	-269.99	11.20	-185.85	low
M1	615256	268.49	-13.81	6.02	high
M1	615257	268.61	-13.84	6.10	medium
M1	615258	268.72	-13.78	6.13	low
M2	615259	195.82	-10.20	5.95	high
M2	615260	195.45	-10.15	5.77	medium
M2	615261	195.86	-10.57	5.91	low
M3	615262	96.02	-7.85	2.41	high
M3	615263	95.66	-7.77	2.25	medium
M3	615264	96.27	-7.89	2.37	low
M4	615265	-3.88	-5.99	2.24	high
M4	615266	-4.31	-6.78	2.18	medium
M4	615267	-4.02	-6.56	2.19	low
M5	615268	-110.75	-4.22	2.22	high
M5	615269	-110.88	-3.51	2.26	medium
M5	615270	-111.03	-4.14	2.18	low
M6	615271	-210.95	3.61	2.33	low

Table B.9: Manipulator runs table 9

Run Plan	Run Number	X (cm)	Y (cm)	Z (cm)	Occupancy
M6	615272	-211.34	4.37	2.40	medium
M6	615273	-211.38	4.06	2.46	high
M7	615274	-279.02	6.82	5.44	high
M7	615275	-279.36	7.85	5.17	medium
M7	615276	-279.13	6.78	5.49	low
N1	615277	3.61	269.05	5.75	high
N1	615278	2.00	269.71	6.02	medium
N1	615279	3.51	268.81	5.73	low
N2	615280	3.87	203.40	2.82	high
N2	615281	3.44	203.69	2.88	medium
N2	615282	4.04	203.33	2.74	low
N3	615283	4.02	100.63	1.63	high
N3	615284	3.60	100.44	1.74	medium
N3	615285	3.56	100.58	1.61	low
N4	615286	-3.79	-7.06	1.95	high
N4	615287	-3.63	-7.00	1.83	medium
N4	615288	-4.65	-5.66	1.55	low
N5	615289	-11.21	-103.64	3.77	high
N5	615290	-12.45	-103.81	3.72	medium
N5	615291	-11.83	-103.60	3.97	low
N6	615292	-13.99	-203.19	7.23	low
N6	615293	-16.70	-203.89	7.30	medium
N6	615294	-15.92	-203.49	7.27	high
N7	615295	-18.24	-274.53	9.48	high
N7	615296	-18.67	-274.68	9.78	medium
N7	615297	-17.60	-274.38	9.95	low
O1	615298	99.29	-9.51	-201.04	high
O1	615299	99.53	-9.23	-200.97	medium
O1	615300	99.39	-9.60	-201.48	low
O2	615301	-10.59	-109.89	-201.72	high

Table B.10: Manipulator runs table 10

Run Plan	Run Number	X (cm)	Y (cm)	Z (cm)	Occupancy
O2	615302	-8.56	-109.33	-201.58	medium
O2	615303	-10.93	-109.89	-201.67	low
O3	615304	-112.54	-8.50	-208.69	high
O3	615305	-112.63	-8.34	-208.56	medium
O3	615306	-112.90	-8.30	-208.64	low
O4	615307	6.86	102.00	-208.96	high
O4	615308	7.07	101.87	-209.09	medium
O4	615309	7.00	102.09	-208.89	low
O5	615310	1.09	100.02	-109.47	high
O5	615311	1.16	100.21	-109.65	medium
O5	615312	1.16	100.21	-109.65	medium
O5	615313	1.16	100.21	-109.65	low
O6	615314	1.16	100.21	-109.65	high
O6	615316	1.16	100.21	-109.65	low
O7	615317	1.16	100.21	-109.65	high
O7	615318	1.16	100.21	-109.65	medium
O7	615319	1.16	100.21	-109.65	low
O8	615320	94.17	-6.82	-100.76	high
O8	615321	94.46	-7.10	-100.89	medium
O8	615322	94.63	-6.30	-100.86	low
O9	615323	93.52	-6.41	1.32	high
O9	615324	93.16	-6.36	1.27	medium
O9	615325	93.20	-6.34	1.33	low
O10	615326	-13.11	-103.83	0.95	high
O10	615327	-13.08	-103.84	1.11	medium
O10	615328	-13.77	-103.84	1.02	low
O11	615329	-109.25	-3.17	-1.74	high
O11	615330	-109.82	-3.17	-1.57	medium
O11	615331	-109.24	-3.28	-1.59	low
O12	615332	0.92	99.86	-1.24	high

Table B.11: Manipulator runs table 11

Run Plan	Run Number	X (cm)	Y (cm)	Z (cm)	Occupancy
O12	615333	0.88	99.70	-1.30	medium
O12	615334	0.66	99.53	-1.48	low
O13	615335	-3.84	97.95	106.34	high
O13	615336	-3.87	98.18	106.14	medium
O13	615337	-3.89	98.27	106.32	low
O14	615338	-108.53	1.65	106.00	high
O14	615339	-109.01	1.83	106.35	medium
O14	615340	-108.73	1.69	106.23	low
O15	615341	-15.37	-99.20	101.02	high
O15	615342	-14.84	-98.88	100.85	medium
O15	615343	-14.29	-98.77	100.86	low
O16	615344	88.82	-3.33	100.86	high
O16	615345	88.83	-4.27	101.32	medium
O16	615347	88.61	-3.90	100.68	low
P1	615348	197.04	-17.13	-196.81	high
P1	615349	197.89	-14.42	-196.99	medium
P1	615350	58.80	243.34	-211.00	low
P2	615351	-17.35	-206.21	-198.29	high
P2	615352	-16.91	-206.23	-197.98	medium
P2	615353	-16.98	-205.66	-198.19	low
P3	615354	-214.06	0.88	-202.20	high
P3	615355	-214.63	1.51	-201.98	medium
P3	615356	-214.64	1.68	-202.16	low
P4	615357	4.05	205.24	-201.87	high
P4	615358	4.41	204.82	-202.00	medium
P4	615359	4.00	205.16	-202.28	low
P5	615360	1.72	202.26	-102.73	high
P5	615361	1.97	201.54	-102.36	medium
P5	615362	2.18	201.89	-102.68	low
P6	615363	-212.86	6.20	-103.31	low

Table B.12: Manipulator runs table 12

Run Plan	Run Number	X (cm)	Y (cm)	Z (cm)	Occupancy
P6	615364	-213.09	6.47	-103.33	medium
P6	615365	-213.02	6.61	-103.30	high
P7	615366	-18.96	-202.58	-99.01	high
P7	615367	-19.42	-202.67	-98.85	medium
P7	615368	-18.52	-202.64	-99.01	low
P8	615369	191.94	-10.45	-99.13	high
P8	615370	191.74	-10.46	-98.79	medium
P8	615371	191.83	-10.49	-98.76	low
P9	615372	187.00	-8.96	1.52	high
P9	615373	186.65	-9.46	1.40	medium
P9	615374	186.15	-9.25	1.17	low
P10	615375	-12.26	-198.50	2.46	high
P10	615376	-10.70	-198.56	2.45	medium
P10	615377	-13.15	-198.84	2.42	low
P11	615378	-208.27	4.74	-1.75	high
P11	615379	-208.16	4.32	-1.93	medium
P11	615380	-207.98	5.07	-1.88	low
P12	615381	1.24	197.97	-1.43	high
P12	615382	0.73	198.43	-1.47	medium
P12	615383	1.35	197.99	-1.44	low
P13	615384	1.34	198.96	100.77	low
P13	615385	1.27	199.00	100.60	low
P13	615386	1.21	198.91	100.82	medium
P13	615387	1.26	199.00	100.69	high
P14	615388	-208.91	3.37	100.14	high
P14	615389	-208.72	3.27	100.08	medium
P14	615390	-209.15	3.45	100.42	low
P15	615391	-20.80	-198.25	103.95	high
P15	615392	-19.94	-198.10	103.84	medium
P15	615393	-19.45	-198.13	103.82	low

Table B.13: Manipulator runs table 13

Run Plan	Run Number	X (cm)	Y (cm)	Z (cm)	Occupancy
P16	615394	188.09	-5.41	105.03	high
P16	615395	188.48	-5.10	105.07	medium
P16	615396	188.44	-5.16	104.80	low
Q1	615397	172.77	-200.39	-121.59	high
Q1	615398	171.97	-201.29	-121.21	medium
Q1	615399	173.27	-199.98	-121.52	low
Q2	615400	-76.37	72.01	-132.64	low
Q2	615401	-76.40	72.03	-132.53	medium
Q2	615402	-76.36	72.00	-132.45	high
Q3	615403	46.22	-60.66	-311.68	high
Q3	615404	46.36	-60.81	-311.26	medium
Q3	615405	46.37	-60.81	-311.72	low
Q4	615406	174.29	-199.22	-128.73	high
Q4	615407	173.83	-199.64	-128.57	medium
Q4	615408	174.80	-198.88	-128.41	low
Q5	615409	50.92	-63.51	110.42	low
Q5	615410	50.53	-63.96	110.41	medium
Q5	615411	50.30	-64.17	110.35	high
Q6	615412	49.57	-62.94	-311.90	high
Q6	615413	49.40	-64.09	-310.56	medium
Q6	615414	49.07	-63.29	-311.80	low
Q7	615416	-0.79	-7.47	-298.56	high
Q7	615417	-1.13	-8.10	-298.63	medium
Q7	615418	-1.30	-8.19	-298.33	low
Q8	615419	-54.00	48.01	-248.10	high
Q8	615420	-53.91	48.07	-247.49	medium
Q8	615421	-54.12	47.98	-247.98	low
Q9	615422	-86.81	83.27	-170.06	low
Q9	615423	-86.78	83.33	-170.13	medium
Q9	615424	-86.99	83.34	-170.08	high

Table B.14: Manipulator runs table 14

Run Plan	Run Number	X (cm)	Y (cm)	Z (cm)	Occupancy
Q10	615425	-94.87	91.85	-97.76	high
Q10	615427	-94.81	91.94	-97.75	medium
Q10	615428	-94.90	91.74	-97.33	low
Q11	615429	192.45	-217.88	-99.14	low
Q11	615430	191.92	-218.32	-99.32	medium
Q11	615431	199.04	-211.62	-99.11	high
Q12	615432	182.70	-209.22	-28.72	high
Q12	615433	184.16	-207.99	-28.12	medium
Q12	615434	184.09	-208.03	-28.52	low
Q13	615435	149.97	-173.73	47.88	low
Q13	615436	153.24	-170.72	47.76	medium
Q13	615437	154.40	-169.63	48.22	high
Q14	615438	99.07	-116.57	97.43	low
Q14	615439	99.70	-115.99	97.25	medium
Q14	615440	99.44	-116.34	97.33	high
Q3R	615441	45.44	-60.69	-312.24	low
Q3R	615442	47.15	-59.48	-312.02	medium
Q3R	615443	46.66	-59.35	-312.01	high
Q15	615444	64.69	-78.60	-201.83	high
Q15	615445	64.78	-78.74	-202.00	medium
Q15	615446	65.41	-77.90	-201.88	low
Q16	615447	40.17	-54.96	-92.25	high
Q16	615448	40.53	-54.92	-92.28	medium
Q16	615449	42.48	-52.85	-92.08	low
Q17	615450	-9.11	-1.03	-79.09	high
Q17	615451	-7.68	-0.20	-79.28	medium
Q17	615452	-8.03	-0.54	-79.29	low
Q18	615453	-52.50	46.23	-41.18	low
Q18	615454	-52.52	46.10	-41.23	medium
Q18	615455	-52.24	46.04	-41.54	high

Table B.15: Manipulator runs table 15

Run Plan	Run Number	X (cm)	Y (cm)	Z (cm)	Occupancy
Q19	615456	188.49	-205.34	120.31	low
Q19	615457	184.98	-208.88	119.98	medium
Q19	615458	186.30	-207.54	120.01	high
Q20	615459	177.31	-200.67	182.17	high
Q20	615460	178.97	-198.89	182.44	medium
Q20	615461	176.44	-201.54	182.15	low
Q21	615462	136.64	-151.77	280.18	low
Q21	615463	135.45	-152.65	280.34	medium
Q21	615464	134.29	-153.67	280.40	high
Q22	615465	91.83	-108.19	316.69	high
Q22	615466	91.34	-108.24	316.96	medium
Q22	615467	89.64	-110.06	316.69	low
Q23	615468	42.23	-55.50	330.21	high
Q23	615469	42.12	-55.79	330.06	medium
Q23	615470	41.53	-56.08	330.18	low
W1	615471	-13.60	-205.17	-266.51	high
W1	615472	-11.48	-203.75	-267.14	high
W1	615473	-11.35	-204.04	-266.91	medium
W1	615474	-10.87	-204.02	-266.85	low
W2	615475	192.48	-8.28	-268.34	high
W2	615476	192.66	-8.33	-268.08	medium
W2	615477	192.67	-7.85	-268.19	low
W3	615478	192.09	-8.10	-215.51	low
W3	615479	191.96	-6.95	-215.85	medium
W3	615480	191.88	-7.97	-215.70	high
W4	615481	-13.16	-200.41	-216.11	high
W4	615482	-14.95	-201.02	-216.15	medium
W4	615483	-12.72	-200.23	-216.28	low
W5	615484	-14.64	-196.02	-111.81	high
W5	615485	-13.00	-195.78	-112.01	medium

Table B.16: Manipulator runs table 16

Run Plan	Run Number	X (cm)	Y (cm)	Z (cm)	Occupancy
W5	615486	-13.65	-196.17	-111.81	low
W6	615487	184.63	-6.38	-112.36	high
W6	615488	184.94	-6.54	-112.41	medium
W6	615489	184.56	-5.69	-112.31	low
W7	615490	193.02	-11.41	-17.37	high
W7	615491	192.99	-11.27	-17.51	medium
W7	615492	192.83	-11.35	-17.50	low
W8	615493	-14.17	-200.71	-16.46	high
W8	615494	-16.85	-201.18	-16.39	medium
W8	615495	-14.54	-200.71	-16.52	low
W9	615496	-13.49	-199.20	81.80	high
W9	615497	-14.73	-199.86	82.19	medium
W9	615498	-13.93	-199.38	81.79	low
W10	615499	191.32	-5.92	82.13	low
W10	615500	190.73	-8.19	82.32	medium
W10	615501	190.76	-6.53	82.28	high
W10	615503	190.72	-7.70	82.33	high
W11	615504	187.24	-6.74	189.07	low
W11	615505	187.45	-6.34	188.79	medium
W11	615506	186.58	-7.93	189.14	high
W12	615507	-14.86	-195.50	188.42	low
W12	615508	-15.10	-196.07	188.14	low
W12	615509	-14.88	-195.42	188.41	medium
W12	615510	-13.24	-195.21	187.96	high
W13	615511	-16.44	-186.70	292.58	high
W13	615512	-17.16	-186.92	292.52	medium
W13	615513	-16.77	-186.59	292.70	low
W14	615514	176.02	-6.68	293.20	high
W14	615515	176.26	-5.51	293.46	medium
W14	615516	176.27	-5.76	293.23	low

Table B.17: Manipulator runs table 17

Run Plan	Run Number	X (cm)	Y (cm)	Z (cm)	Occupancy
X1	615517	240.65	-12.10	5.98	high
X1	615518	240.92	-11.03	6.10	medium
X1	615519	240.46	-13.61	6.09	low
X2	615520	124.74	207.87	1.22	high
X2	615521	125.08	207.59	1.28	medium
X2	615522	125.72	207.63	1.66	low
X3	615523	-126.91	218.47	-1.14	high
X3	615524	-125.15	218.89	-1.26	medium
X3	615525	-125.41	218.93	-1.19	low
X4	615526	-255.29	6.42	1.48	high
X4	615527	-255.23	6.67	1.30	medium
X4	615528	-255.16	6.46	1.37	low
X5	615536	-145.51	-209.81	3.09	low
X5	615537	-145.08	-209.75	3.18	medium
X5	615538	-146.12	-209.53	2.73	high
X6	615539	105.50	-222.01	4.80	low
X6	615540	105.60	-222.17	5.08	medium
X6	615541	106.02	-221.75	4.90	high
W1'	615545	-16.92	-196.61	-283.38	high
W1'	615546	-15.90	-196.27	-283.50	medium
W1'	615547	187.22	-7.86	-283.19	low
W2'	615548	187.86	-6.71	-283.03	high
W2'	615601	186.62	-3.12	-285.56	high
W2'	615602	185.92	-6.03	-285.45	medium
W2'	615603	185.98	-5.28	-285.61	low

Table B.18: Manipulator runs table 18

Run Plan	Run Number	X (cm)	Y (cm)	Z (cm)	Occupancy
W6'	615604	202.13	-10.27	-141.71	high
W6'	615605	201.51	-11.62	-141.76	medium
W6'	615606	202.47	-8.18	-141.79	low
W5'	615607	-11.38	-210.58	-142.18	high
W5'	615608	-12.13	-210.75	-142.20	medium
W5'	615609	-11.79	-210.60	-141.93	low
W9'	615610	-13.08	-198.11	101.39	high
W9'	615611	-14.49	-198.32	101.37	medium
W9'	615612	-15.51	-198.71	101.15	low
W10'	615613	189.46	-7.07	101.67	low
W10'	615614	189.40	-6.50	101.57	medium
W10'	615615	189.26	-7.29	101.56	high
W14'	615616	208.18	-11.73	254.80	high
W14'	615617	208.17	-10.71	255.13	medium
W14'	615618	207.87	-12.25	255.07	low
W13'	615619	-10.74	-217.24	254.58	high
W13'	615620	-10.08	-217.22	254.68	high
W13'	615621	-9.67	-217.16	254.68	low
W9"	615622	-14.10	-193.78	100.59	low
W10"	615623	185.20	-4.69	101.10	low
W6"	615624	201.58	-10.62	-144.52	low
W5"	615625	-12.38	-210.57	-144.76	low

Appendix C

Analysis Code

Figure C displays the basic data flow for the position reconstruction analysis. We have two sources of data:

- Manipulator Systems, and

- 1KT Detector.

The data from the manipulator positioning systems is held in the MIDAS ODB. With each run we dump the ODB contents to a file. This file is scanned for the arm lengths and angles by read_odb, which also performs the construction of the nominal position described in Section 3.3.3. In addition the location and number of the odb files and run occupancy is fed to read_odb. read_odb.py generates four text files containing the location, number, and names of ofl files, run occupancy, as well as ball positions according to one of the four positioning systems (man_limits.txt, man_safety.txt, man_prima.txt and man_secon.txt for limit and safety inclinometer and primary and secondary encoder systems respectively).

One of the four text files (usually the limit positions) is read in by a Perl script called write_lb_script.pl. With the data file to be read in the Perl script also takes a binary argument (0 or 1):

- 0 means the scripts it generates are for scott_occ, and

- 1 means the scripts are for the ofl to ntuple converter.

Each script sets the necessary environmental variables for the K2K analysis and feeds the code the data it needs.

C.1 Ntuple Generator

The ntuples generated from the laserball data contain only one event per spill due to size limitations of the ntuple file format. These ntuples are used in the position reconstruction analysis performed by Shaomin Chen.
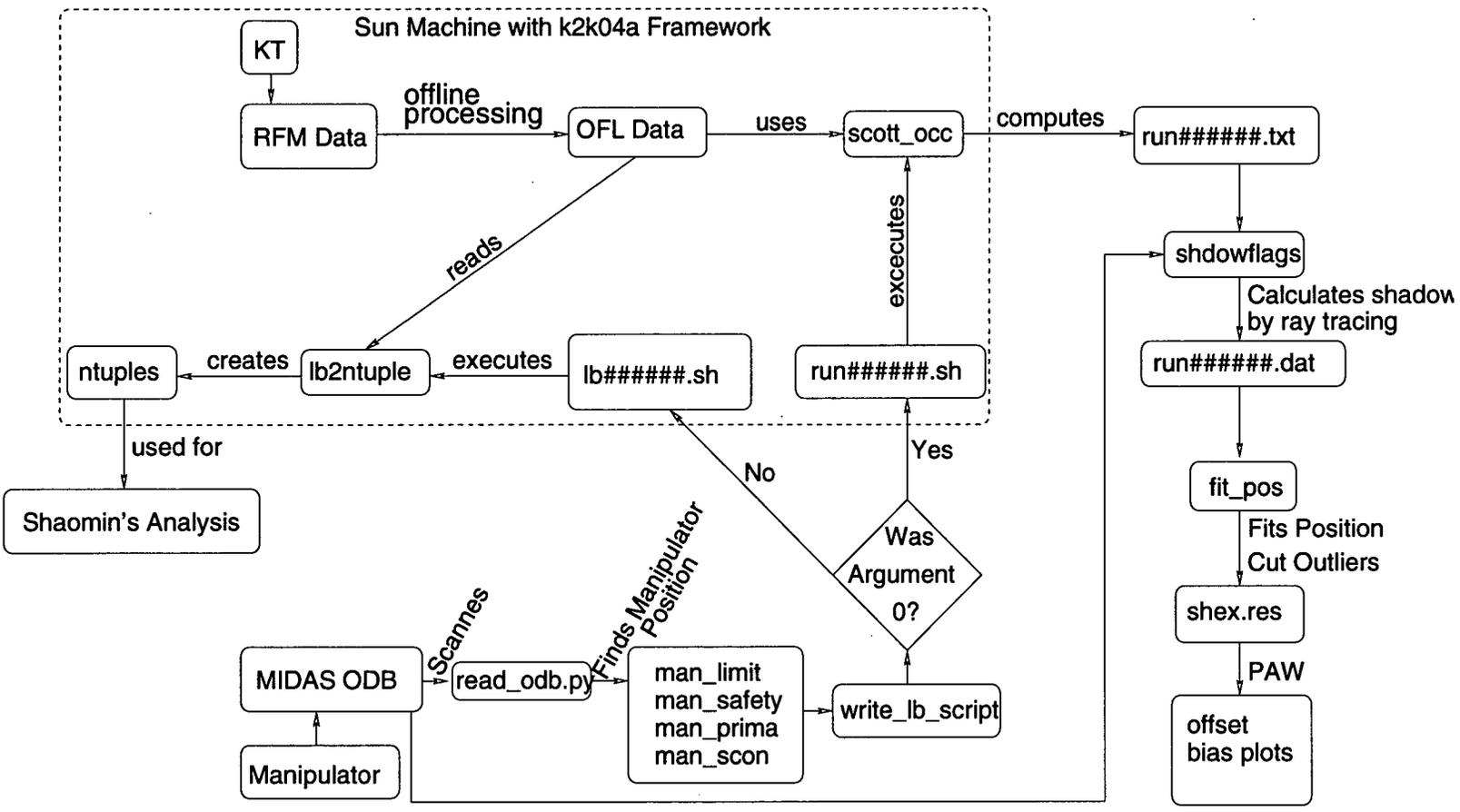
Figure C.1: Flow chart of analysis code used for the manipulator

C.2 Position Reconstruction

If the binary argument to write_lb_script.pl was 0 the scripts write_lb_script.pl generates run scott_occ. This will perform the peak finder and saturation cuts explained in sections 2.2 and 4.2.1 respectively. scott_occ generates a file for each run containing the timing peaks for each PMT, standard deviation of those peaks, time of flight to the PMT, PMT position and normals. This data is read in by the shadowflags code, which tags PMTs which are shaded according to the ray tracing algorithm. The files returned by shadowflags have the information from scott_occ, plus a flag of 0 for non-shaded and 1 for PMTs whose border is shaded and 2 for PMTs whose center is in the manipulator shadow. These files are read in by fit_pos, which scans for outlier PMTs in the time histogram and tags those with outliers by adding 4 to their shadow flag. Then the fit is run once, PMTs with large residuals are tagged by incrementing their flag by 8. The fit is run a final time ignoring all PMTs with flags greater then zero. The result positions for all runs are put into a text file, together with run numbers, position uncertainties (algorithm described in Section 2.2), and the fits χ^2.